University of Alberta

Simulation of the Initial 3-D Instability of a Vortex Ring

by

Justin Wiwchar

A thesis submitted to the Faculty of Graduate Studies and Research
in partial fulfillment of the requirements for the degree of

Master of Science

Department of Mechanical Engineering

Fall 2010
Edmonton, Alberta

Examining Committee

Lorenz Sigurdson, Mechanical Engineering

Carlos Lange, Mechanical Engineering

Mark Freeman, Physics

Abstract

Computational simulations of a perturbed vortex ring are performed to recreate and understand the instability seen in impacting water droplet experiments. Three initial conditions are tried to respectively trigger a Widnall instability, a Rayleigh centrifugal instability, and a vortex breakdown instability. Simulations with a perturbed solitary ring result in an instability similar to that seen experimentally. Waviness of the core which would be expected from a Widnall instability is not visible. Adding an opposite-signed secondary vortex ring or an image vortex ring to the initial conditions does not appear to significantly change the instability from what is seen with a solitary ring. This suggests that a Rayleigh centrifugal instability or a vortex breakdown instability are not likely at work, though tests are not conclusive. Elliptical streamlines are visible in the core of the solitary ring at early times, suggesting that an elliptic instability may be the source of the experimental instability.

Contents

Appendices

List of Tables

List of Figures

Nomenclature

α.....core radius

α_p.....primary core radius when multiple rings are present

α_s.....secondary core radius when multiple rings are present

d.....ring diameter

D_0.....Bubble initial diameter

d_p.....primary ring diameter when multiple rings are present

d_s.....secondary ring diameter when multiple rings are present

f.....body force per unit volume

Γ.....circulation

Γ_p.....primary ring circulation when multiple rings are present

Γ_s.....secondary ring circulation when multiple rings are present

h.....distance between the primary ring and the image ring

ν.....kinematic viscosity

ω.....vorticity

Φ.....vorticity source term

ρ.....density

r.....ring radius

r_p.....primary ring radius when multiple rings are present

r_s.....secondary ring radius when multiple rings are present

Re.....Reynolds number, based on circulation and kinematic viscosity

Re_o.....bubble Reynolds number, based on initial velocity and ring diameter

s.....spacing between the primary ring and the Rayleigh-unstable opposite signed ring

t.....time

u.....convection velocity

U_0.....bubble initial translation velocity

1. Introduction

Vortex rings are a common structure which occur in many different fluid flows. A water drop impacting a pool of water causes a vortex ring to form below the surface and convect down through the pool. A bursting bubble causes a vortex ring which convects up. Pushing fluid with a piston into a large chamber causes a vortex ring to form. Even the mushroom cloud of an atomic bomb contains a vortex ring. Despite the differences in generation method and large differences in Reynolds number, these vortex rings can have very similar large-scale structures.

Vortex rings have been studied in papers dating back to the 19th century. They are a basic three-dimensional structure that can be isolated and studied, hopefully giving greater understanding of the dynamics involved in some turbulent flows. Since there is a noticeable similarity in the structure of vortex rings created by different methods, developing a greater understanding of one experiment could provide insight into vortex rings found in other places.

The impacting drop experiment is easy to casually observe, though more difficult to get consistent results and data from. It can be performed on a basic level by releasing water from a dropper into a pool and observing the results below the surface. In experiments performed by Peck & Sigurdson (1994), an instability was observed, and one of the goals of this thesis is to recreate this structure computationally in order to study it and understand it better.

1.1 Literature Survey

The work presented here was inspired by research performed by Peck & Sigurdson (1994). Peck & Sigurdson created an experiment involving an impacting water drop, in order to understand the birth and evolution of the resulting vortex structure. A dyed water drop was released above a pool of quiescent water, and images of the vortex structure that formed were taken below the free surface. The sequence of images is shown in Figure 1. From these images, they observed that some vortex filaments underwent an instability and were

eventually shed off behind the main vortex ring. These filaments were referred to as “petals”. They also proposed a vortex skeleton of the resulting structure, consisting of five closed line vortices. The work presented here was an attempt to recreate the vortex structure from the experiment in order to understand the source in nature of the instability.

Sigurdson (1997) discusses how visualization techniques have been used to examine turbulent flows and discover large-scale structures. He discusses several different flow types, which include flow over a blunt-faced cylinder, flow over a blunt flat plate, the impacting drop experiment, the vorticity formed from a nuclear explosion, and the vorticity formed from a bursting bubble. He shows how flow visualization has allowed the identification of similar large-scale structures in these different flow types. Specifically, direct comparison of the water droplet images with the atomic bomb test images shows an uncanny similarity, which was first reported in Sigurdson (1991). An updated comparison was reported in Sigurdson (1997), and is shown in Figure 2.

Peck & Sigurdson (1995) deals with the same type of experiment as Peck & Sigurdson (1994), and examines the appropriate time scale to use when comparing experiments. Water drops are released from two different heights and the position and diameter of the vortex ring are observed after impact with the pool. They propose that the appropriate time scale is the time taken for the impact crater to reach its maximum depth.

Sigurdson & Peck (1995) also discusses the impacting drop experiment, and focuses on the type of instability that may be at work in the experiment. Several different instabilities are examined, which will be discussed in the next sub-section. The geometry of the instability is discussed and a representative vortex line is shown to explain how a perturbation could grow.

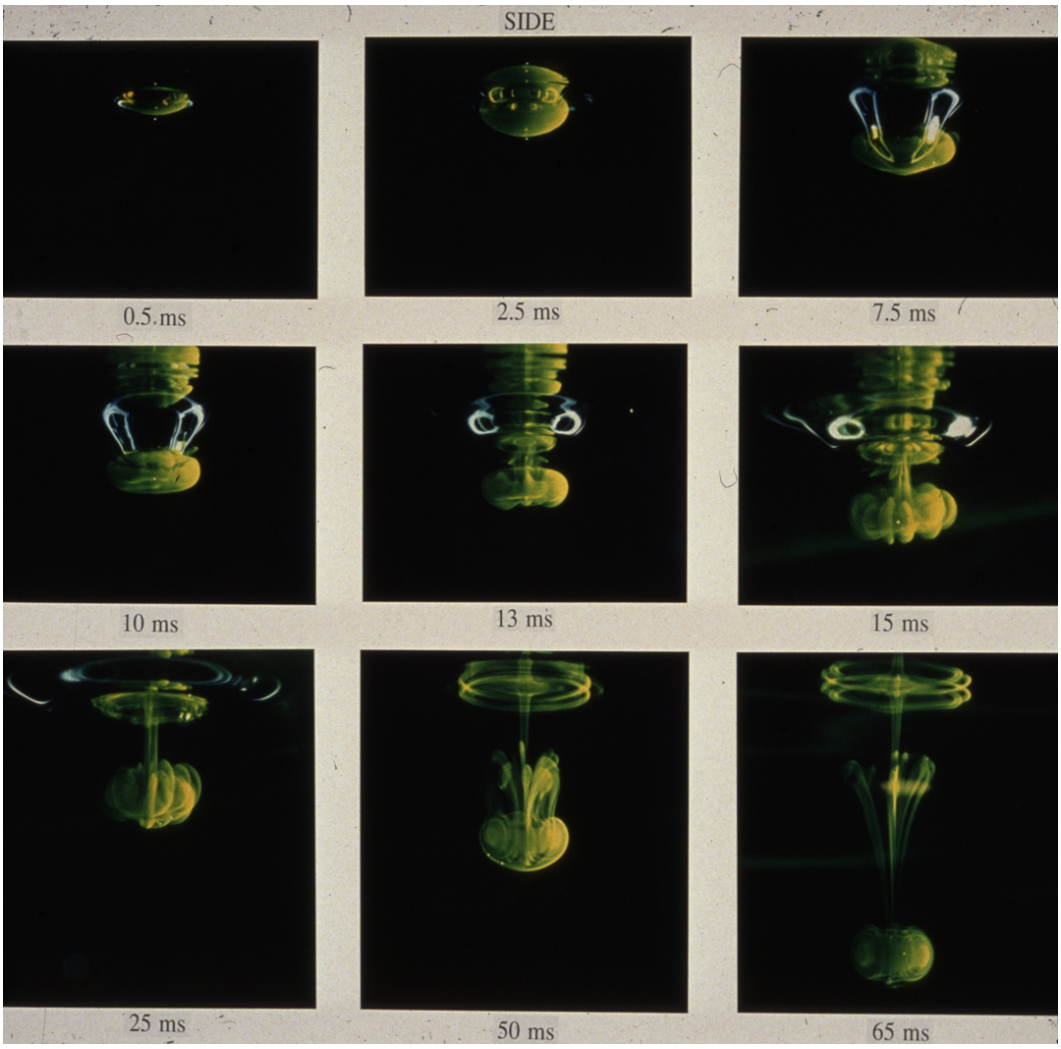

Figure 1. A dyed water droplet is released above a pool of water. Photographs of the resulting vortex structure are taken below the free surface of the pool. Images are from Peck & Sigurdson (1994), and are reused with permission from the American Institute of Physics.

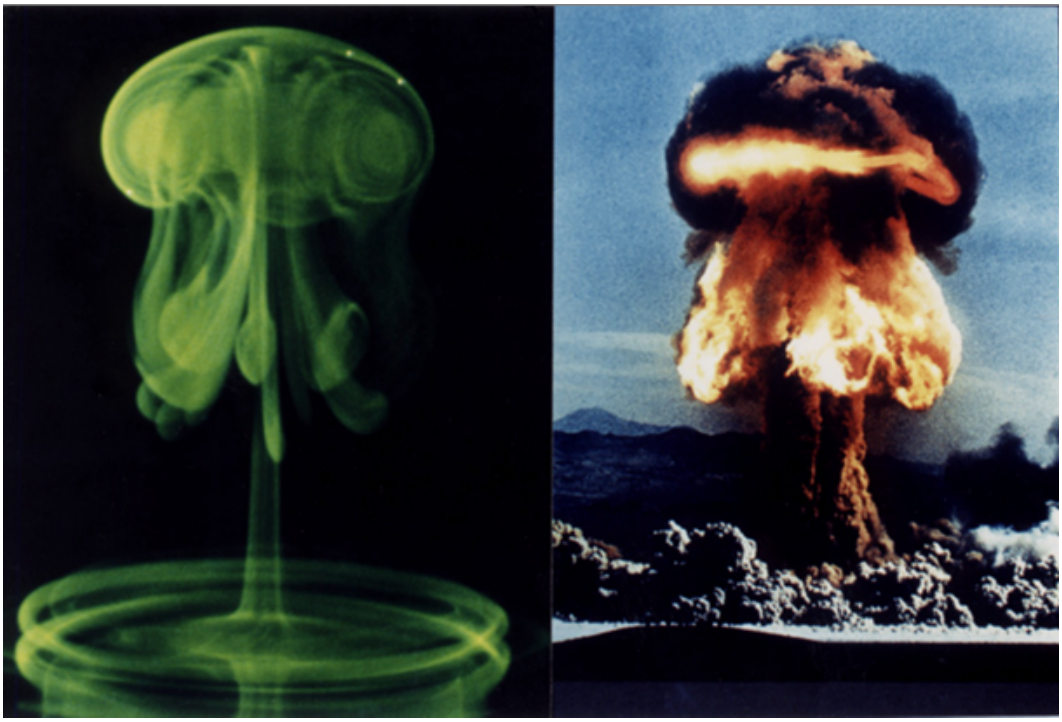

Figure 2. An image from the water drop experiment is inverted and shown next to an image from an above-ground nuclear test to show the similarity of the structure despite the large Reynolds number difference. Left image is from Peck & Sigurdson (1994) and is reused with permission from the American Institute of Physics. Right image is from the U.S. Dept. of Energy (1957). Sigurdson (1997) reported them together as shown here.

1.1.1 Types of Known Instabilities

1.1.1.1 Widnall Instability

Widnall & Tsai (1977) investigated the instability of a vortex ring to azimuthal bending waves, which followed up on work presented by Widnall, Bliss, & Tsai (1974) and Widnall & Sullivan (1973) among others. They examined thin-cored vortex rings in an ideal fluid and developed equations to determine the most-amplified wave-number for different vorticity distributions in the core. The instability presented in their paper is often referred to as the "Widnall instability" or "Krutsch instability" and involves the core of the vortex ring becoming "wavy" due to the straining field created by the circular geometry of the ring.

1.1.1.2 Rayleigh Centrifugal Instability

Maxworthy (1972) investigated vortex rings produced by pushing fluid through a hole in a plate into a fish tank. He discovered that for large Reynolds numbers, the initial ring became unstable and then formed a new, larger vortex ring a short time later. This was determined to be caused by the entrainment of opposite-sign vorticity into the ring which causes an unstable layer of vorticity around the outside of the ring. This type of instability is often referred to as a "Rayleigh centrifugal instability" and is caused by the rapidly decreasing circulation towards the outside of the vortex ring.

1.1.1.3 Elliptic Instability

Leweke and Williamson (1998) analysed the three-dimensional instability of counter-rotating vortex pairs to short waves. They found that due to the mutually induced strain on each vortex, the core of the vortices would develop elliptical streamlines which encouraged a three-dimensional instability. In addition to the core becoming elliptical in shape, the vortex pair would also lose its axial symmetry, with the centers of the vortices moving away from each other in the streamwise direction. In the long-term flow, secondary vortex pairs developed perpendicular to the primary vortex pair, caused by fluid crossing over between the pair of primary vortices. They suggest that this "elliptic instability" is the

source of the disturbance seen in Widnall & Tsai (1977) and found very good agreement when comparing growth rates of the most unstable modes.

1.1.2 Others' Calculations

Saffman (1978) presented a method for estimating the number of waves on an unstable vortex ring. His results applied to vortex rings formed by pushing fluid out of a tube, and the number of waves was dependant on the Reynolds number and the vorticity distribution in the core of the ring. While it would be valuable to predict the number of waves and their growth rate in our simulation, it would be difficult to compare Saffman's results to our work given the difference in vorticity distribution and Reynolds number.

Shariff, Verzicco & Orlandi (1994) performed a numerical study of the instability of vortex rings. They introduced both a random perturbation and a single-mode perturbation to the vortex ring, and examined the linear and early nonlinear phases. The purpose of their research was to expand on previous research done by Widnall, Bliss & Tsai (1974), and Widnall & Tsai (1977). The simulation produced instabilities that agree with the results presented in Widnall, Bliss & Tsai (1974), and they observed an elongation of the most unstable mode, which could be similar to the vortex filaments which get shed off behind the vortex ring in Peck & Sigurdson (1994). However, the simulations were performed at a higher Reynolds number than was studied in the experiments by Peck & Sigurdson (1994), and they only discuss 2-Dimensional structures.

Dazin, Dupont, & Stanislas (2005, 2006) performed an experimental study of vortex rings to examine the linear and non-linear phases. They used planar laser induced fluorescence and particle image velocimetry to evaluate the vortex rings, which were formed by forcing water through a submerged pipe with a piston. The earlier paper deals with the initial linear phase, and the later paper deals with the non-linear phase that follows. Despite the difference in the method of vorticity generation, they were able to see the same vortex filaments wrapped around the

main ring as seen in Peck & Sigurdson (1994). They theorize that the filaments generate near the streamwise median plane of the vortex ring and could be due to a curvature or pressure gradient effect; however there is not any discussion of what they mean by this or how they came to this conclusion. Their experiments are performed at a much higher Reynolds number than the experiment from Peck & Sigurdson (1994), which may explain why they did not observe the relaminarization that occurs in the later stages of the Peck & Sigurdson (1994) experiments.

Watanabe, Saruwatari, and Ingram (2008) performed a computational analysis of the free surface flows under impacting droplets, similar to the work presented here. However, their method was to simulate the actual impact between the droplet and the free surface and observe the vorticity generated from the impact. Since simulating the droplet-surface interactions complicates the system considerably, the numerical method used needed to be more approximate compared to the direct numerical simulation presented in this work.

Wantanabe et al (2008) observed four counter-rotating vortex pairs trailing behind the main vortex ring, oriented vertically. They conclude that these vortex pairs stretch out behind the main vortex ring, forming the “stalk” observed in Peck & Sigurdson (1994). They also conclude that these stalks get pulled through the main vortex ring and wrap around it to form the “petals” from Peck & Sigurdson (1994).

While Wantanabe et al (2008) is a valuable study of the impacting droplet, they appear more interested in the computational and numerical aspects of the simulation than the vortex dynamics involved in the impacting droplet experiment. They don’t comment on the type of instability present on the main vortex ring or suggest if it is likely a Widnall instability or some other instability at work. They also don’t comment on the possible existence of a counter-rotating vortex ring above the main vortex ring, which was speculated to exist from the

experiments by Peck & Sigurdson (1994).

Feng, Kaganosvskiy, & Krasny (2009) performed a computational simulation leading to a similar geometry analyzed in this thesis, but beginning from different initial conditions. They started with a vortex sheet in the shape of a circular disc which was perturbed by adding waves which had increasing amplitude with increasing radial distance from the center of the disc. With this perturbation they were able to visualize the vortex filaments seen in Peck & Sigurdson (1994). No physical argument for using that particular perturbation is given, however they appear to recreate the phenomenon from Peck & Sigurdson (1994) and the similarity is impressive. It should be noted that the paper was not published until this thesis was in its final stages.

Dziedzic & Leutheusser (1996) examined vortex rings at various Reynolds numbers to attempt to classify the rings based on their appearance. They proposed four classifications for the vortex rings: laminar, wavy, turbulence-producing, and turbulent. Laminar rings appear as smooth toroids and are expected at a Reynolds number below about 1000. Wavy rings have a visible waviness in the toroid and are expected at Reynolds numbers between about 1000 and 2000. Turbulence-producing vortex rings have a turbulent wake, while turbulent vortex rings have a turbulent wake and core, and both are expected at Reynolds numbers above about 2000.

1.2 Objectives

The simulations detailed here were a follow-up to the work done by Peck and Sigurdson (1994) Experiments were run where a water droplet fell into a pool of quiescent water, and the resulting vorticity below the surface of the pool was observed. After the droplet impacted with the pool of water, a vortex ring formed below the surface and convected downwards. The vortex ring developed an instability and a bracelet structure developed, consisting of rings of vorticity wrapped around the core of the vortex ring. The goal of the simulations was to

recreate the experiment computationally in hopes of explaining the source of the instability causing the bracelet structure.

The exact physics of the experiment were not recreated, which would be difficult to simulate with the complex interactions between the falling droplet and the pool of water. Instead, a vortex ring was formed, and the ring was perturbed by adding different vorticity fields. The initial vorticity fields were chosen by observing the experimental results and speculating what other vorticity might be present. If a certain initial vorticity field caused the bracelet structure to appear in the simulation, then it could be inferred that the same vorticity field might be causing the instability in the experiment. This provides valuable insight towards determining the exact source of the instability, where detailed experiments might be too difficult, time consuming, or expensive.

Three base vorticity fields were used in these simulations. In some of the simulations a second ring of opposite sign, smaller diameter, and smaller circulation was added at various positions above the main ring. It was thought that opposite sign vorticity may form just below the surface of the pool as the vortex ring is moving away, and that perhaps a Rayleigh instability was causing the bracelet structure.

In other simulations, an image vortex was placed above the main ring to cause it to contract as it convects downwards. In the experiment the vortex ring undergoes a contraction, and it was thought that this may be contributing to the instability causing the bracelet structure.

Finally, simulations were run with no opposite sign vorticity present. This was done to see if either of the previous vorticity fields were actually causing the instabilities that were observed, or if they were being caused by other perturbations to the vorticity.

1.3 Outline of Thesis

In the following thesis, Section 2 deals with the details of the computation performed in this thesis. Section 2.1 gives an overview of the details of the code. Section 2.2 explains the code verification process that was performed. Section 2.3 explains the computational domain. The initial conditions of the simulations are detailed in Section 3. Section 3.1 details the different initial vorticity distributions that were used to test the instability hypothesis. Section 3.2 explains the types of perturbations that were introduced into the system to trigger the instability. Section 3.3 discusses the turbulence regimes resulting from the different Reynolds numbers used in the simulations. Results and Discussion are contained in Section 4. Section 4.1 details simulations performed with a solitary vortex ring. Section 4.2 details simulations performed with an opposite-signed vortex ring present. Section 4.3 details simulations performed with an image vortex ring. Section 4.4 discusses the skeleton vortex structure seen in the simulations. Section 4.5 discusses the growth of the instability. Section 4.6 discusses the possible source of the instability. Conclusions are contained in Section 5, and Section 5.1 presents ideas for future work.

2. Computational Details

2.1 Details of the Code

The code used for the simulations was developed by J.H. Walther and P. Koumoutsakos, and simulations were run with the collaboration of J. H. Walther. Simulations were performed remotely on a supercomputer located in Manno, Switzerland. For more detailed information about the code than presented here, see Walther and Koumoutsakos (2001).

The code uses a 3D viscous vortex method to simulate the flow. Unlike traditional Eulerian methods that look at discrete volumes of the flow and balance the fluxes into and out of the volume, vortex methods use a Lagrangian approach, focusing on discrete particles within the flow. When the vorticity is located in specific areas and is not extending to infinity, this approach has computational advantages over others. Vortex methods in general discretize the vorticity field into individual vortices, each having their own circulation. In three-dimensional methods, the vortices also have their own volume, and are also known as vortex blobs. By solving the Navier-Stokes equations, the motion of the vortices can be found, and therefore the movement of the flow can be simulated.

The governing Navier-Stokes equation in ***u*-*ω*** form for constant density and viscosity is as follows,

$$\frac{D\boldsymbol{\omega}}{Dt} = (\boldsymbol{\omega}\cdot\nabla)\boldsymbol{u} + \nu\nabla^2\boldsymbol{\omega} + \Phi \tag{1}$$

where D/Dt is the material derivative defined in Equation (2), $\boldsymbol{\omega}$ is the vorticity, $\boldsymbol{u}$ is the velocity, ν is the kinematic viscosity, and Φ is the vorticity source term defined in Equation (3),

$$\frac{D\boldsymbol{\omega}}{Dt} = \frac{\partial\boldsymbol{\omega}}{\partial t} + \boldsymbol{u}\cdot\nabla\boldsymbol{\omega} \tag{2}$$

$$\Phi = \frac{1}{\rho} \nabla \wedge \boldsymbol{f} \tag{3}$$

where ρ is the fluid density, $\nabla \wedge$ denotes the curl, and $\boldsymbol{f}$ is the body force per unit volume.

The vorticity field is discretized using a number of vortex particles, each having their own volume and strength. The i^{th} particle strength is defined as,

$$\boldsymbol{\alpha}_i = \mathrm{vol}_i \boldsymbol{\omega}(\boldsymbol{x}_i) \tag{4}$$

where vol_i is the volume of each particle. Since it is a product of the particle volume and the vorticity, the particle strength should not be confused with the circulation or the vorticity magnitude of the particle.

Each particle is moved in two steps. The first step is inviscid, and corresponds to the tilting and stretching term from Equation (1). The locations of the particles are changed to account for advection, while the strength of the particles is changed to account for vortex tilting and stretching. The inviscid first step is solved using the following equations,

$$\frac{d\boldsymbol{x}_i}{dt} = \boldsymbol{u}(\boldsymbol{x}_i) \tag{5}$$

$$\frac{d\boldsymbol{\alpha}_i}{dt} = \mathrm{vol}_i (\boldsymbol{\omega}(\boldsymbol{x}_i) \cdot \nabla) \boldsymbol{u}(\boldsymbol{x}_i) \tag{6}$$

The second step is viscous, and corresponds to the second and third terms of Equation (1) which account for diffusion of the vortex particles and for body forces. In this step the vortices are held in place, and the strength of the vortices is

modified to account for diffusion. This second step is solved using the following equations,

$$\frac{d\boldsymbol{x}_i}{dt} = 0 \tag{7}$$

$$\frac{d\boldsymbol{\alpha}_i}{dt} = \mathrm{vol}_i\left(\nu \nabla^2 \boldsymbol{\omega}(\boldsymbol{x}_i) + \Phi(\boldsymbol{x}_i)\right) \tag{8}$$

In the simulations presented here, the vorticity source term is zero as there are no body forces.

To decrease the computational cost of computing the velocity field, the code uses a vortex-in-cell method. In the vortex-in-cell method, the vorticity field is interpolated onto a uniform grid, and finite differences are used to compute the velocity field and vorticity stretching on the grid. This eases the computational burden because for these calculations the vorticity only exists at set grid points, instead of existing at any point within the domain. After the velocity field is computed, the grid is used to update the position and strength of the vortices.

A re-meshing procedure, similar to the vortex-in-cell method working in reverse, is used to re-form the vortex particles. The vortex particle strength is assigned to a mesh, and a new set of particles is formed based on the mesh vorticity. This allows vortex particles to be formed or removed where necessary, while ensuring enough vortex overlap is present. This is important because having sufficient vortex overlap ensures the convergence of the vortex method.

2.2 Code Verification

To verify that the code was accurate, a thin-cored vortex ring was simulated and the convection velocity was compared to theoretical values. This test was chosen because a convecting thin-cored vortex ring is essentially a simplification of the

simulations presented in this paper, and because theory is readily available to predict the convection velocity. The theoretical convection velocity U_c of the centroid of a thin-cored vortex ring with an Oseen core can be expressed as follows,

$$U_c = \frac{\Gamma}{4\pi R}\left(\ln\frac{8R}{\sqrt{4\nu t}} - 0.558\right) \tag{9}$$

where R is the radius of the vortex ring.

Several simulations were run with varying core radius α to ensure that the vortex ring was suitably "thin-cored" for the theory to apply. Simulations were run with core radius ratios α/R of 0.2, 0.1, and 0.05. Making the core radius much smaller made the computational costs prohibitive. At a core radius ratio of 0.05 there was a maximum error between the simulation and theory of -9.4%, however for most of the simulation the error was closer to -3%. For graphs comparing convection velocities and percent error, see Figures 3 and 4.

There are multiple ways to explain the difference between the simulated convection velocity and the theory. For one, the theory is for a thin-cored vortex ring ($\alpha/R \ll 1$), while the smallest core used in the simulations had a core ratio $\alpha/R = 0.05$, which may not have been suitably small. Making the core in the simulation even thinner may have improved the agreement with theory, however it would have made the computational costs prohibitive. Also, the simulated vortex ring does not retain its core thickness throughout the simulation. As time progresses, the core diffuses and becomes thicker, therefore the simulation would be expected to agree less with theory at later times. This is evident in Figure 4, as the percent error begins to increase at later times for the $\alpha/R = 0.05$ case.

Despite the differences between the simulation and the theory, most of the error is in the 3-4% range, and the trend in Figure 4 suggests that the error would be

smaller if a thinner core could have been used. The code error is likely much lower because the error presented here is a combination of two error sources: the error caused by the theory and simulation not matching exactly, and the error introduced by the code calculations. However, this provides an upper bound for the error introduced by the code, which for our uses is acceptable.

The convection velocity simulations were also performed at a coarser grid resolution. The resulting convection velocity did not change between the simulations, suggesting that the grid was suitably refined.

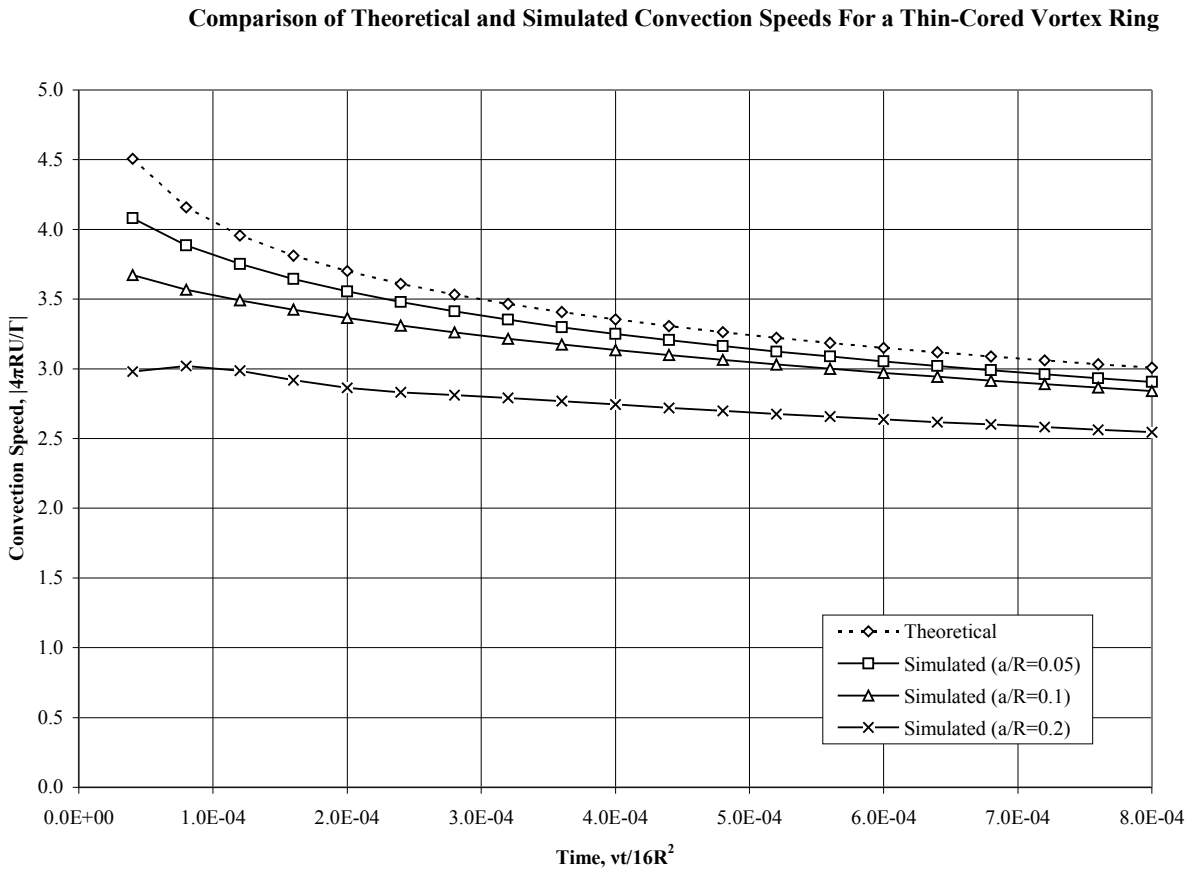

Figure 3. Convection speed vs. time for a theoretical thin-cored vortex ring and simulated vortex rings with $\alpha/R = 0.05$, $\alpha/R = 0.1$, and $\alpha/R = 0.2$. Convection speed and time have both been nondimensionalized.

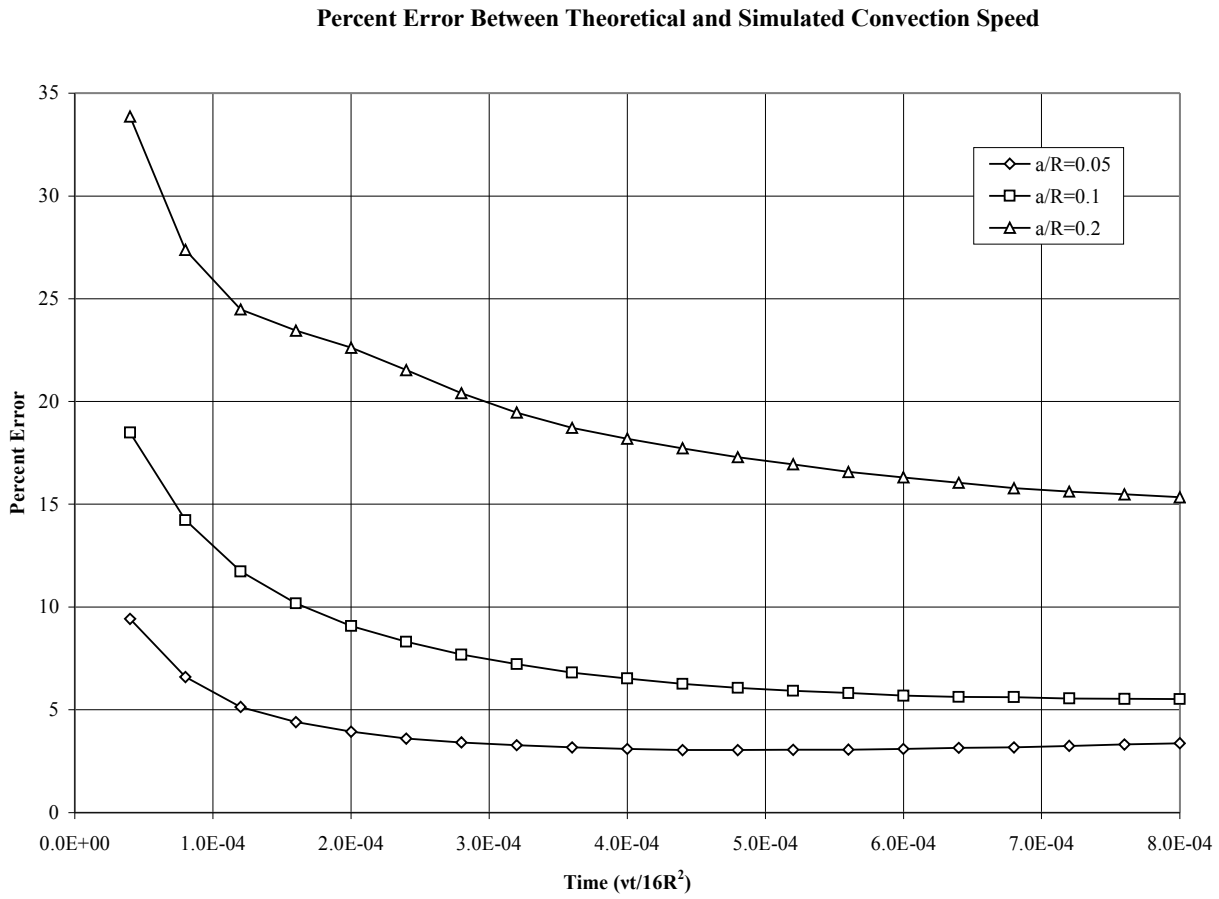

Figure 4. Percent error between the theoretical convection speed of a thin-cored vortex ring and the simulated convection velocity of vortex rings with $\alpha/R = 0.05$, $\alpha/R = 0.1$, and $\alpha/R = 0.2$. Time has been nondimensionalized.

2.3 Computational Domain

The width and depth of the computational domain were 1 cm, and the height ranged from 1 cm to 2 cm. The grid spacing was $3.891 * 10^{-3}$ cm in each direction. The time steps ranged from $5 * 10^{-5}$ s to $2 * 10^{-4}$ s for the majority of the simulations, with a data file being output every 10 to 40 time steps. Simulations at higher Reynolds numbers had smaller time steps, while the grid spacing was the same for all simulations.

The domain used periodic boundary conditions in all directions, such that any particle passing through a wall of the boundary will emerge from the opposite wall. Since the vortex ring is convecting down through the domain, care was taken to ensure that the ring did not move through an area contaminated with vorticity. The domain was made large enough that simulations could be terminated before the ring looped around to the point it started at.

To ensure accuracy of the simulations, they were run at the highest grid resolution possible within the memory restrictions of the supercomputer. Comparing the core size in the simulations to the grid size shows that there were about 30 grid points within the core diameter, which should be sufficient to resolve the core adequately. The instabilities we were interested in were fairly large compared to the grid resolution, so they should not be eliminated by discretization error. The number of vortex blobs in the domain was approximately $30 * 10^{6}$, again suggesting that the domain was suitably resolved.

The code calculates the kinetic energy at each time step. This was observed for each simulation to ensure that the energy did not suddenly grow, ensuring that the solution was stable.

3. Simulation Initial Conditions

Several approaches were tried to attempt to recreate the bracelet structure seen in Peck & Sigurdson (1994). Section 3.1 explains the initial conditions used to trigger three different instabilities. Section 3.1.1 details the simulation of a solitary vortex ring, Section 3.1.2 details the addition of a Rayleigh-unstable opposite-signed vortex ring, and Section 3.1.3 details the addition of an image vortex ring. Section 3.2 explains the different perturbations added to the vorticity in the system. Section 3.2.1 details the "random" perturbation, and section 3.2.2 details the "wave" perturbation. For an overview of the parameters tested in the simulations, see Table 1, and for the specific details of each simulation performed, see Appendix 1.

3.1 Instability Hypothesis

In order to attempt to recreate the bracelet structure seen experimentally, multiple hypotheses were developed to explain what was causing the bracelet structure to form. The experimental results were observed, and initial vorticity fields were developed for the simulations based on where other vorticity was thought to be found in the experiments. If a certain initial vorticity field caused the bracelet structure to appear in the simulations, then it could be inferred that the same vorticity field could be causing the bracelet structure in the experiment.

Three different initial vorticity fields were simulated. In one case, a solitary axisymmetric vortex ring was used. In another case, an opposite-sign vortex ring was added near the main ring. In the last case, an image vortex ring was placed above the main ring. The intent was to trigger various instabilities which are discussed in the following sections.

The vorticity fields were also perturbed in multiple ways, which are described in Section 3.2.

Sample Image	Schematic	Type of Secondary Vorticity	Secondary Vorticity Location	Re	Primary Ring Perturbation
Fig. 5a	Fig. 6	None	N/A	1000	None
Fig. 5b	Fig. 7	Opposite-signed ring (15%)	s = 1.17 α	1000	None
Fig. 5b	Fig. 7	Opposite-signed ring (15%)	s = 1.17 α	1400	None
Fig. 5b	Fig. 7	Opposite-signed ring (15%)	s = 1.17 α	1400	Random, 1% of max vorticity
Fig. 5b	Fig. 7	Opposite-signed ring (15%)	s = 1.17 α	1400	Random, 2% of max vorticity
Fig. 5c	Fig. 7	Opposite-signed ring (30%)	s = 0.94 α	1400	Random, 10% of max vorticity
Fig. 5c	Fig. 7	Opposite-signed ring (30%)	s = 0.67 α	1400	Random, 10% of max vorticity
Fig. 5d	Fig. 7	Opposite-signed ring (30%)	s = 0.67 α	1400	30 waves, 0.33% r_p amplitude
Fig. 5d	Fig. 7	Opposite-signed ring (30%)	s = 0.67 α	1400	30 waves, 10% r_p amplitude
Fig. 5d	Fig. 7	Opposite-signed ring (30%)	s = 0.67 α	1400	30 waves, 1% r_p amplitude
Fig. 5e	Fig. 7	Opposite-signed ring (30%)	s = 0.67 α	2500	30 waves, 1% r_p amplitude
Fig. 5f	Fig. 6	None	N/A	1400	30 waves, 0.33% r amplitude
Fig. 5f	Fig. 6	None	N/A	1400	30 waves, 1% r amplitude
Fig. 5g	Fig. 6	None	N/A	2500	30 waves, 1% r amplitude
Fig. 5h	Fig. 8	Image vortex	h = 4 α	1400	30 waves, 1% r_p amplitude
Fig. 5h	Fig. 8	Image vortex	h = 2 α	1400	30 waves, 1% r_p amplitude
Fig. 5h	Fig. 8	Image vortex	h = 1 α	1400	30 waves, 1% r_p amplitude

Table 1. Overview of the parameters used in the simulations. Multiple simulations were often run for a single set of parameters. Sample images are given in Figure 3. For a complete list of simulations performed, see Appendix 1.

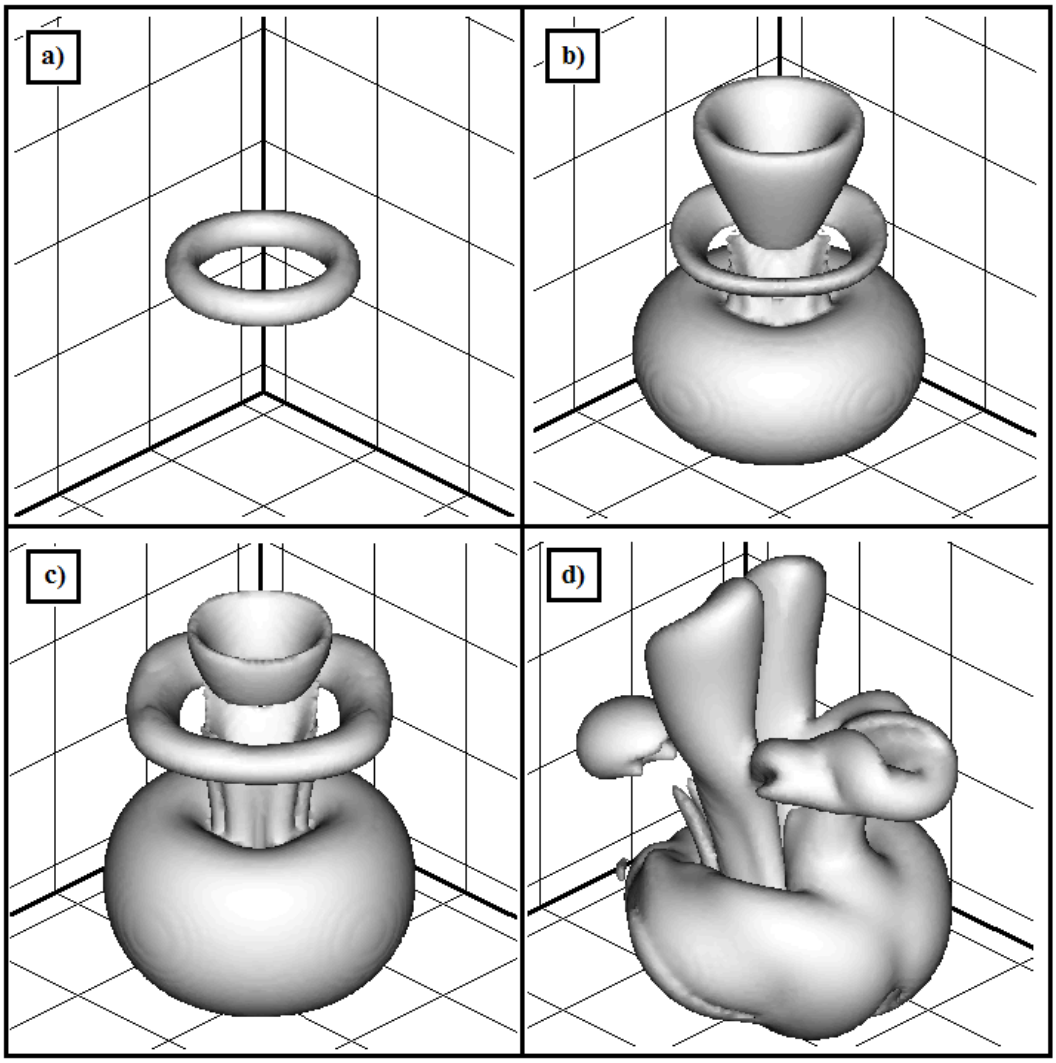

Figure 5, Part 1. Sample images for the simulations detailed in Table 1. **a)** Thin ring convection velocity tests. **b)** Rayleigh unstable opposite-signed ring with either no perturbation or small random perturbation to the primary ring. Secondary ring is 15% of the primary rings circulation, Re = 1400. **c)** Rayleigh unstable opposite-signed ring with large random perturbation to the primary ring. Secondary ring is 30% of the primary rings circulation, Re = 1400. **d)** Rayleigh unstable opposite-signed ring with 30 wave-number perturbation. Secondary ring is 30% of the primary rings circulation, Re = 1400.

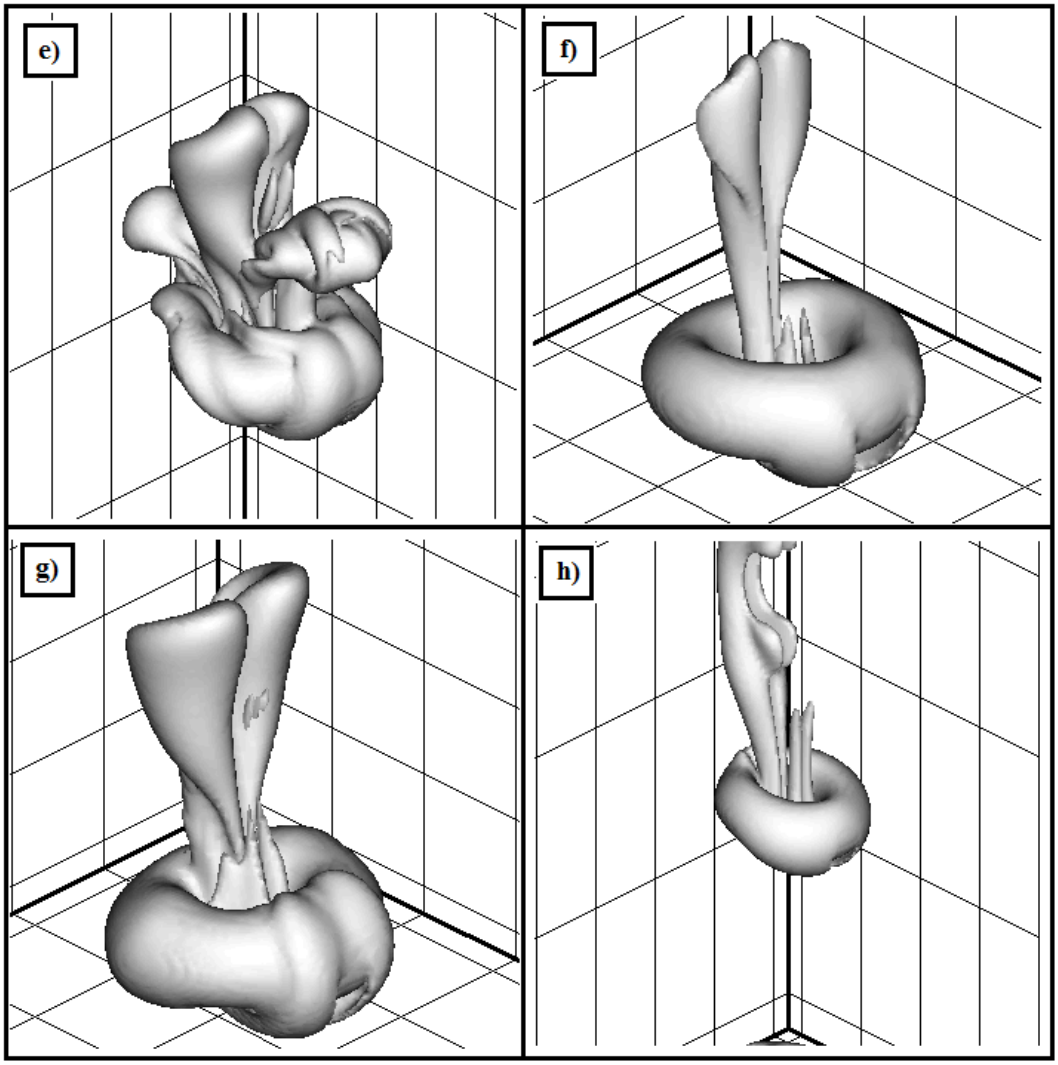

Figure 5, Part 2. Sample images for the simulations detailed in Table 1. **e)** Rayleigh unstable opposite-signed ring with 30 wave-number perturbation. Secondary ring is 30% of the primary rings circulation, Re = 2500. **f)** Solitary ring with 30 wave-number perturbation, Re = 1400. **g)** Solitary ring with 30 wave-number perturbation, Re = 2500. **h)** Image vortex ring added, Re = 1400.

3.1.1 Solitary Ring

It was hypothesised that perhaps an instability developed on the main ring that was not a result of any vorticity outside of the main ring, and this was causing the bracelet structure to occur. To simulate this, a solitary axisymmetric vortex ring was used. No other vorticity was present in the domain. For a diagram showing the cross-section of this initial vorticity, see Figure 6.

The simulation of the solitary ring also provides a helpful baseline to compare with the other simulations. If the bracelet structure was observed with the solitary ring, and also observed with either of the other initial vorticity fields, it would suggest that the other vorticity field was not solely responsible for causing the bracelet structure.

3.1.2 Opposite-Signed Ring

A Rayleigh centrifugal instability was hypothesised to be a possible cause of the bracelet structure. In the experiment, as the vortex ring breaks away from the free surface of the pool, it is possible that some opposite-signed vorticity is formed along the free surface and gets pulled into the main ring. This opposite-signed vorticity could cause the vortex ring to be Rayleigh unstable which could contribute to the formation of the bracelet structure.

To simulate this, an opposite-signed vortex ring was added near the core of the main ring. The position of the opposite-signed ring with respect to the main ring was altered, to see if moving the opposite-signed ring closer or further from the main ring would cause the bracelet instability to appear. For a diagram showing the cross-section of this initial vorticity, see Figure 7.

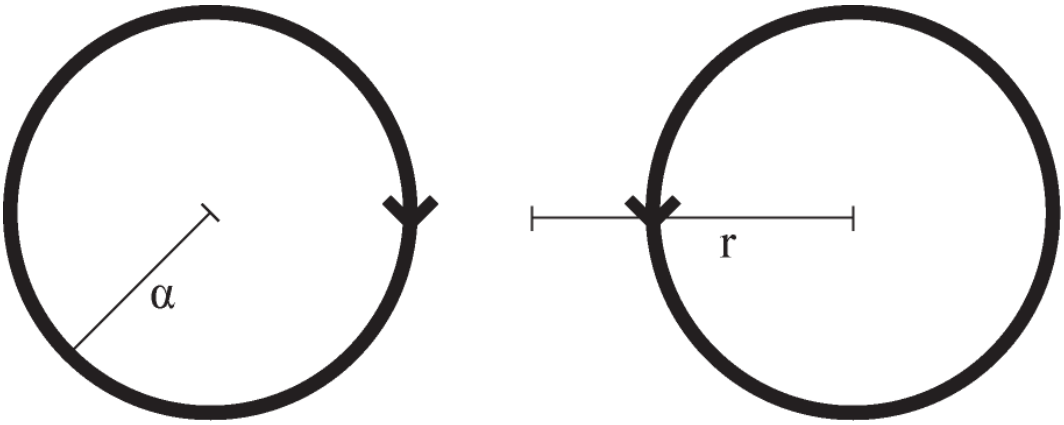

Figure 6. A schematic of a cross-section through the core of the vortex ring for the solitary ring simulation. α denotes the radius of the core, and r is the radius of the vortex ring.

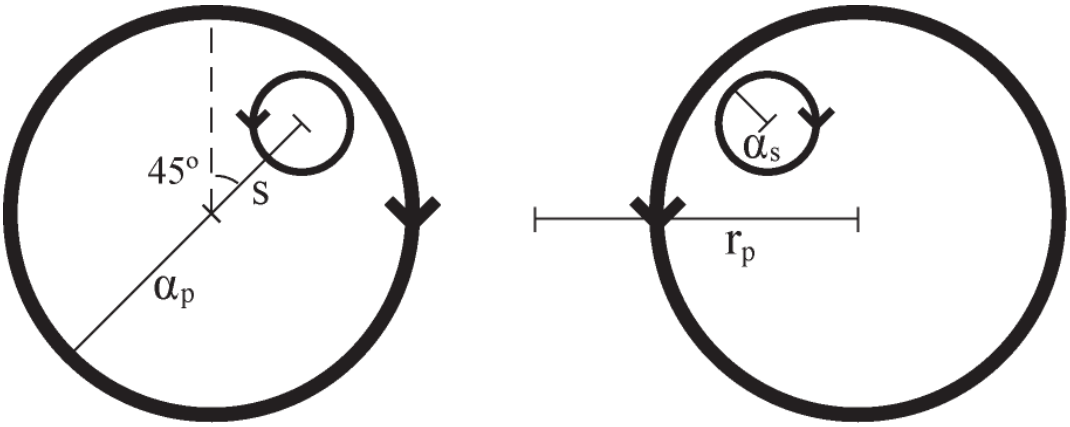

Figure 7. A schematic of a cross-section of the cores of the two vortex rings, showing the placement of the opposite-signed secondary ring compared to the primary ring. α_p is the radius of the primary ring core, s is the spacing between the primary ring and secondary ring, and r_p is the radius of the primary ring. In some simulations $s < \alpha_p$ as in the figure, while in other simulations $s > \alpha_p$ which places the secondary ring outside of the core of the primary ring.

3.1.3 Vortex Breakdown

Another hypothesis for the cause of the bracelet structure involves the compression of the vortex ring as it moves away from the free surface of the pool. In the experiment there is a visible reduction in the radius of the vortex ring in early times as it moves away from the free surface, which could be the source of an instability and causes the bracelet structure to form. Vortex breakdown is discussed in Panton (1996) and occurs when a vortex aligned with the flow moves into an area of increasing pressure gradient or a slower moving region of the flow.

To simulate the compression of the vortex ring, an image vortex ring was placed above the main ring. The distance between the two vortex rings was altered to see the effect on the main ring. Moving the two rings closer together increases the amount that the main ring contracts, but it also causes the core of the ring to lose its circular symmetry due to the effect of the vorticity in the image ring. The intent of these simulations was not to investigate the effect of an asymmetric core, so the rings were not placed close enough together to cause a significant asymmetry. For a diagram showing the cross section of this initial vorticity, see Figure 8.

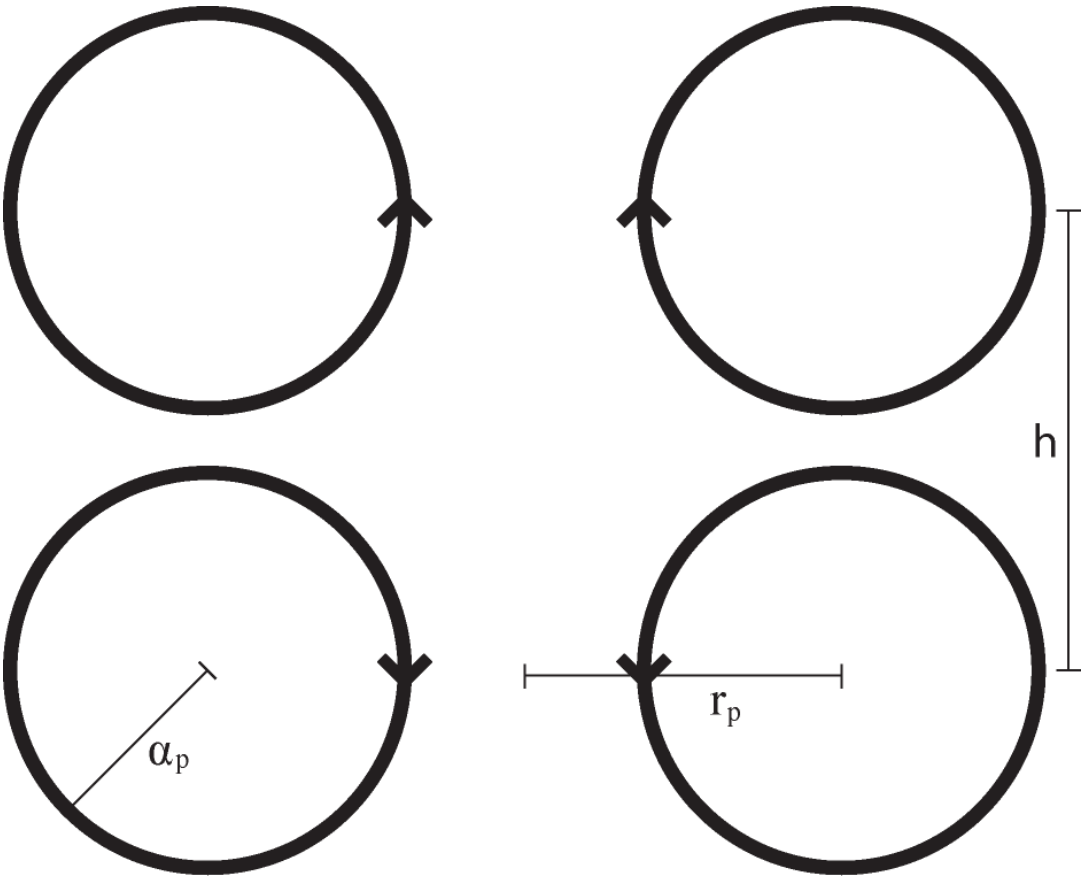

Figure 8. A schematic of a cross section through the cores of the vortex rings, showing the placement of the image vortex ring with respect to the primary ring. α_p denotes the radius of the primary core, r_p is the radius of the primary ring, and h is the spacing between the primary ring and the image vortex ring. Since the secondary ring is an image vortex, both vortex rings have the same core radius, ring radius, and vorticity amplitude, and the sign of the vorticity is opposite.

3.2 Details of Perturbations Used

To attempt to recreate the bracelet structure, several methods of perturbing the vorticity were attempted. These involved modifying the amplitude or location of the vorticity in the simulation.

3.2.1 "Random" Perturbation

The first type of perturbation that was used involved changing the magnitude of the vorticity and not the location. A small amount of vorticity was added or subtracted from each point of vorticity in the domain. The maximum perturbation was set based on either the local vorticity or the global maximum vorticity. It was then scaled using a random number generated for each point of vorticity, and added or subtracted from the vorticity at that point. The random number ranged from 0 to 1. See Equation 10.

$$\omega_{perturbed} = \omega_{initial} + 2 * (\text{Max perturbation}) * (\text{Random number} - 0.5) \quad (10)$$

Initially the maximum perturbation was based on the global vorticity, such that every point of vorticity had an equal chance of being perturbed the same amount. This was later changed to be based on the local vorticity, such that areas of higher vorticity would likely receive larger perturbations than areas of lower vorticity. For an example of what the random perturbation could look like, see Figure 9.

The code used a "clean function" to ensure the vorticity field is divergence-free. Since the random perturbation is non-physical, the added perturbation might be eliminated by the code to ensure the vorticity is divergence-free. Tests were done to investigate the effect of the clean function, and it was found that the perturbation was reduced by a maximum of 24%. Therefore, the clean function reduces the magnitude of the perturbation, but does not eliminate it. See Appendix 8 for details of the calculations used to determine the effect of the clean function.

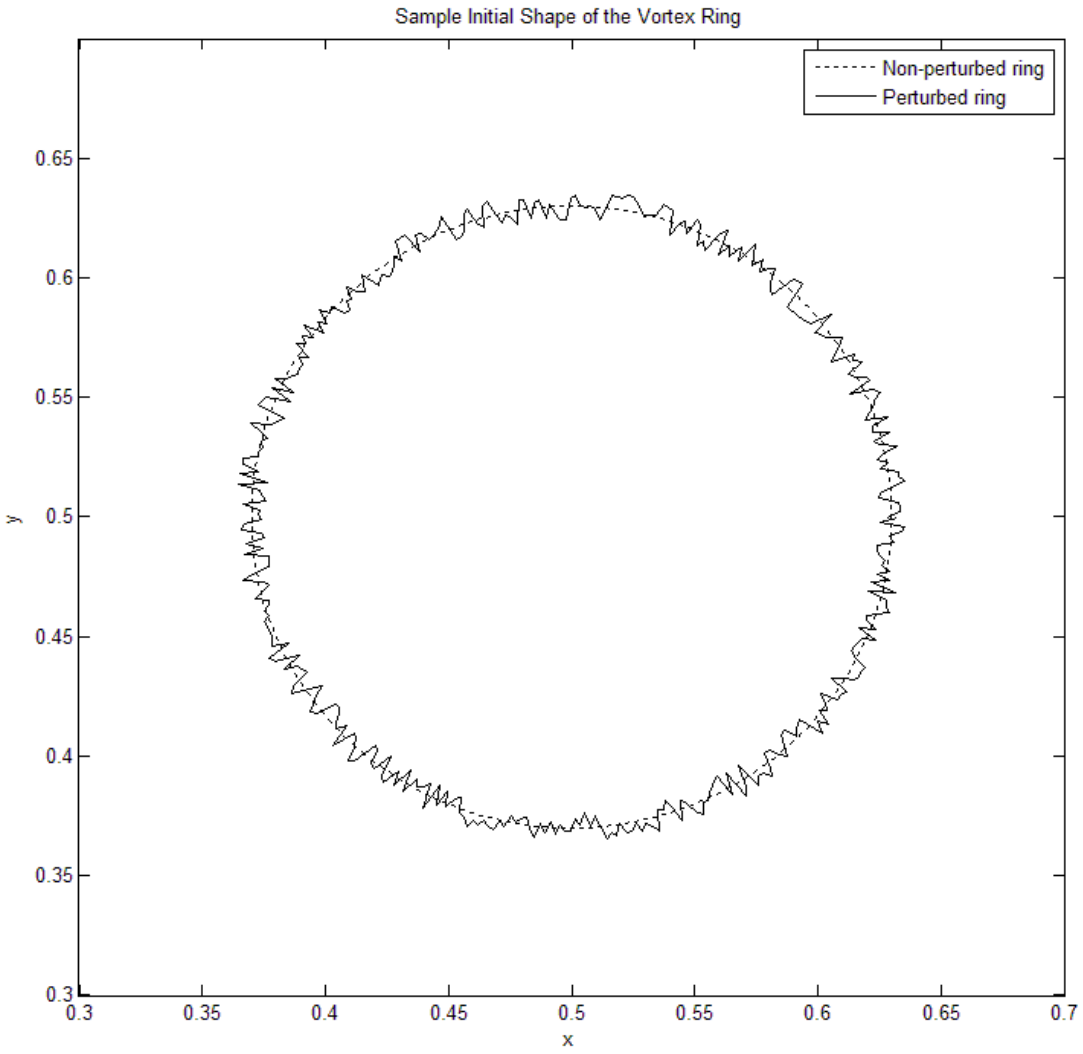

Figure 9. Example of how the random perturbation could change the shape of the vortex ring core. The dashed line represents the center of the core in a non-perturbed case, and the solid ring represents the center of the core with the random perturbation applied.

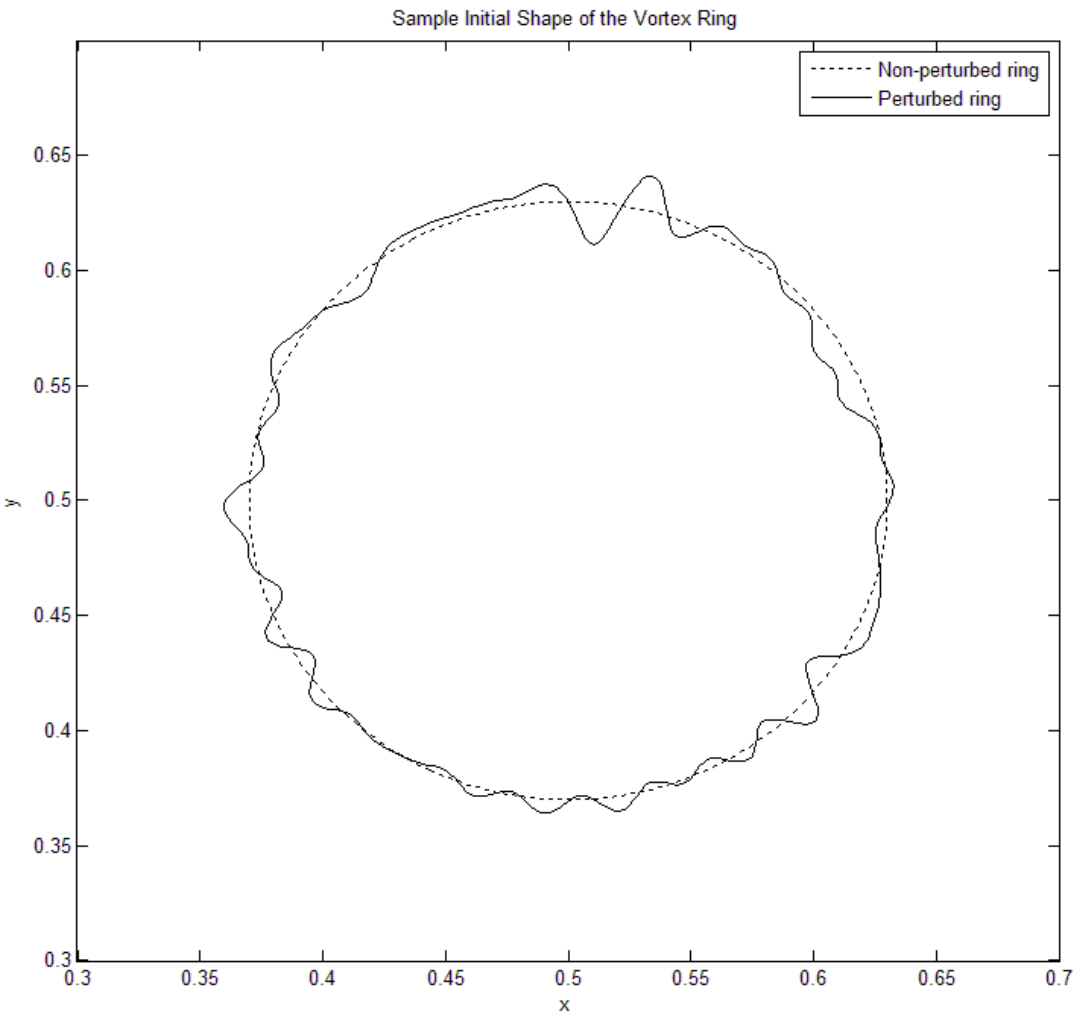

Figure 10. Example of how the 30 wave-number perturbation could change the shape of the vortex ring core. The dashed line represents the center of the core in a non-perturbed case, and the solid ring represents the center of the core with the wave-number perturbation applied.

3.2.2 "Wave-number" Perturbation

The second type of perturbation that was used involved changing the location of the vorticity instead of the magnitude. Unlike the random perturbation which perturbed the vorticity all throughout the domain, the wave-number perturbation focused on perturbing the core of the vortex ring. Waves of vorticity were added to the vortex ring core, similar to Shariff, Verzicco, & Orlandi (1994). 30 wave-numbers were added to the ring, each having the same amplitude and each having a random phase. The highest wave-number found in the experiment from Peck & Sigurdson (1994) was 28, so adding 30 wave-numbers was decided to be sufficient. The waves were added by shifting the location of the vorticity in the ring, based on the phase of the wave being added. This was repeated for each of the waves. The amplitude of each wave-number was based on the radius of the vortex ring, and was 1% of the radius of the ring for the majority of the simulations attempted. Since the phase was random, each simulation had a different perturbation. For an example of what this perturbation might look like, see Figure 10.

3.3 Turbulence Regimes

Most of the simulations were run at two different Reynolds numbers. Calculated from the circulation as in Equation (11), the two Reynolds numbers were 1400 and 2500.

$$\mathrm{Re} = \frac{\Gamma}{\nu} \tag{11}$$

where Γ is the circulation and ν is the kinematic viscosity. The two Reynolds numbers were chosen from data in Peck & Sigurdson (1994) in order to best re-create the vortex rings from the experiment.

Maxworthy (1972) described different regimes for vortex rings based on "bubble Reynolds number", where rings with Re < 600 were stable, rings between Re =

600 and Re = 1000 begin to become unstable, and rings with Re > 1000 are initially unstable but emerge from the disorganized flow as a new stable vortex ring. Using Maxworthy's bubble Reynolds number calculated from the diameter of the ring and the initial velocity as in Equation (12), the two Reynolds numbers for our simulations were 714 and 1275.

$$\mathrm{Re}_0 = \frac{U_0 D_0}{\nu} \tag{12}$$

where U_0 is the initial velocity of translation and D_0 is the initial diameter of the bubble.

Since the calculation of the initial velocity of translation was taken from the first two time steps of our simulations and the ring is decelerating, having smaller time steps or earlier time steps would cause the bubble Reynolds number to be higher. From Maxworthy's definitions we would therefore expect our simulations of both Reynolds numbers to produce unstable rings with the higher Reynolds number producing a more disorganized ring.

Dziedzic & Leutheusser (1996) also came up with a classification for vortex rings based on Reynolds number. Using the bubble Reynolds number from Maxworthy, they suggested that below Re = 1000, vortex rings were laminar, between Re = 1000 and Re = 2000 vortex rings exhibited a waviness in the core, and above Re = 2000 the vortex rings would have a turbulent wake and possibly a turbulent core. According to their definition, the lower Reynolds number used in our simulations would cause laminar rings, and the higher Reynolds number used in our simulations would produce rings with wavy cores.

4. Results & Discussion

4.1 Solitary Ring

To see if the vortex ring would go unstable by itself, with no other opposite-signed vorticity present, simulations were done with a solitary vortex ring. The perturbation used on the solitary ring was the wave perturbation outlined in Section 3.2.2 where 30 wave-numbers of equal amplitude and random phase were added.

In this section the simulations are visualized using isosurfaces of total vorticity magnitude. The isosurface is a surface where every point has the same vorticity level; it is essentially a contour line expanded into three dimensions. As the surface is for a set vorticity level, you can often infer that thicker areas on the isosurface have higher levels of vorticity contained within.

In these simulations there appear to be four loops of vorticity wrapped around the primary ring; two on the front and two on the back, though the loops on the back are not visible in Figure 11. These loops of vorticity appear similar to the bracelet structure, though due to their small amplitude they are difficult to visualize with isosurfaces for the Re = 1400 case. Four regions of streamwise vorticity are visible in the wake, two of which are much stronger than the other two.

The Reynolds number was increased from 1400 to 2500 to see the effect on the instability. The larger Reynolds number amplifies the instability. The bracelet structure is much more pronounced than in the Re = 1400 case and much easier to visualize with isosurfaces. Two loops of vorticity are visible on the front of the ring in Figure 12, and another two are on the back of the ring, though not easily visible in the Figure. Four regions of streamwise vorticity are visible in the wake, like in the Re = 1400 case.

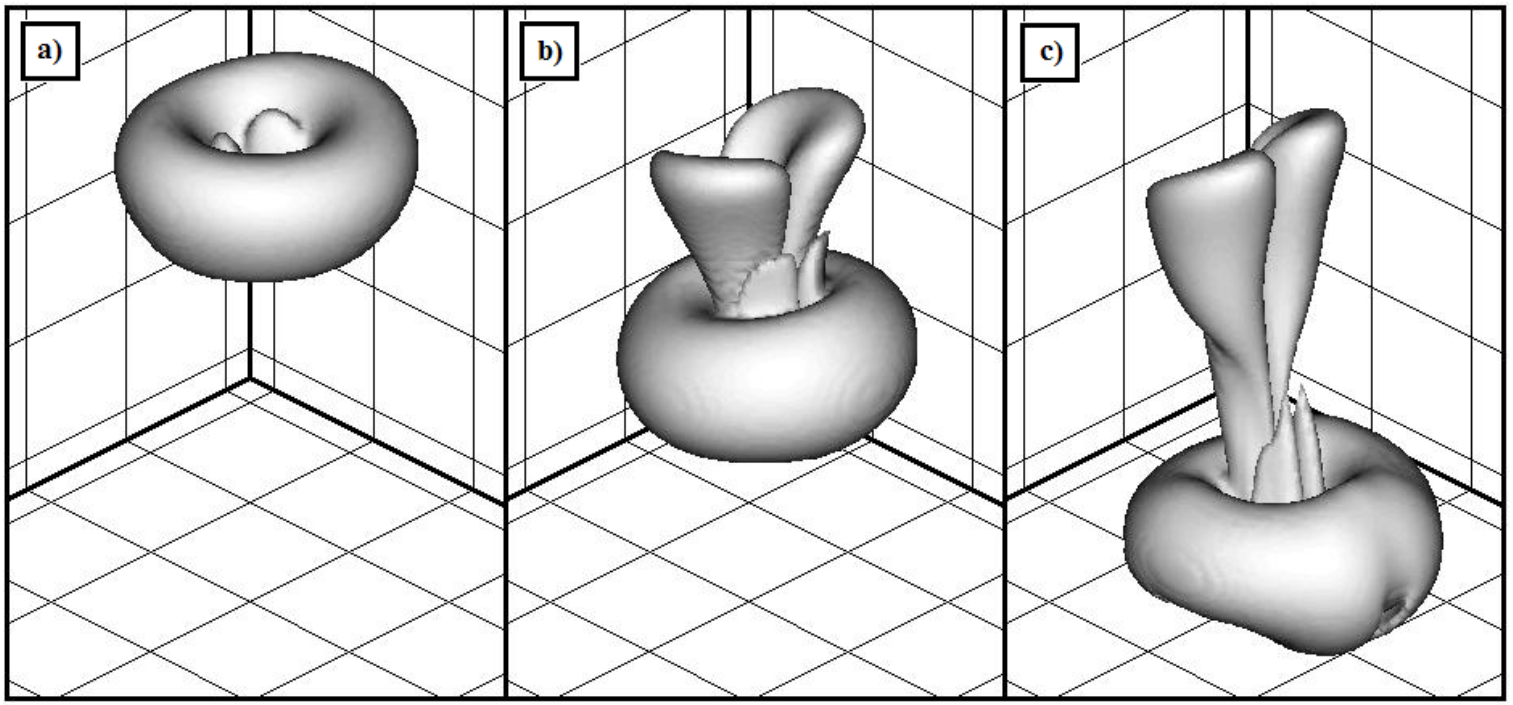

Figure 11. Solitary vortex ring with wave-number perturbation, Re = 1400. The ring convects downwards, leaving a wake of streamwise vorticity behind. In image **c)** a small bracelet structure is visible on the front-right of the ring. Image **a)** corresponds to t = 0.004s, **b)** corresponds to t = 0.02s, and **c)** corresponds to t = 0.04s. Isosurface is of total vorticity magnitude, level is $\omega = 100\ s^{-1}$.

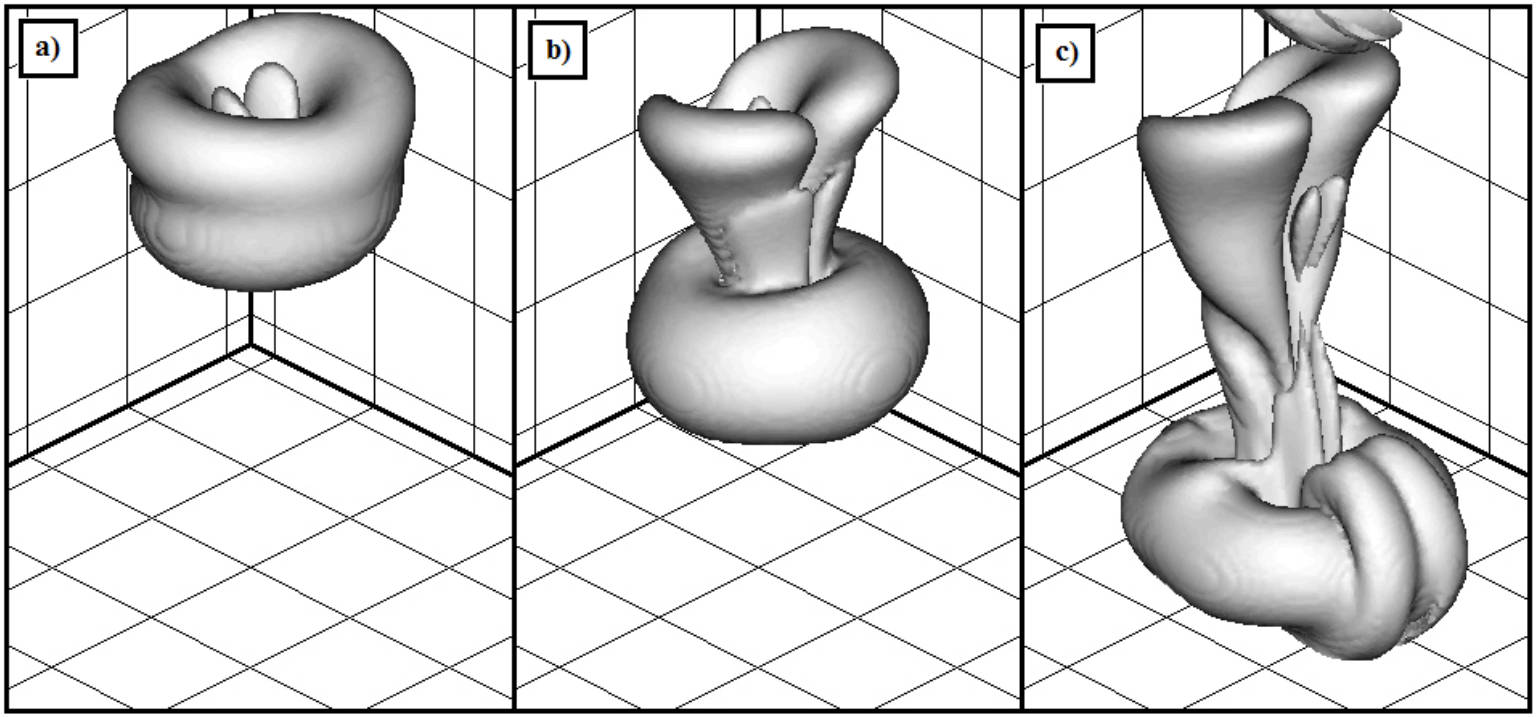

Figure 12. Solitary vortex ring with wave-number perturbation, Re = 2500. Results are similar to Figure 11, however the instability is more pronounced. In the third image, a bracelet structure is visible. Image **a)** corresponds to t = 0.004s, **b)** corresponds to t = 0.012s, and **c)** corresponds to t = 0.024s. Isosurface is of total vorticity magnitude, level is $\omega = 150\ s^{-1}$.

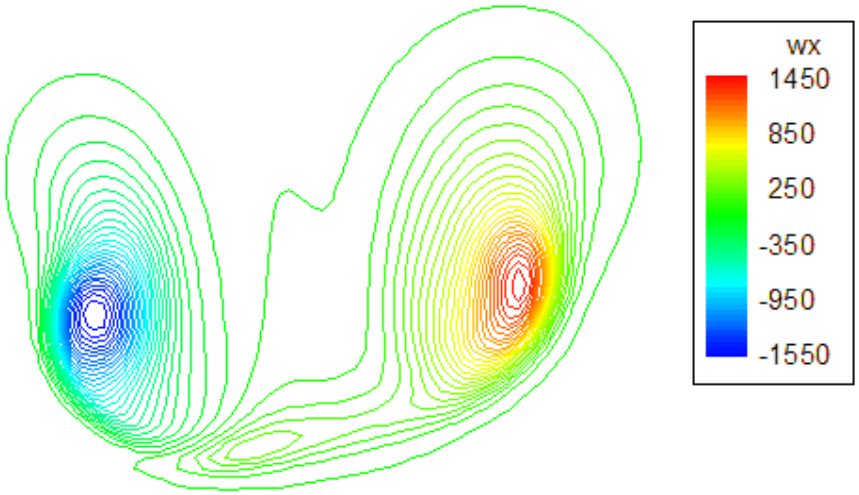

Figure 13. Contour plot of ω_x in the y-z plane showing the elliptical shape of the core and the slant of the core. Re = 1400, t = 0.06s, $\Delta z/d$ = 2.3.

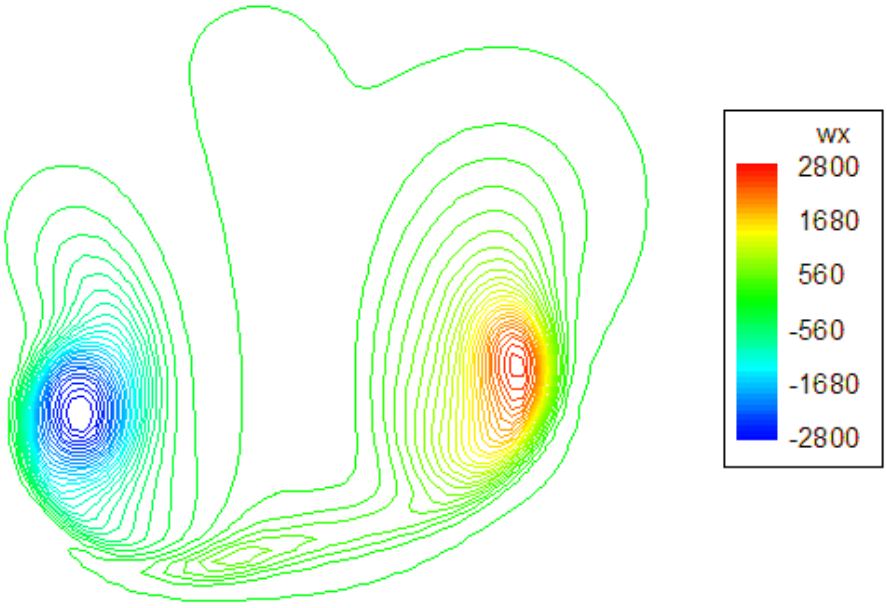

Figure 14. Contour plot of ω_x in the y-z plane showing the elliptical shape of the core and the slant of the core. Re = 2500, t = 0.04s, $\Delta z/d$ = 2.5.

Contour plots of the x vorticity on the y-z plane were performed to visualize the shape of the core of the vortex ring. At early times for both Reynolds numbers, the core is visibly elliptical instead of being circular as the initial condition of the ring was. Also, the two parts of the core cut by the plane are separated in the z-direction, which represents a slant of the plane of the core. The implications of this observation are discussed in Section 4.6.4. For the contour plot at Re = 1400 see Figure 13, and for the similar contour plot at Re = 2500, see Figure 14.

4.2 Opposite-Signed Ring

A smaller ring of opposite-signed vorticity, henceforth referred to as the "opposite-signed ring", was added above the primary ring to attempt to make it Rayleigh unstable. The circulation of the opposite-signed ring was varied, along with the perturbation imposed on the system.

4.2.1 15% Circulation

The first simulations used an opposite-signed ring with a circulation that was 15% of the primary ring's circulation. Some of the simulations in this section were run with no perturbation to the vorticity; others used the random perturbation described in Section 3.2. The random perturbation was based on both the local vorticity and the global vorticity, and was at most 10% of the local vorticity. These simulations were run at a Reynolds number of 1400.

In these simulations with the random perturbation, the bracelet structure does not appear. The opposite-signed ring initially passes down through the inside of the primary ring. As it emerges from the bottom of the primary ring its diameter increases, its velocity decreases, and it passes around the outside of the primary ring and gets left behind. This is similar to the "leapfrogging" behaviour that happens with two vortex rings traveling along the same centerline, however in this case only one leapfrog is observed. A wake of streamwise vorticity is visible trailing behind the primary ring. Both the primary ring and secondary ring remain axisymmetric. See Figure 15.

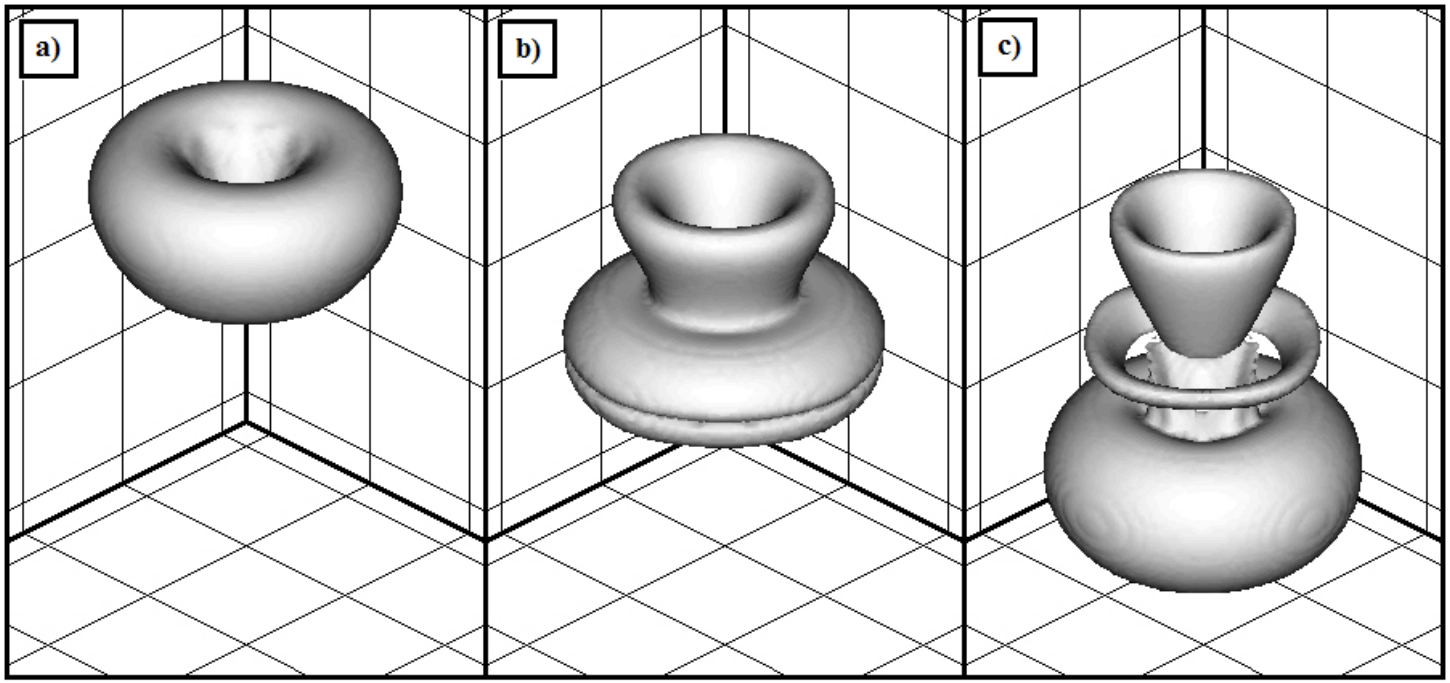

Figure 15. Opposite-signed secondary vortex ring with 15% of the primary ring's circulation, random perturbation, Re = 1400. In image **b)** the opposite-signed ring is looping around the primary ring, and in image **c)** it has been left behind the primary ring. Image **a)** corresponds to t = 0.04s, **b)** corresponds to t = 0.16s, and **c)** corresponds to t = 0.32s. Isosurface is of total vorticity magnitude, level is $\omega = 5\ s^{-1}$.

4.2.2 30% Circulation

The circulation of the opposite-signed ring was increased to 30% of the circulation of the primary ring. This was done to see if the forcing provided by the opposite-signed vorticity was insufficient to produce the bracelet structure simply because the amplitude was too small. The random perturbation described in Section 3.2.1 was used, limited to a maximum 10% of the local vorticity. In this case the structure appears similar to simulations run in the previous section with the secondary ring circulation being 15% of the primary ring circulation. Unlike the previous simulation however, the secondary ring appears to lose its symmetry and becomes wavy after leapfrogging around the primary ring. The primary ring remains axisymmetric and does not develop the bracelet structure. See Figure 16.

4.2.3 30% Circulation with 30 Wave-Number Perturbation

Since increasing the circulation of the opposite-signed ring did not cause the bracelet structure to appear, the next simulations changed the way the vorticity was perturbed. In these simulations, 30 wave-numbers were added to the primary ring, each having a random phase and each having the same amplitude. This perturbation is described in Section 3.2.2.

This time the primary ring is no longer axisymmetric, and an instability is clearly visible which looks similar to the bracelet structure. Loops of vorticity appear to form from the primary ring, and as the primary ring continues to travel downwards, the loops trail behind the primary ring and wrap around the secondary ring. Two regions of streamwise vorticity are visible in the wake of the primary ring. See Figure 17.

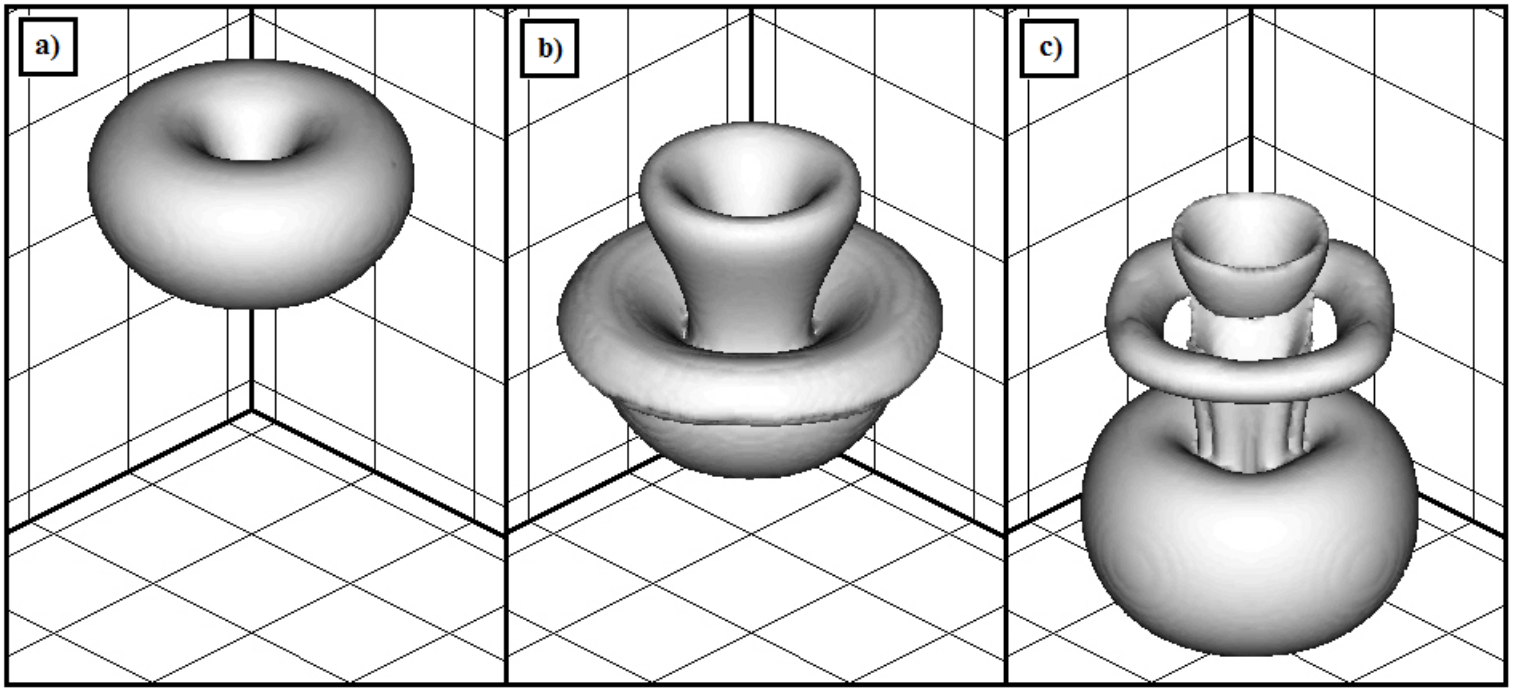

Figure 16. Opposite-signed secondary vortex ring with 30% of the primary ring's circulation, random perturbation, Re = 1400. In image **b)** the opposite-signed ring is looping around the primary ring, and in image **c)** it has been left behind the primary ring. Unlike Figure 15, the secondary ring becomes wavy in image **c)**. Image **a)** corresponds to t = 0.004s, **b)** corresponds to t = 0.024s, and **c)** corresponds to t = 0.052s. Isosurface is of total vorticity magnitude, level is $\omega = 30\ s^{-1}$.

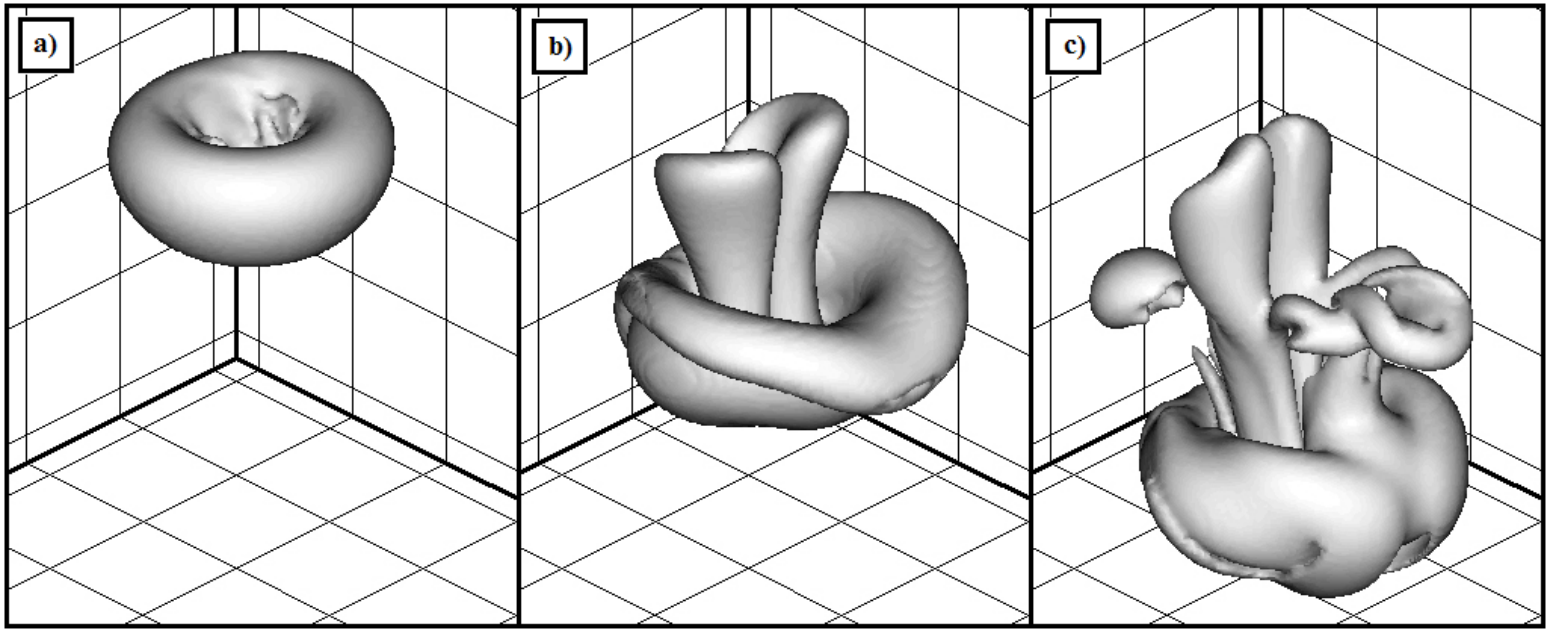

Figure 17. Opposite-signed secondary vortex ring with 30% of the primary ring's circulation, wave-number perturbation, Re = 1400. In image **b)** the opposite-signed ring is looping around the primary ring, and in image **c)** it has been left behind the primary ring. Bracelet structures are visible on the primary ring, and loops of vorticity appear to trail behind the primary ring and wrap around the secondary ring. Image **a)** corresponds to t = 0.004s, **b)** corresponds to t = 0.028s, and **c)** corresponds to t = 0.06s. Isosurface is of total vorticity magnitude, level is $\omega = 100\ s^{-1}$.

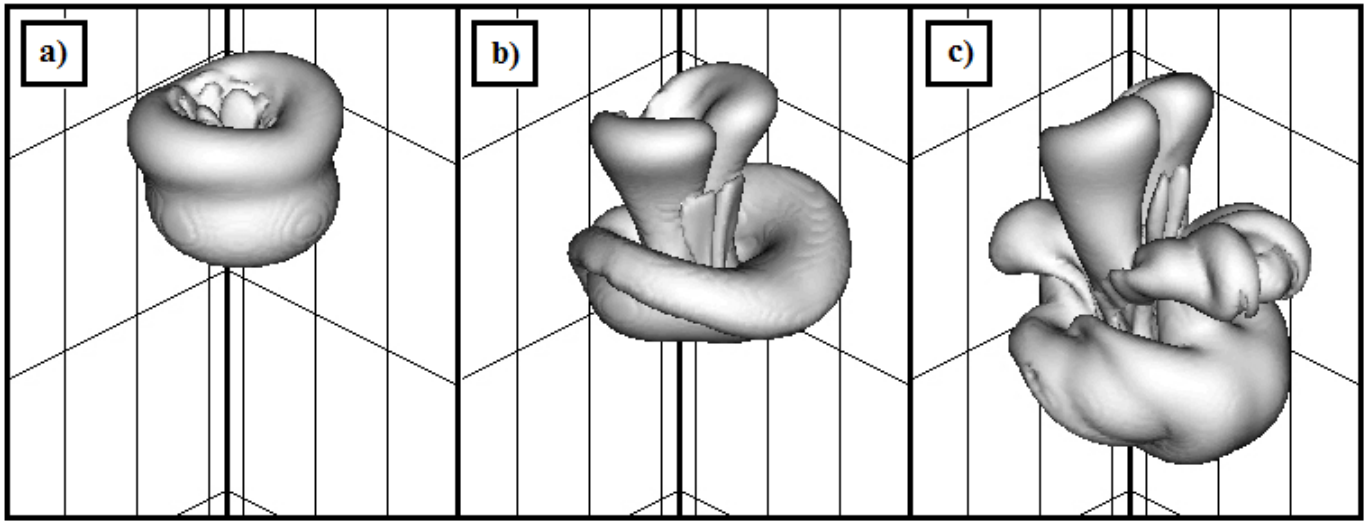

Figure 18. Opposite-signed secondary vortex ring with 30% of the primary ring's circulation, wave-number perturbation, Re = 2500. In image **b)** the opposite-signed ring is looping around the primary ring, and in image **c)** it has been left behind the primary ring. Bracelet structures are visible on the primary ring, and loops of vorticity appear to trail behind the primary ring and wrap around the secondary ring. Image **a)** corresponds to t = 0.005s, **b)** corresponds to t = 0.015s, and **c)** corresponds to t = 0.03s. Isosurface is of total vorticity magnitude, level is $\omega = 150\ s^{-1}$.

The Reynolds number was increased from 1400 to 2500 to see the effect on the instability. The primary ring is again not axisymmetric, and the instabilities appear more pronounced than in the previous simulations done at Re = 1400, which would be expected due to the higher Reynolds number. An instability is visible on the primary ring, which appears similar to the bracelet structure. The loops of vorticity trailing behind the primary ring again wrap around the secondary ring. Like the simulations done at Re = 1400, two regions of streamwise vorticity are visible in the wake. See Figure 18.

4.3 Vortex Breakdown

An image vortex ring was added above the primary ring to see if perhaps the contraction of the primary ring diameter, which was observed experimentally, contributes to the formation of the bracelet structure. The image vortex is placed at varying distances from the primary ring, to cause the ring to contract. Placing the image vortex closer to the primary ring will increase the amount of contraction; however it will also cause the shape of the vortex ring core to change. Care was taken to avoid excessive deformation of the core, which could also be the source of a different instability. The result is similar to the simulations discussed in Section 3.1.1 at Re = 1400. A small bracelet structure is apparent on the vortex ring, and four regions of streamwise vorticity are visible in the wake. See Figure 19.

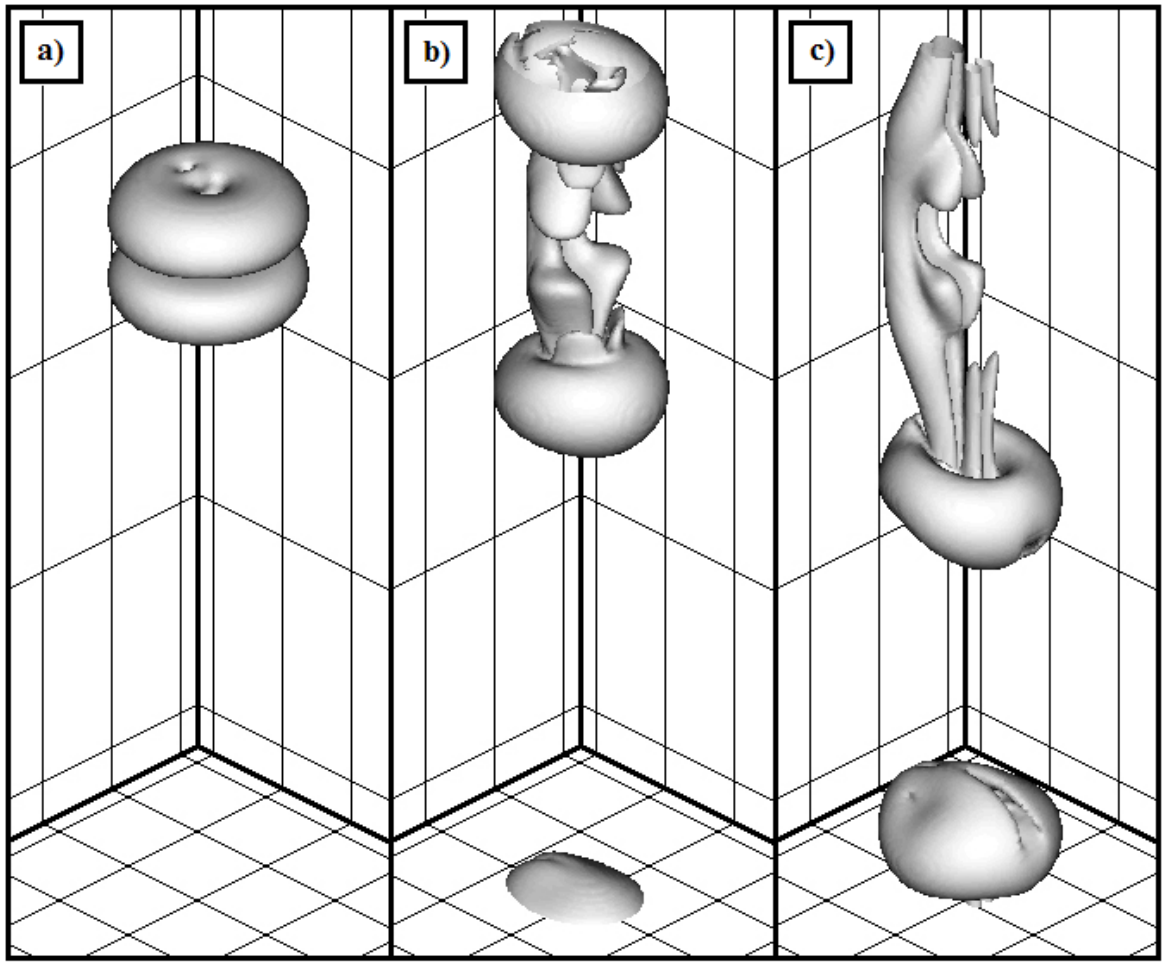

Figure 19. Image vortex ring is placed above the primary ring, Re = 1400. In image **b)** the two rings are convecting away from each other. In image **c)** a small bracelet structure is visible on each ring. Due to the periodic boundary conditions, vorticity passing out of the top of the domain enters back into the bottom of the domain, and vorticity passing out of the bottom enters back into the top. Image **a)** corresponds to t = 0.002s, **b)** corresponds to t = 0.02s, and **c)** corresponds to t = 0.04s. Isosurface is of total vorticity magnitude, level is $\omega = 100\ s^{-1}$.

4.4 Skeleton Vortex Structure

To attempt to follow the evolution of the instabilities, vortex lines were calculated using Tecplot for several time steps and locations. Vortex lines are lines that are everywhere tangent to the vorticity. The time evolution of the vortex lines was observed to see how they changed, and the vortex lines were matched up to features visible in the isosurfaces of vorticity. It is possible to compare the vortex lines created here to the proposed model from Peck & Sigurdson (1994), which is shown in Figure 20.

To choose the location of the vortex lines, a slice was taken in the y-z plane, and the locations of the maximum and minimum x-vorticity were found, which would correspond to the center of the vortex ring core. The z values of the maximum and minimum were averaged, and this location was used to create a slice in the x-y plane. A contour plot of the z-vorticity was created on this plane, and the local minima and maxima were found. These local minima and maxima were used as the starting points for the vortex lines.

This analysis was performed for the solitary ring simulations at both Re = 1400 and Re = 2500, using the wave-number perturbation. Only the higher Reynolds number results are presented here as they both resulted in very similar vortex lines. The analysis was not performed for the other simulations as the presence of the other vorticity complicated the process; there were too many local minimums and maximums on the contour plot, and tracking the vortex lines between time steps became too difficult.

Three vortex lines were found that were of particular interest. Two of the vortex lines corresponded to a wave number of one, and will therefore be referred to as vortex lines 1a and 1b. The third vortex line corresponded to a wave number of two, and will be referred to as vortex line 2. See Figure 21 for a sample contour plot used to find the starting positions of the vortex lines.

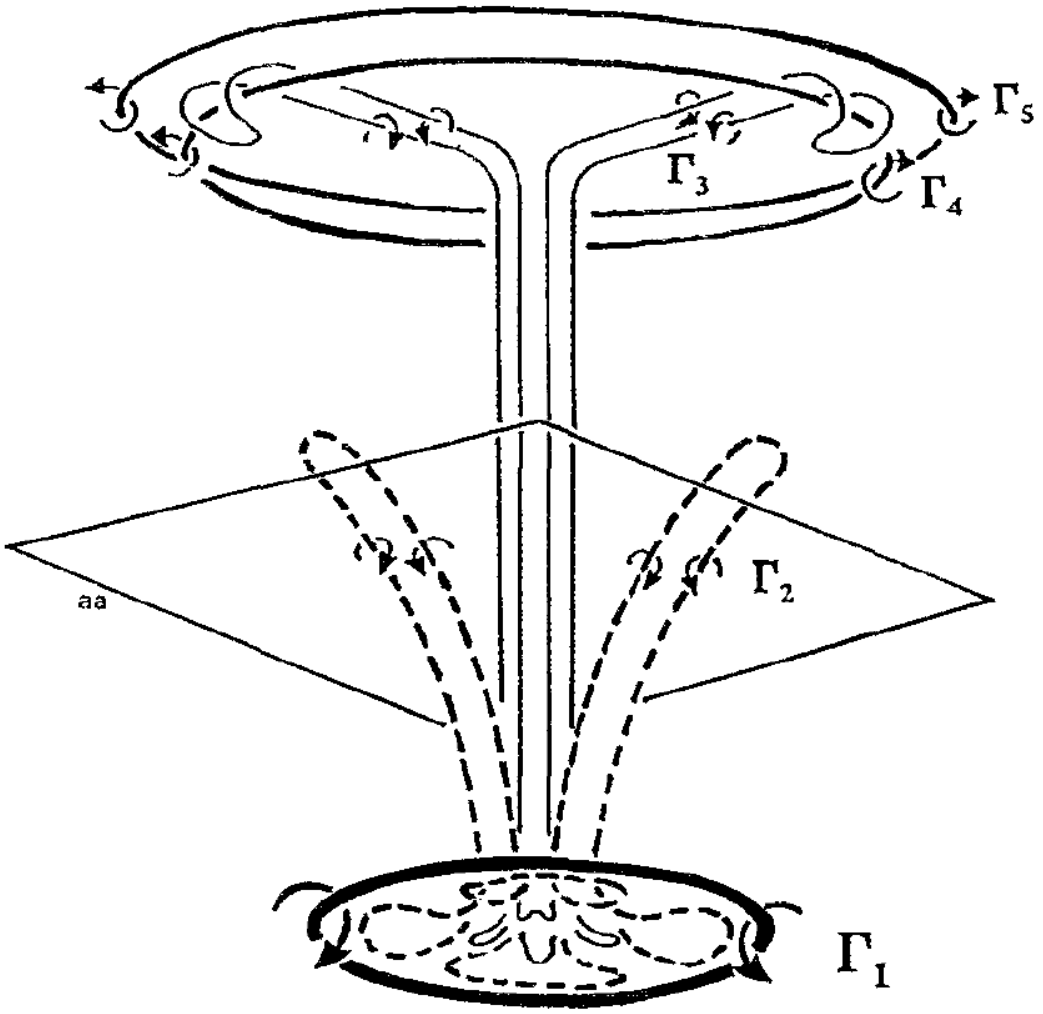

Figure 20. The three-dimensional vortex skeleton proposed by Peck & Sigurdson (1994). For clarity, only two "petals" and two portions of the "stalk" are shown. Reused with permission from the American Institute of Physics.

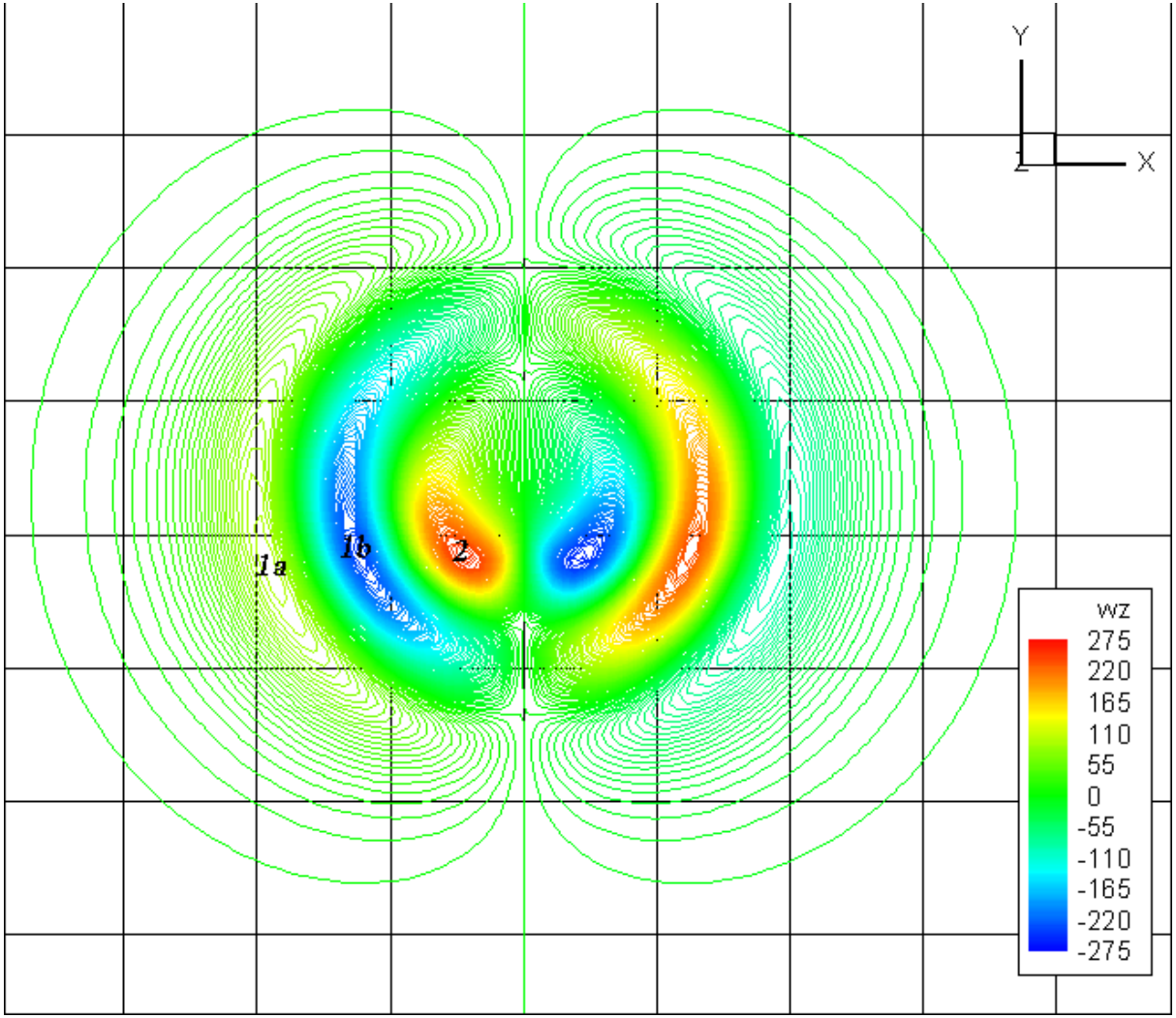

Figure 21. Sample contour plot used to choose starting points for the vortex lines. Locations 1a, 1b, and 2 were chosen as the starting points as they correspond to local minima and maxima of z-vorticity.

The evolution of the vortex lines was observed by creating similar contour plots at later time steps and again using the local minimums and maximums as starting points for vortex lines. As time progressed, however, more local minimums and maximums were visible in the contour plots. This was inferred to be due to the rotation of the vortex ring core, which could pull the z-vorticity around to the opposite side of the core, creating another pair containing a minimum and maximum. The rotation speed of the approximately solid body rotation portion of the core was calculated, and it was found to go through about half a rotation between each observed time step. This would suggest that the rotation of the core is the primary cause of the increased number of local minimums and maximums.

The evolution of vortex line 1a is shown in Figure 22. At the earliest time step available it appears as a round loop which is bent in half, with the rear half of the loop pointing down and the front half of the loop lying approximately along the x-y plane. As time progresses, the loop seems to be pulled around by the rotation of the vortex ring, giving the loop more of an “S” shape. Vortex line 1a seems to evolve into the smaller part of the stalk visible in isosurfaces of the vorticity in Section 3.3.1.

The evolution of vortex line 1b is shown in Figure 23. Vortex line 1b begins as a round loop which has been rotated slightly, in the opposite direction of vortex line 1a. As time progresses, the loop stretches out, and similar to vortex line 1a it develops an “S” shape. Eventually the back-end of the loop doesn’t close on itself any more, and the vortex lines run off to the edges of the simulated volume. This is likely due to the integration in Tecplot not being able to perfectly track the vortex line with the available grid resolution. The front end of the loop appears to begin to wrap around the vortex ring, and seems to create the bracelet structure on the front of the vortex ring which is visible in the isosurface images.

The evolution of vortex line 2 is shown in Figure 24. As vortex line 2 has a wave number of two, the shape is more complicated than vortex lines 1a and 1b, even

from the earliest available time step. The loop extends down at the back, has its high point in the middle, and extends down again in the front. At later time steps, the loop gets stretched out, and the part towards the back begins to get pulled around the vortex ring. The high points of the loop appear to form the large part of the stalk seen in the isosurface images in Section 4.1, while the rear part of the loop appears to form the bracelet structure visible at the back of the vortex ring.

a) Time = 0.001s b) Time = 0.005s c) Time = 0.009s

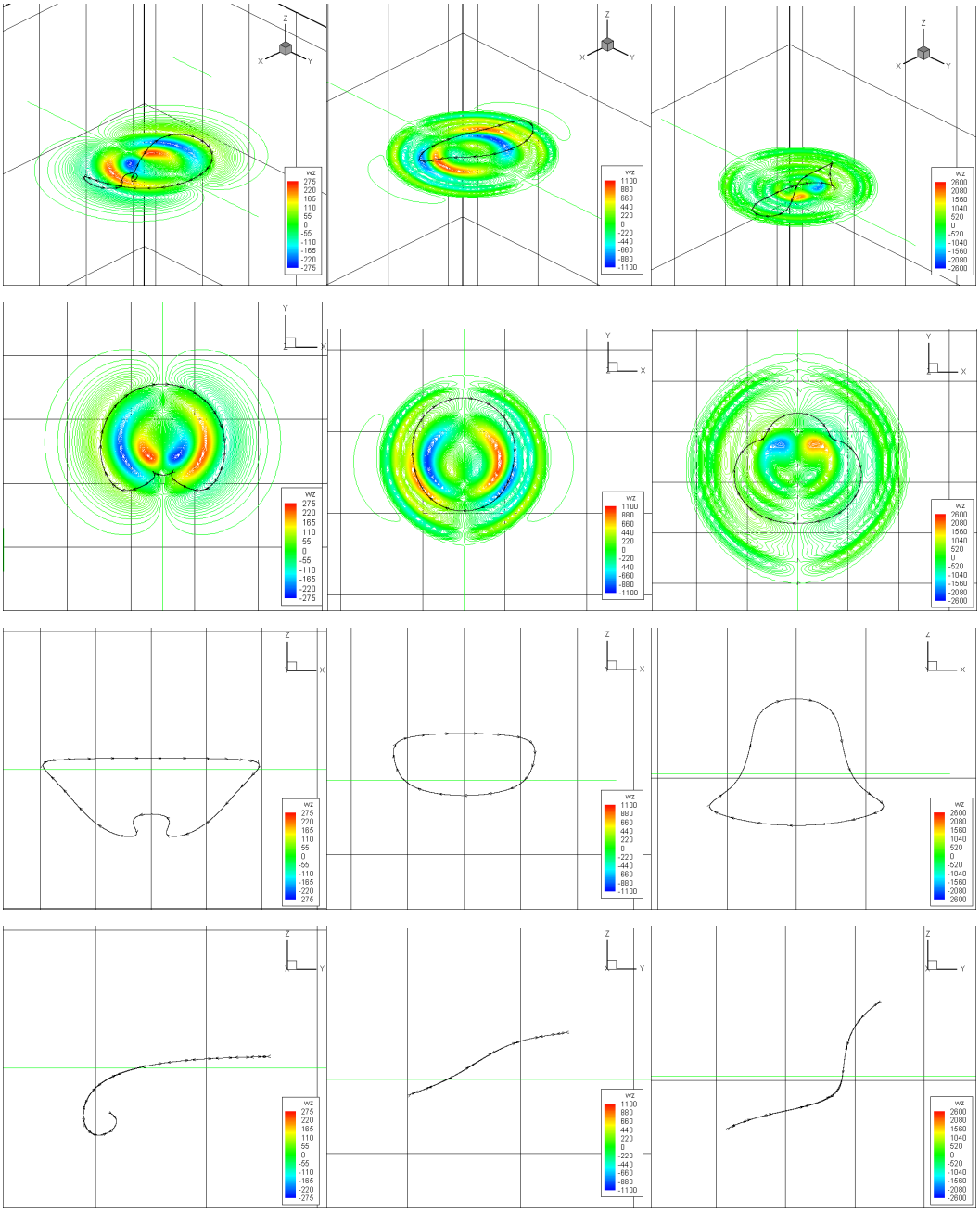

Figure 22. The evolution of vortex line 1a. The first column corresponds to t = 0.001s, the second column corresponds to t = 0.005s, and the third column corresponds to t = 0.009s. The first row shows the isometric view, the second row shows the x-y view (looking toward negative z), the third row shows the x-z view (looking toward positive y), and the fourth row shows the y-z view (looking toward negative x).

a) Time = 0.001s b) Time = 0.005s c) Time = 0.009s

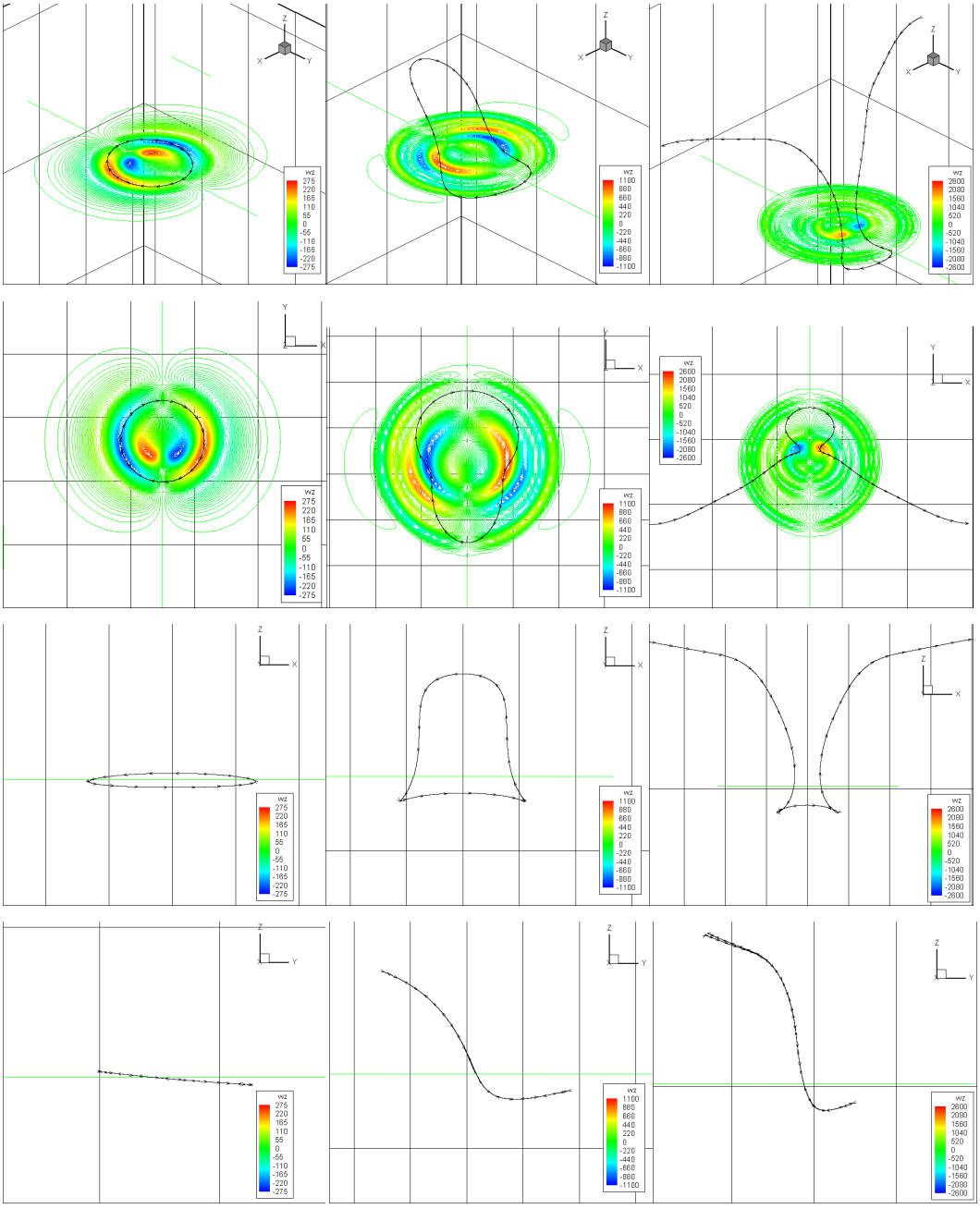

Figure 23. The evolution of vortex line 1b. The first column corresponds to t = 0.001s, the second column corresponds to t = 0.005s, and the third column corresponds to t = 0.009s. The first row shows the isometric view, the second row shows the x-y view (looking toward negative z), the third row shows the x-z view (looking toward positive y), and the fourth row shows the y-z view (looking toward negative x).

a) Time = 0.001s b) Time = 0.005s c) Time = 0.009s

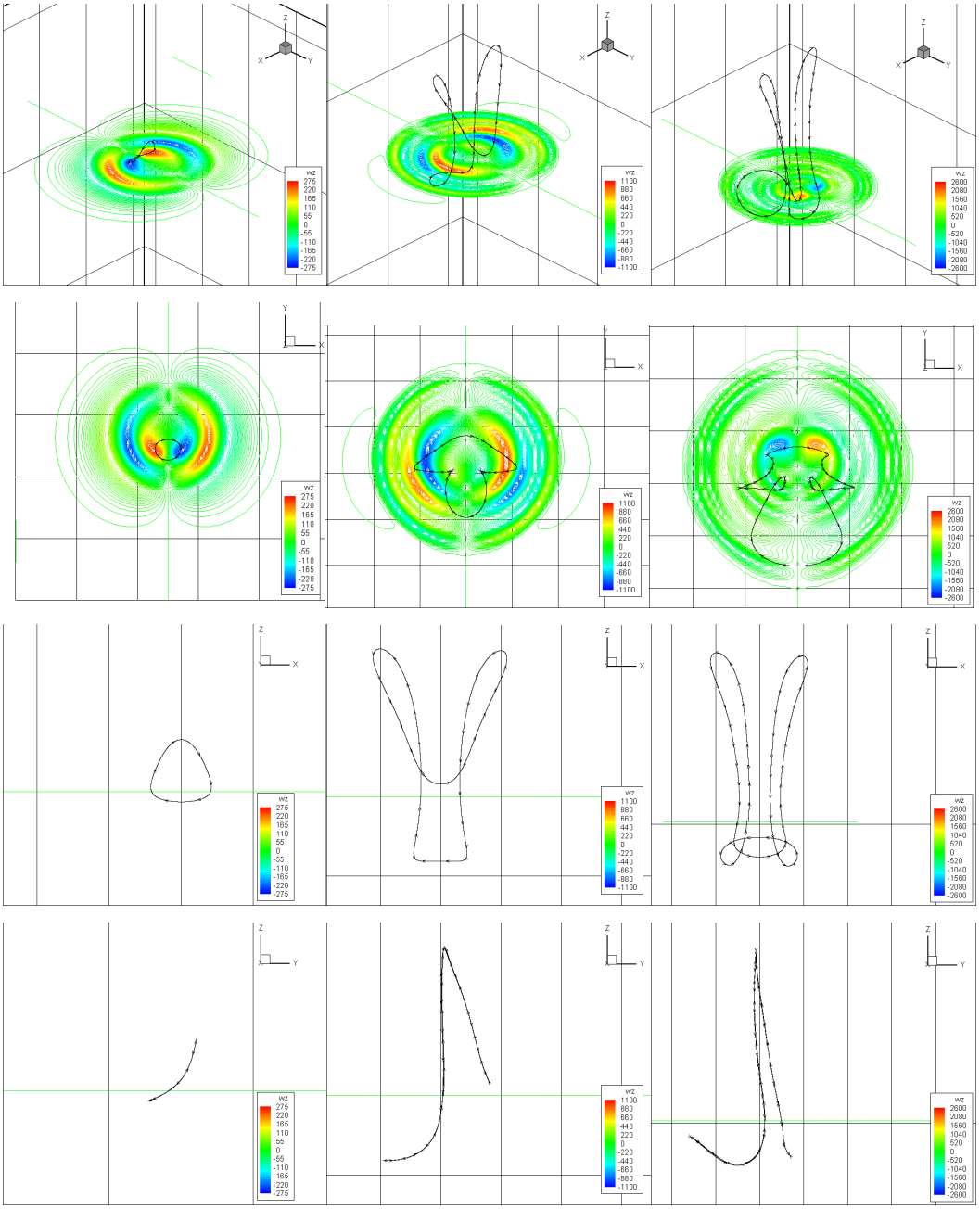

Figure 24. The evolution of vortex line 2. The first column corresponds to t = 0.001s, the second column corresponds to t = 0.005s, and the third column corresponds to t = 0.009s. The first row shows the isometric view, the second row shows the x-y view (looking toward negative z), the third row shows the x-z view (looking toward positive y), and the fourth row shows the y-z view (looking toward negative x).

4.5 Instability Growth

In order to examine the growth of each instability wave-number, slices of vorticity in the x-y plane were taken through the center of the vortex ring at each time step. The center was determined from the centroid, which was calculated from the magnitude of ω_x and ω_y. To limit the effect of the z-vorticity which composed the wake, ω_z was excluded, since the presence of the wake vorticity would influence the centroid to be above the expected center of the vortex ring. The x-y plane was then made to pass through the calculated centroid.

For each slice, vorticity data was taken azimuthally around the center of the vortex ring. A Fourier transform was performed on ω_r using the FFT function in MATLAB. This provided the amplitude and phase of each wave-number involved in the instability. For a non-perturbed ideal vortex ring, the radial vorticity would be zero around the azimuth, while for a perturbed ring the radial vorticity would be non-zero, which the Fourier transform would then break down into wave-numbers of varying amplitudes and phases. A sample of the FFT result for t = 0.001s is given in Figure 25. By performing this process on each time step, it was then possible to determine the growth rate in time of each individual wave-number. Since the centroid location for each time step was previously calculated, it was then possible to calculate the growth in space. This analysis was performed for the solitary ring simulations at both Re = 1400 and Re = 2500.

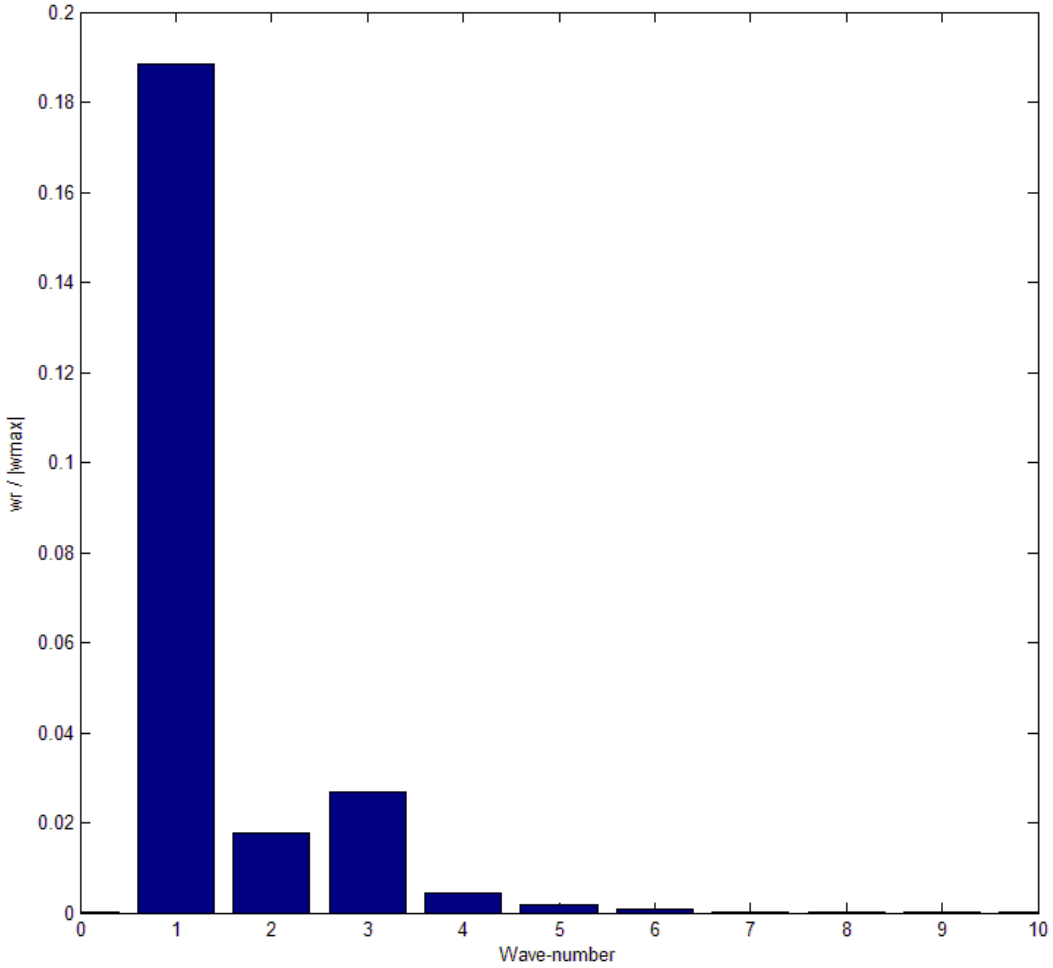

Figure 25. Sample Fourier transform result for t = 0.001s showing the amplitude of each wave-number. This process was then performed for every time step so that each individual wave-number could be analyzed.

For the Re = 1400 case, the growth of wave-numbers 1-3 are shown in Figure 26. The amplitudes of wave-numbers higher than 3 were less than 5% of the maximum vorticity on the plane and are not shown. The vertical axis was non-dimensionalized using the maximum vorticity magnitude around the azimuth of the vortex ring. This was chosen instead of the maximum radial vorticity because for an ideal vortex ring with no instability the radial vorticity would be zero, therefore the only radial vorticity present is due to the observed instabilities. Non-dimensionalizing with radial vorticity would give a comparison of each wave-number to the most amplified wave-number, with the most amplified wave-number having a value of 1. Non-dimensionalizing with the maximum vorticity magnitude gives a comparison of each wave-number to the maximum vorticity present, where a value of 1 would mean that the only vorticity present was that particular wave-number.

For the Re = 2500 case, the growth of wave-numbers 1-3 are shown in Figure 27, and wave-numbers 4-6 are shown in Figure 28. Unlike the Re = 1400 case, higher wave-numbers still have significant amplitudes. The wave-number amplitude does not drop below 5% of the max vorticity on the plane until wave-numbers past 18. To avoid clutter, wave-numbers up to 18 are available in Appendix 6. The axes are non-dimensionalized in the same way as the Re = 1400 case.

In both cases, wave-number 1 is dominant, and grows as the ring evolves. For the Re = 1400 case, wave-numbers 1 and 3 grow the most, while 2 stays comparatively low in magnitude. For the Re = 2500 case, all the shown wave-numbers have substantial peaks at various points but wave-number 1 is usually largest. Unlike with Re = 1400, the wave-numbers beyond 3 have significant amplitudes for the Re = 2500 case. This is likely due to the smaller-scale vorticity present with the higher Reynolds number.

A similar analysis was also performed on the Re = 1400 and Re = 2500 cases, but using ω_z instead of ω_r. Similar to the radial vorticity, for an ideal vortex ring with

no instability there would be no z-vorticity present, however in the simulations presented here and in the experiment from Peck and Sigurdson (1994), z-vorticity is seen in the wake and from the shedding of the "petals".

For the Re = 1400 case, the growth of wave-numbers 1-3 are shown in Figure 29, and wave-numbers 4-6 are shown in Figure 30. Wave-numbers past 6 have peak amplitudes of less than 5% of the max vorticity on the plane and are therefore excluded. The axes are non-dimensionalized in the same manner as the previous plots of ω_r.

For the Re = 2500 case, the growth of wave-numbers 1-3 are shown in Figure 31, and wave-numbers 4-6 are shown in Figure 32. As opposed to ω_z for Re = 1400, but similar to ω_r for Re = 2500, higher wave-numbers still have significant amplitudes. To aid in keeping the data readable, wave-numbers up to 18 are displayed in Appendix 7. The axes are non-dimensionalized in the same manner as the previous plots of ω_r.

Similar to the results of the wave-number analysis of ω_r, the wave-number 1 instability tends to dominate for both Re = 1400 and Re = 2500. In both cases it tends to peak early, then decline as the ring convects, though in the Re = 2500 case there are a few peaks. The wave-number 4 instability overcomes wave-number 1 at the end of the data for Re = 1400, and has a significant secondary peak in the Re = 2500 case. The Re = 2500 data has an interesting secondary peak at approximately $\Delta z/d = 3$, and most of the wave-numbers grow at approximately $\Delta z/d = 2.5$. The growth of the wave-number amplitudes at a later time could be due to the higher Reynolds number ring remaining turbulent instead of relaminarizing. The Re = 2500 data is also different from the Re = 1400 data in that higher wave-numbers seem to have non-trivial amplitudes. Similar to the analysis of ω_r, this could be due to the smaller vorticity scale at the higher Reynolds number which could show up as smaller waves and therefore higher wave-numbers.

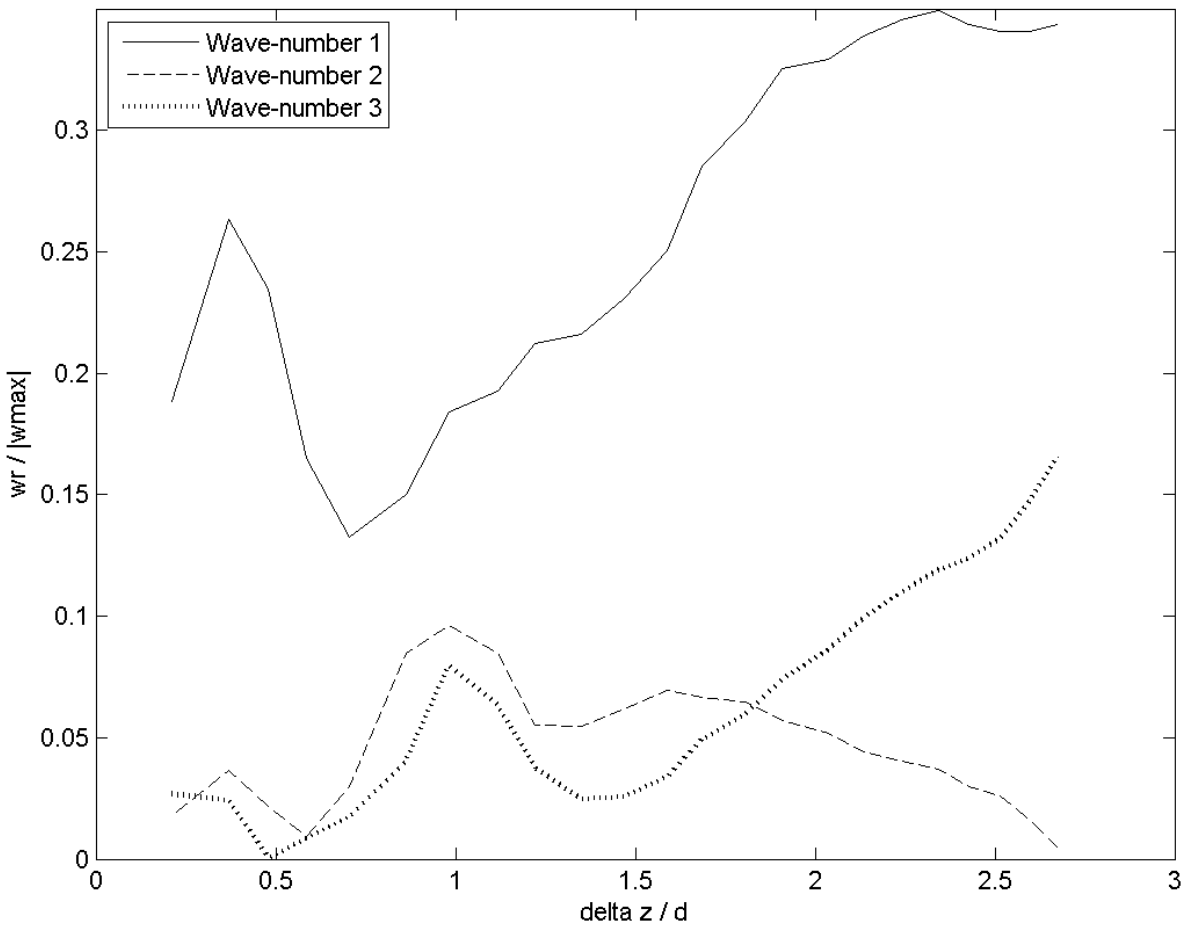

Figure 26. Instability growth of wave-numbers 1-3 for ω_r. The horizontal axis is the number of ring diameters the vortex ring has travelled. The vertical axis is the amplitude of the instability compared to the maximum vorticity magnitude around the azimuth of the vortex ring. Re = 1400, Solitary ring simulation with wave-number perturbation.

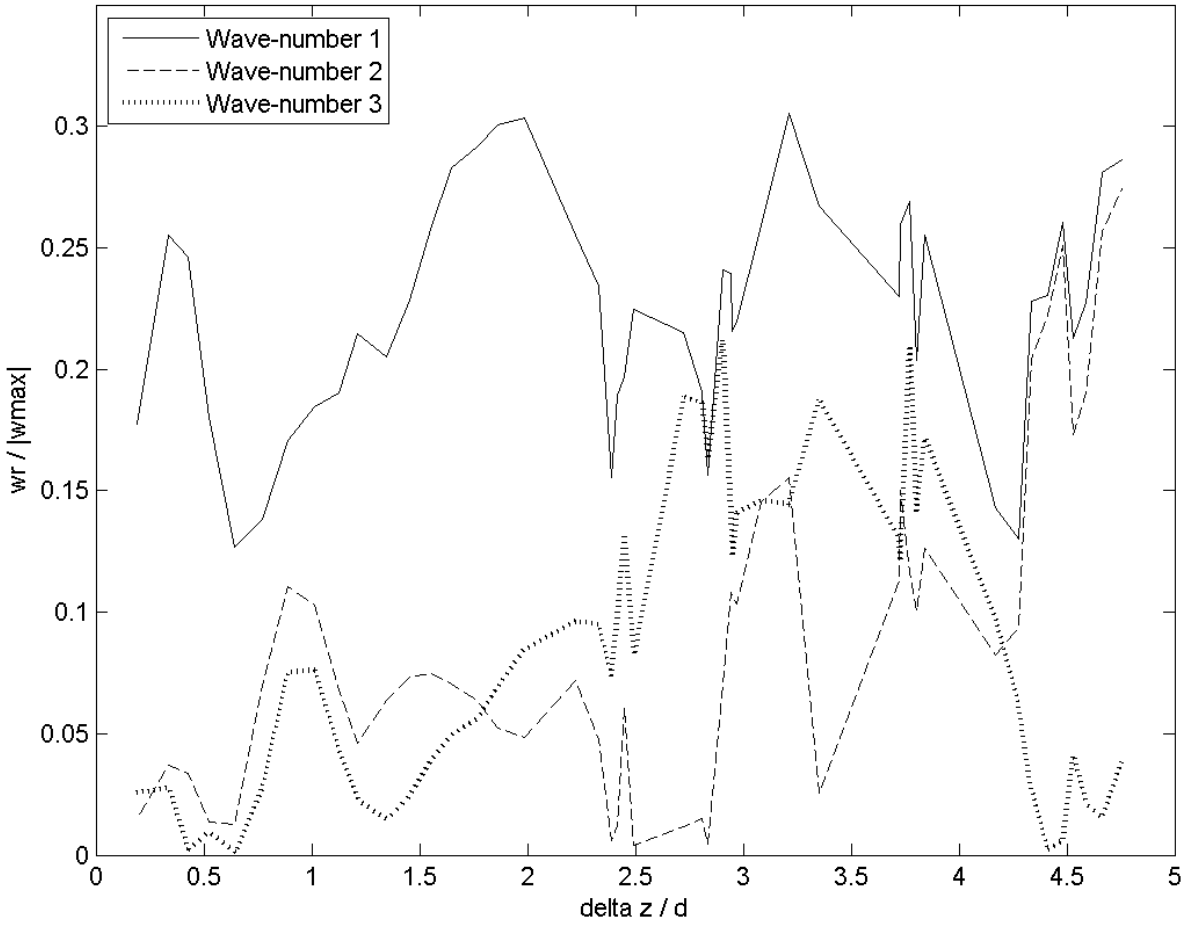

Figure 27. Instability growth of wave-numbers 1-3 for ω_r. The horizontal axis is the number of ring diameters the vortex ring has travelled. The vertical axis is the amplitude of the instability compared to the maximum vorticity magnitude around the azimuth of the vortex ring. Re = 2500, Solitary ring simulation with wave-number perturbation.

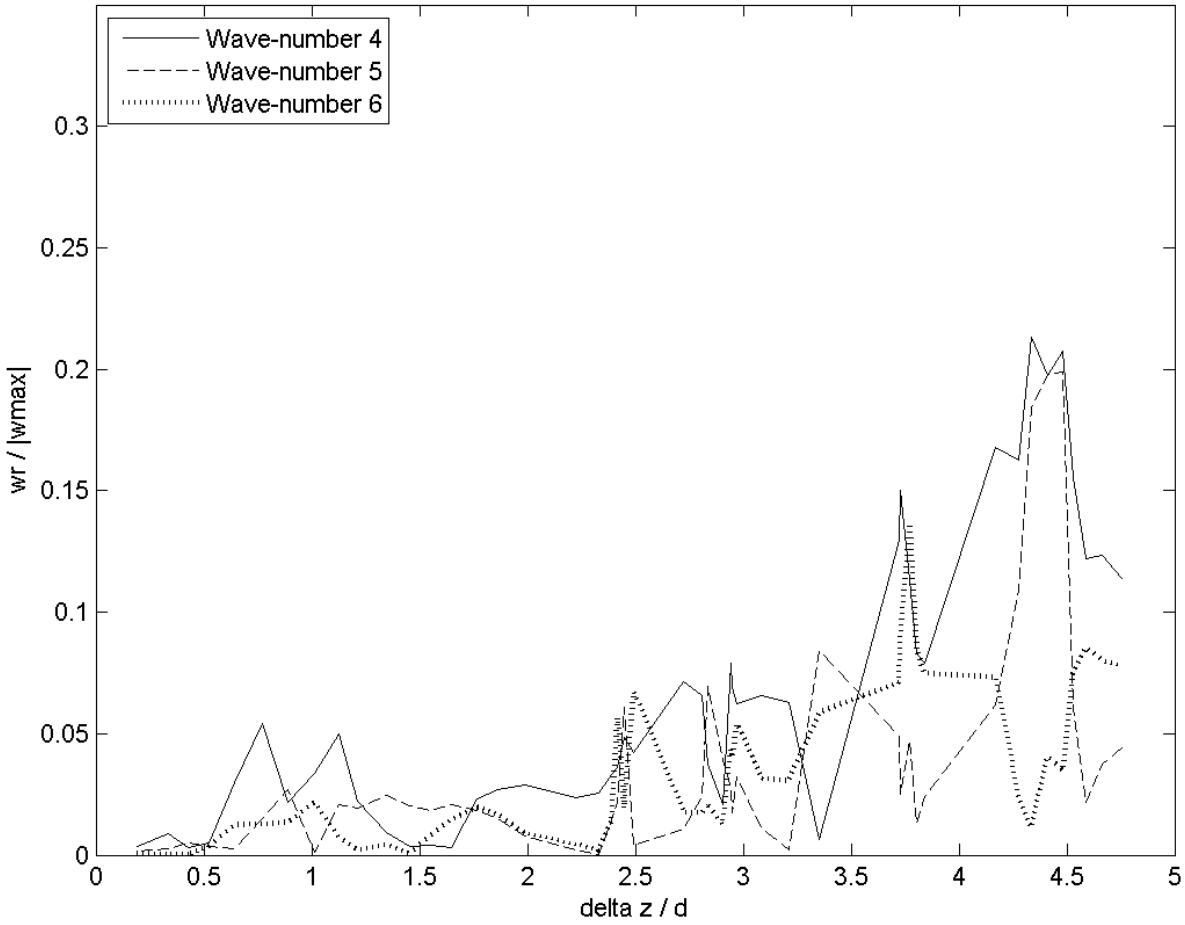

Figure 28. Instability growth of wave-numbers 4-6 for ω_r. The horizontal axis is the number of ring diameters the vortex ring has travelled. The vertical axis is the amplitude of the instability compared to the maximum vorticity magnitude around the azimuth of the vortex ring. Re = 2500, Solitary ring simulation with wave-number perturbation.

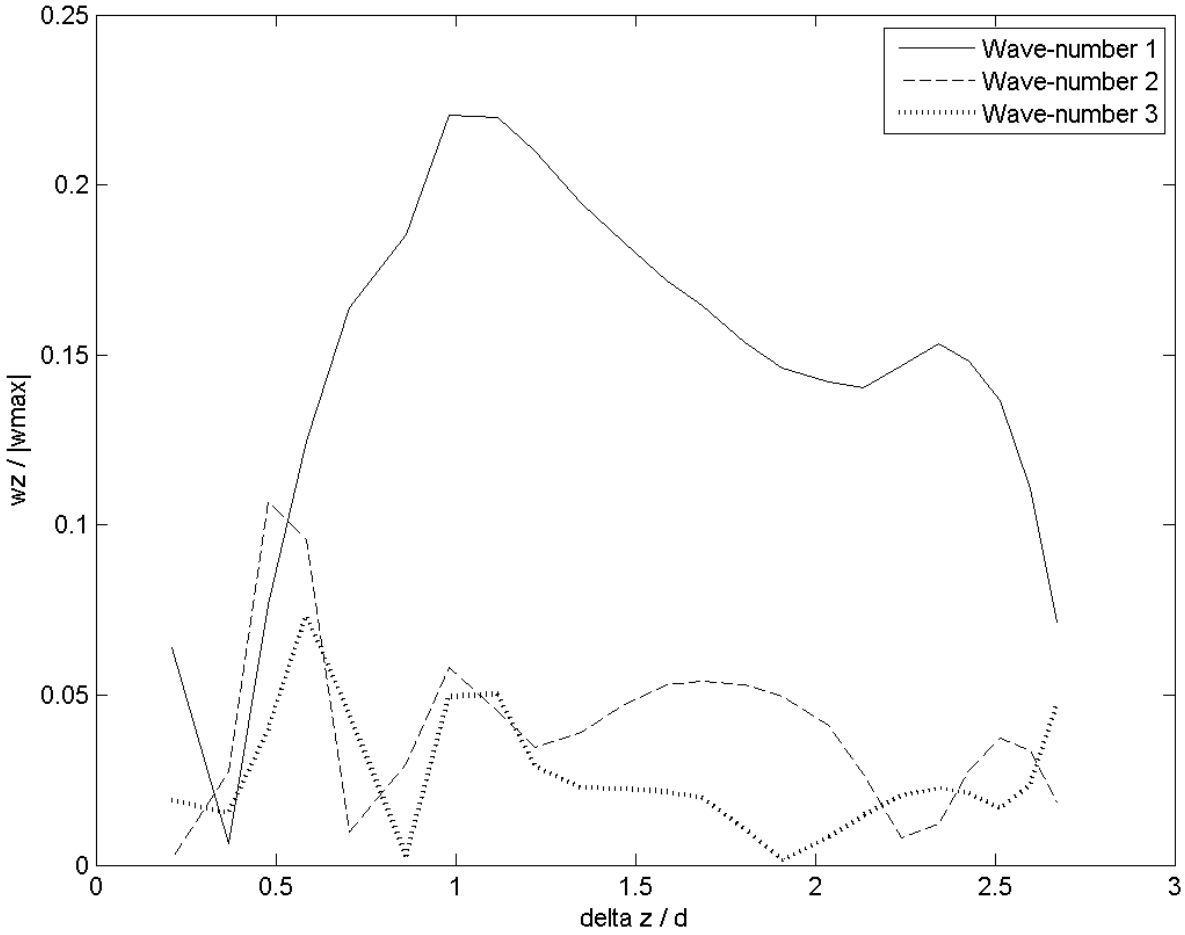

Figure 29. Instability growth of wave-numbers 1-3 for ω_z. The horizontal axis is the number of ring diameters the vortex ring has travelled. The vertical axis is the amplitude of the instability compared to the maximum vorticity magnitude around the azimuth of the vortex ring. Re = 1400, Solitary ring simulation with wave-number perturbation.

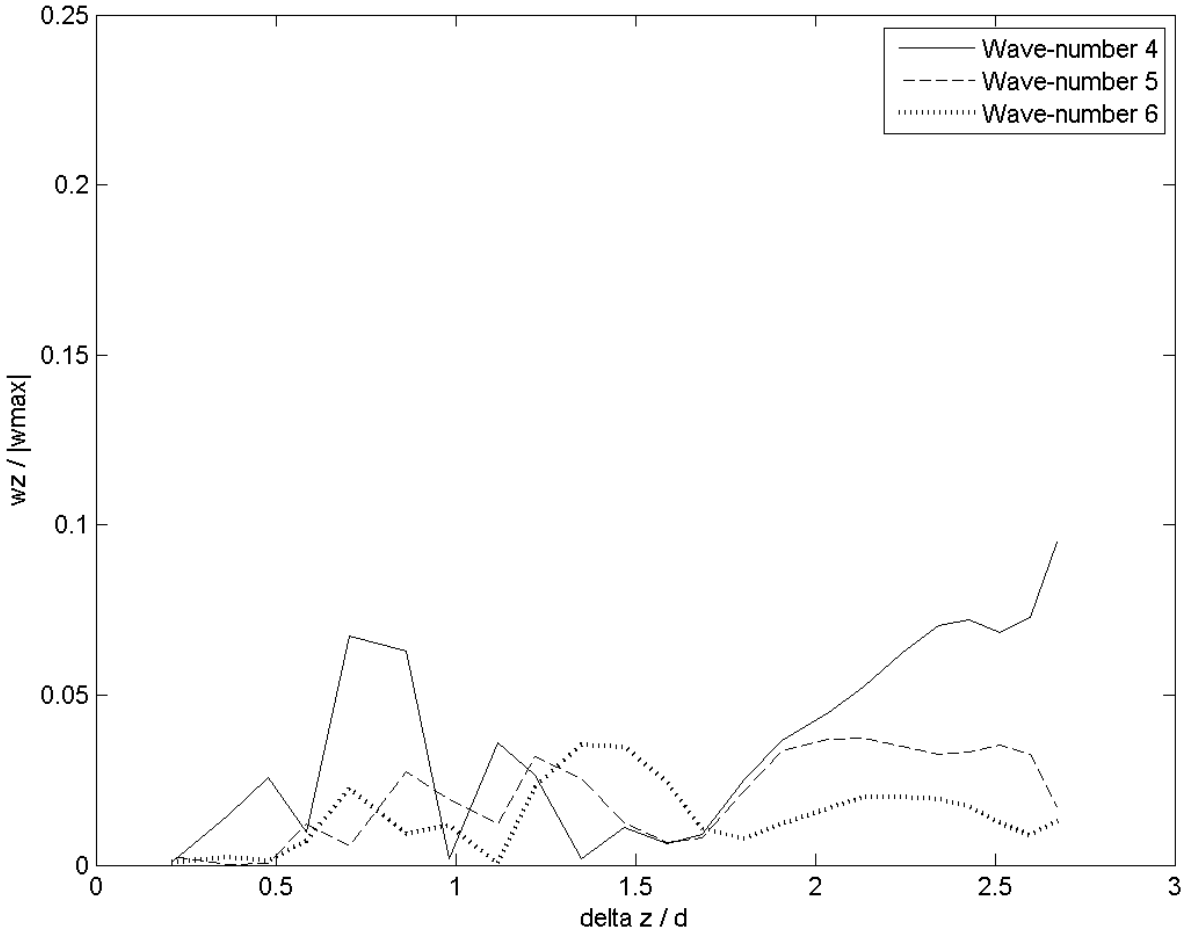

Figure 30. Instability growth of wave-numbers 4-6 for ω_z. The horizontal axis is the number of ring diameters the vortex ring has travelled. The vertical axis is the amplitude of the instability compared to the maximum vorticity magnitude around the azimuth of the vortex ring. Re = 1400, Solitary ring simulation with wave-number perturbation.

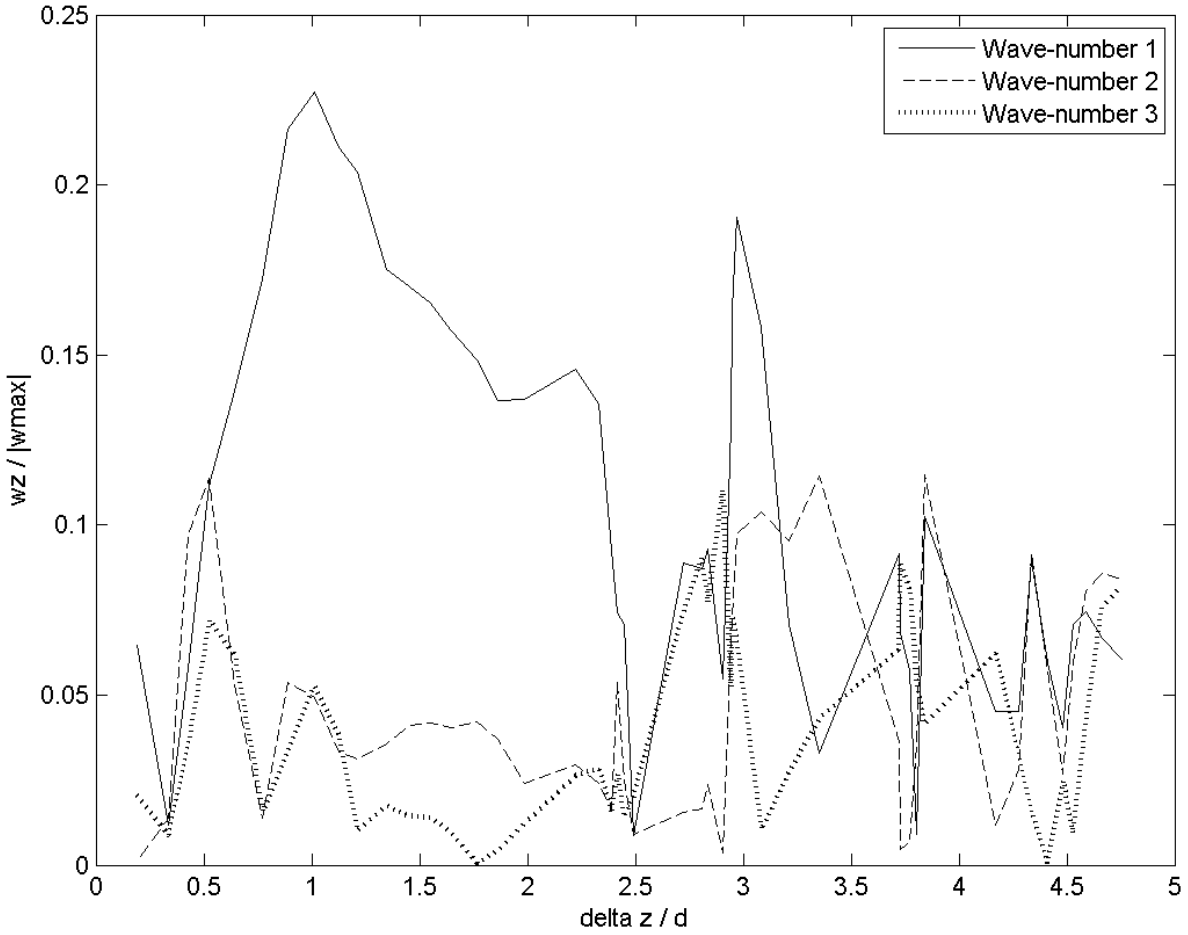

Figure 31. Instability growth of wave-numbers 1-3 for ω_z. The horizontal axis is the number of ring diameters the vortex ring has travelled. The vertical axis is the amplitude of the instability compared to the maximum vorticity magnitude around the azimuth of the vortex ring. Re = 2500, Solitary ring simulation with wave-number perturbation.

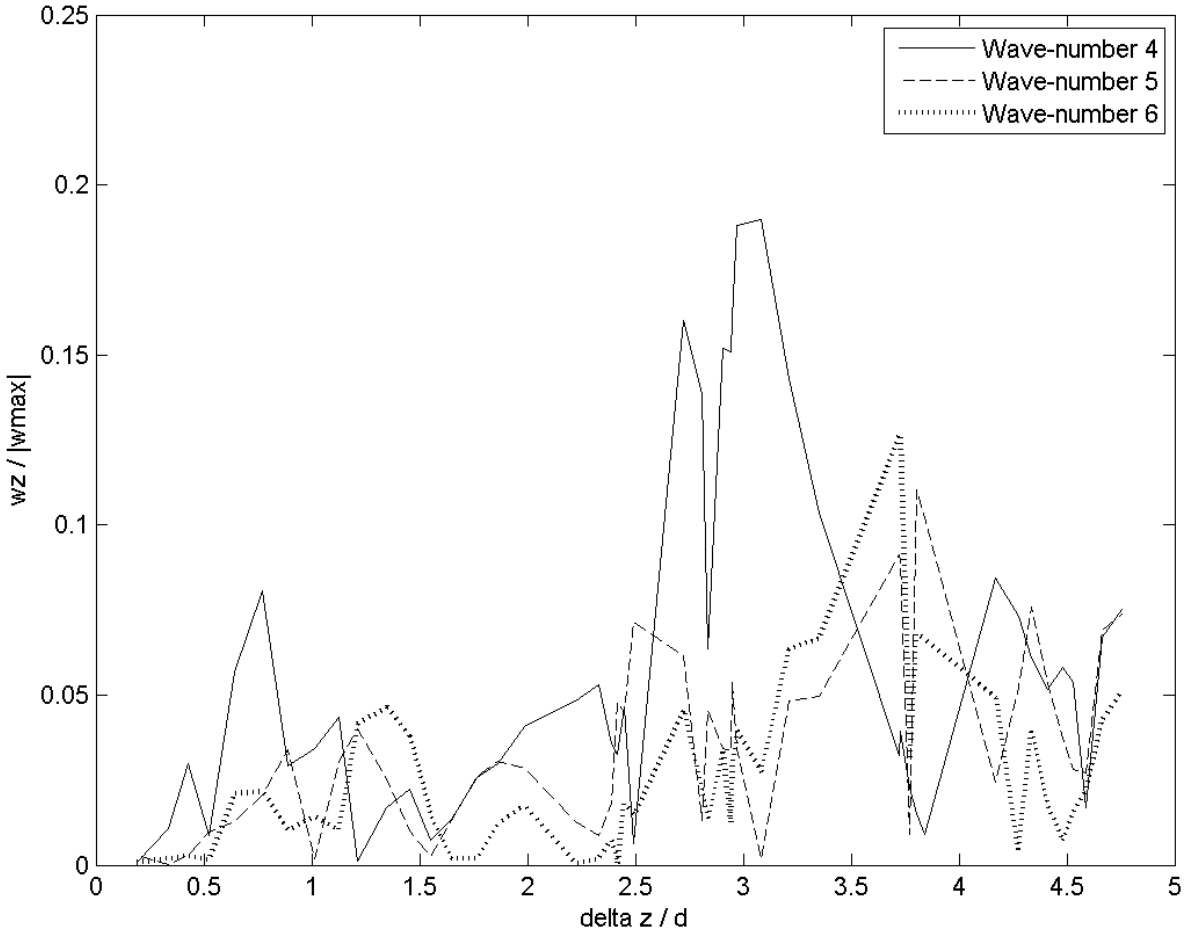

Figure 32. Instability growth of wave-numbers 4-6 for ω_z. The horizontal axis is the number of ring diameters the vortex ring has travelled. The vertical axis is the amplitude of the instability compared to the maximum vorticity magnitude around the azimuth of the vortex ring. Re = 2500, Solitary ring simulation with wave-number perturbation.

For most of the graphs, the wave-number growth is noticeably spiky. This could be due to the way the points around the core were chosen. Instead of finding the exact center of the core, which could be non-circular and therefore difficult to calculate, a circle was chosen of the initial core radius. If the actual core center was slightly away from this point, the result would be a smaller wave-number amplitude recorded at that point. This could contribute to the wave-number growth not appearing smooth.

4.6 What is the Source of the Instability?

Several types of instabilities were identified as possible causes for the instability seen in the impacting water drop experiment. Some of these were suggested in Sigurdson & Peck (1995). The Widnall instability and Rayleigh centrifugal instability were both tested as possible sources, and the Elliptic instability was later observed as a possible source.

4.6.1 Widnall Instability

The Widnall instability is one possible source of the instability observed in the impacting water drop experiment, and is discussed in Section 1.1.1.1. The Widnall instability involves the entire core of the vortex ring becoming wavy due to the straining field imposed by the circular geometry of the ring. Sigurdson & Peck (1995) wrote that they suspected the Widnall instability may not be the source of the instability, but that it may play a role at times.

To see if the Widnall instability was at work, it was tested by adding waves along the azimuth of the vortex ring to encourage the instability to grow. An instability developed from this perturbation, causing loops around the primary vortex ring. However, looking at the isosurfaces of vorticity in both the Re = 1400 and Re = 2500 cases, the vortex ring never becomes visibly wavy. The instabilities appear to develop at a few points around the ring, instead of causing the entire ring itself to become wavy which would be expected from the Widnall instability. This

suggests that the Widnall instability is likely not the source of the instability seen in the impacting water drop experiment.

4.6.2 Rayleigh Centrifugal Instability

Another possible source of the instability is the Rayleigh centrifugal instability, which is discussed in Section 1.1.1.2. The Rayleigh instability can develop whenever the circulation decreases with radial distance somewhere in the flow, which is caused by the presence of opposite-signed vorticity. It was suggested in Peck & Sigurdson (1994) that some observed opposite-signed vorticity may get trapped in the primary vortex ring, causing a situation that would be Rayleigh unstable.

The possibility of a Rayleigh instability was tested by adding a smaller secondary vortex ring of opposite sign near the primary ring, similar to what was theorized to exist in the impacting water drop experiment. The details of the geometry are shown in Figure 7 in Section 3.1.2. Tests which included only the opposite-signed ring and no other perturbation did not appear to set off an instability similar to the impacting droplet experiment. Instead, the secondary vortex ring appeared to loop around the primary ring once before being left behind in the wake. An instability was seen, however, when using the opposite-signed ring and adding waves to the azimuth of the primary vortex ring as was done in the tests for the Widnall instability.

Simulations performed with the opposite-signed ring and the wave-number perturbation produced a similar instability to that seen with a solitary ring. Bracelet structures were visible on the primary ring, and were also visible on the opposite-signed ring after it leapfrogged with the primary ring. The primary core appeared less smooth overall than simulations run without the opposite-signed ring. It is possible that the presence of the opposite-signed ring amplified the instability, but the basic appearance remained quite similar. From the isosurface images it is difficult to get a quantitative comparison of the instability size.

Since the addition of the opposite-signed vortex ring near the primary ring did not significantly change the instability seen in the simulations with a solitary ring, it suggests that a Rayleigh instability may not be the source of the instability seen in the impacting water drop experiment. The perturbation was only observed after adding waves to the azimuth of the primary ring, and appeared similar to simulations with the solitary ring. The Rayleigh instability can not be completely ruled out, however, as the opposite-signed vorticity could be added in different geometries, such as adding a sheath of opposite-signed vorticity around the primary core.

4.6.3 Vortex Breakdown

Vortex breakdown can occur when a vortex aligned with the flow moves into a slower moving region or experiences an increasing pressure gradient, for example in a diffuser, and is discussed in Panton (1996). It was observed from the images in Peck & Sigurdson (1994) that, while near the surface, the vortex ring appears to become compressed as it convects through the fluid, suggesting that a vortex breakdown instability may be present.

To cause the reduction of the vortex ring diameter in the simulations, an image vortex was placed above the main ring. Tests were run with varying distance between the main ring and the image ring to provide different amounts of contraction on the vortex ring diameter. The details of the geometry are shown in Figure 8 in Section 3.1.3. In each case, an instability was observed, however it appeared similar to the instability observed when no image vortex was present in the simulations. Similar to the tests for the Rayleigh centrifugal instability, this suggests that the instability seen in the simulations was caused by the addition of waves to perturb the vortex ring core, and not by the presence of the image vortex. It is possible, however, that the ring diameter contraction was not strong enough to cause a vortex breakdown instability.

4.6.4 Elliptic Instability

There is another instability which was not discussed when designing the initial conditions for the computational simulations presented in this thesis. It was called the elliptic instability by Leweke and Williamson (1998), where they observed two dimensional counter-rotating vortex pairs developing elliptical streamlines in the cores. In the work for this thesis, it was observed from contour plots of slices through the vortex ring core that the core sometimes developed an elliptical shape, and the two sides of the core would be displaced from each other in the z-direction. This is similar to what was seen in Leweke and Williamson (1998). The contour plots are visible in Figures 13 and 14 in Section 4.1.

Since the elliptic cores were only noticed after the simulations for this thesis were run, no simulations were run where the core was purposefully made elliptical in shape to observe the result. However, the cores appear to go elliptical on their own when the core is perturbed by adding waves along the azimuth of the vortex ring. This suggests that an elliptic instability might be at play in the impacting water drop experiment and we conclude that, of the instabilities considered, it is the most likely candidate to be the cause of the bracelet structure.

5. Conclusions

To recreate the instability seen in the impacting water droplet experiment, three different vorticity initial conditions were simulated, along with two different methods of perturbing the system. The simulated initial conditions attempted to trigger a Widnall instability, a Rayleigh centrifugal instability, and a vortex breakdown instability. The vorticity in the system was perturbed by both a random perturbation and a controlled wave perturbation of various wave-numbers but with a random phase.

Of the two methods of perturbing the vorticity, only the wave-number perturbation produced favourable results. The wave-number perturbation involved adding 30 wave-numbers of equal amplitude and random phase to the primary vortex ring. In simulations of all three initial conditions using the wave-number perturbation, an instability was seen on the vortex ring which resembled the bracelet structure of a streamwise vortex pair of rings about the core that is seen in the impacting water droplet experiment. Slight instabilities were observed in some simulations using the random perturbation, however none of the instabilities resembled the bracelet structure. Simulations that did not include a perturbation to the vorticity did not result in any visible instability. Therefore we conclude that, for the initial conditions simulated here, the wave-number perturbation is necessary to observe the bracelet structure.

An instability similar to the bracelet structure was observed in simulations of a solitary vortex ring which were performed to trigger the Widnall instability. The instability was observed in simulations run at Reynolds numbers of 1400 and 2500, based on circulation, with the instability being more pronounced at Re = 2500. A general characteristic of the Widnall instability which was not observed, however, is the waviness of the vortex ring core. While an instability resembling the bracelet structure was observed, the vortex ring core never became visibly wavy, which is characteristic of the Widnall instability. Therefore, while the solitary vortex ring simulations resulted in an instability which resembles the

bracelet structure from experiments, the Widnall instability is likely not the source.

Simulations run with a secondary opposite-signed vortex ring present to trigger a Rayleigh centrifugal instability resulted in an instability similar to that seen experimentally. However, the appearance of the instability did not seem to differ noticeably from the instability seen in simulations with a solitary vortex ring. Therefore, since adding the opposite-signed vortex ring did not change the appearance of the instability, the Rayleigh centrifugal instability is not the source. Like the simulations performed with a solitary ring, both Re = 1400 and Re = 2500 produced the instability, and the instability was more pronounced at Re = 2500.

Simulations run with an image vortex ring present to cause compression of the vortex ring and trigger a vortex breakdown instability also resulted in an instability that resembled the bracelet structure. However, while the instability was seen in simulations with the image vortex present, the instability was not noticeably different from that seen with the solitary vortex ring. This suggests that, like the Rayleigh centrifugal instability, the vortex breakdown instability is not the source of the instability since adding the image vortex ring did not change the appearance.

For the solitary ring simulations, slices through the core were taken in the radial direction and contour plots of vorticity were created. It was observed from these contour plots that the vortex ring core becomes elliptical and shifts in the streamwise direction. The elliptic shape and steamwise displacement of the core is similar to that seen by Leweke and Williamson (1998) in their examination of a two-dimensional vortex pair. Because of the similarity seen between the instability presented here and the instability seen by Leweke and Williamson (1998) we conclude that, of the instabilities examined here, the elliptic instability is the most likely source of the bracelet structure seen experimentally.

A wave-number analysis was performed on the solitary ring simulation data to determine the growth of each wave-number. For both Reynolds numbers and when examining either ω_r or ω_z, wave-number 1 is dominant. For the Re = 1400 simulations, wave-numbers beyond 3 have insignificant amplitudes. However for the Re = 2500 simulations, wave-numbers up to 18 have significant amplitudes. This is likely due to the smaller scale vorticity present in simulations with the higher Reynolds number.

To observe the evolution of the instabilities, vortex lines were observed at various time steps and locations on the vortex ring. Three vortex lines were chosen from an early time step, and they were matched up with vortex lines at later time steps to see how the instability might be evolving. Two vortex lines corresponded to a wave-number 1 instability and one of the vortex lines corresponded to a wave-number 2 instability, and they were matched up to features of the instability that are visible at later times. Observing the vortex lines shows how the instability develops at very early time steps, then gets stretched by the rotation of the vortex ring and either forms the streamwise vorticity in the wake, or wraps around the ring to form the bracelet instability from Peck & Sigurdson (1994).

5.1 Future Work

As the elliptic instability was only identified as a possible candidate for the cause of the bracelet structure after the simulations were completed, it would be valuable to perform simulations where the core was made purposely elliptical to observe the effect on the instability. Other possible initial conditions would be to use a different configuration of vorticity when simulating the Rayleigh centrifugal instability. For example, surrounding the core with a sheath of opposite-signed vorticity, such that a cross section would appear as concentric circles with the innermost circle being the primary core and the outermost circle containing the opposite-signed vorticity.

The perturbation on the vorticity in the system could also be altered. In simulations presented here the vorticity perturbation was only on the x-y plane; in future simulations the result of adding a perturbation in the z-direction could also be investigated.

It would also be useful to gather data for later time steps for some of the low Reynolds number simulations. Simulations were run to time periods chosen from the experiment of Peck & Sigurdson (1994) that were long enough to see the bracelet structure form. However, due to computer time constraints, they were not run long enough to see if the ring relaminarizes like in the experiments. Having data for later time steps might allow us to better understand what happens to the bracelet structure longer after it has formed.

Bibliography

Buchholz, J. H. J. and Sigurdson, L. W. (2000). The kinematics of the vortex ring structure generated by a bursting bubble. *Physics of Fluids*, 12(1):42-53.

Dazin, D., Dupont, P. and Stanislas, M. (2006). Experimental characterization of the instability of the vortex ring. Part I: Linear phase. *Experiments in Fluids*, 40:389-399.

Dazin, D., Dupont, P. and Stanislas, M. (2006). Experimental characterization of the instability of the vortex rings. Part II: Non-linear phase. *Experiments in Fluids*, 41:401-413.

Feng, H., Kaganovskiy, L. and Krasny, R. (2009). Azimuthal instability of a vortex ring computed by a vortex sheet panel method. *Fluid Dynamics Research*, 41:1-16.

Glezer, A. and Coles, D. (1990). An experimental study of a turbulent vortex ring. *Journal of Fluid Mechanics*, 211:243-283.

Krasny, R. and Nitsche, M. (2002). The onset of chaos in vortex sheet flow. *Journal of Fluid Mechanics*, 454:47-69.

Leweke, T. and Williamson, C. H. K. (1998). Cooperative elliptic instability of a vortex pair. *Journal of Fluid Mechanics*, 360:85-119.

Maxworthy, T. (1972). The structure and stability of vortex rings. *Journal of Fluid Mechanics*, 51(1):15-32.

Maxworthy, T. (1974). Turbulent vortex rings. *Journal of Fluid Mechanics*, 64(2):227-239.

Panton (1996). Incompressible Flow, Second Edition. New York: Wiley-Interscience.

Peck, B. and Sigurdson, L. (1994). The three-dimensional vortex structure of an impacting water drop. *Physics of Fluids*, 6(2):564-576.

Peck, B. and Sigurdson, L. (1995). The vortex ring velocity resulting from an impacting water drop. *Experiments in Fluids*, 18:351-357.

Saffman, P. G. (1978). The number of waves on unstable vortex rings. *Journal of Fluid Mechanics*, 84(4):625-639.

Shariff, K. and Leonard, A. (1992). Vortex rings. *Annual Review of Fluid*

Mechanics, 24:235-279.

Shariff, K., Verzicco, R. and Orlandi, P. (1994). A numerical study of three-dimensional vortex ring instabilities: viscous corrections and early nonlinear stage. *Journal of Fluid Mechanics*, 279:351-375.

Sigurdson, L. W. (1991). Atom-bomb / water drop. *Physics of Fluids A*, 3(9):2034.

Sigurdson, L. W. (1997). Flow visualization in turbulent large-scale structure research. *Atlas of Visualization, Vol. III*, 99-113.

Sigurdson, L. and Peck, B. (1995). Three-dimensional transition of the vorticity created by an impacting water drop. *Advances in Turbulence V*, 470-475.

Walther, J. H. and Koumoutsakos, P. (2001). Three-dimensional vortex methods for particle-laden flows with two-way coupling. *Journal of Computational Physics*, 167:39-71.

Wantanabe, Y., Saruwatari, A. and Ingram, D. M. (2008). Free-surface flows under impacting droplets. *Journal of Computational Physics*, 227:2344-2365.

Widnall, S. E. and Sullivan, J. P. (1973). On the stability of vortex rings. *Proceedings of the Royal Society of London. Series A, Mathematical and Physical Sciences*, 332(1590):335-353.

Widnall, S. E., Bliss, D. B. and Tsai, C. Y. (1974). The instability of short waves on a vortex ring. *Journal of Fluid Mechanics*, 66(1):35-47.

Widnall, S. E. and Tsai, C. Y. (1977). The instability of the thin vortex ring of constant vorticity. *Philosophical Transactions of the Royal Society of London. Series A, Mathematical and Physical Sciences*, 287(1344):273-305.

Appendix 1. Table with Details of the Simulation Parameters

Sample Image (Fig. 5)	Schematic	Kinematic Viscocity ν (cm^2/s)	Circulation Γ (cm^2/s)	Re	Type of Secondary Vorticity	Secondary Vorticity Location	Primary Ring Perturbation
a	Fig. 6	0.001	1	1000	None	N/A	None
a	Fig. 6	0.001	1	1000	None	N/A	None
a	Fig. 6	0.001	1	1000	None	N/A	None
a	Fig. 6	0.001	1	1000	None	N/A	None
b	Fig. 7	0.001	1	1000	Opposite-signed ring (15%)	s = 1.17 α	None
b	Fig. 7	0.001	1	1000	Opposite-signed ring (15%)	s = 1.17 α	None
b	Fig. 7	0.001	1	1000	Opposite-signed ring (15%)	s = 0.60 α	None
b	Fig. 7	0.001	1	1000	Opposite-signed ring (15%)	s = 0	None
b	Fig. 7	0.00001005	0.000352	35	Opposite-signed ring (15%)	s = 1.17 α	None
b	Fig. 7	0.00001005	0.000352	35	Opposite-signed ring (15%)	s = 1.17 α	None
b	Fig. 7	0.01005	3.5175	350	Opposite-signed ring (15%)	s = 1.17 α	None
b	Fig. 7	0.001	1.4	1400	Opposite-signed ring (15%)	s = 1.17 α	None
b	Fig. 7	0.001	1.4	1400	Opposite-signed ring (15%)	s = 1.17 α	None
b	Fig. 7	0.001	1.4	1400	Opposite-signed ring (15%)	s = 1.17 α	None
b	Fig. 7	0.001	1.4	1400	Opposite-signed ring (15%)	s = 1.17 α	Random, 1% of max vorticity
b	Fig. 7	0.001	1.4	1400	Opposite-signed ring (15%)	s = 1.17 α	Random, 2% of max vorticity
c	Fig. 7	0.001	1.4	1400	Opposite-signed ring (30%)	s = 0.94 α	Random, 10% of local vorticity
c	Fig. 7	0.01	14	1400	Opposite-signed ring (30%)	s = 0.94 α	Random, 10% of local vorticity
c	Fig. 7	0.01	14	1400	Opposite-signed ring (30%)	s = 0.94 α	Random, 10% of local vorticity

Table A1. Details of the parameters used in the simulations. Sample images are given in Figure 3 in the body of the thesis.

Sample Image (Fig. 5)	Schematic	Kinematic Viscocity ν (cm^2/s)	Circulation Γ (cm^2/s)	Re	Type of Secondary Vorticity	Secondary Vorticity Location	Primary Ring Perturbation
c	Fig. 7	0.01	14	1400	Opposite-signed ring (30%)	s = 0.67 α	Random, 10% of local vorticity
N/A	Fig. 7	0.01	14	1400	Opposite-signed ring (30%)	s = 0.67 α	1 wave, 38% r_p amplitude
d	Fig. 7	0.01	14	1400	Opposite-signed ring (30%)	s = 0.67 α	30 waves, 0.33% r_p amplitude
d	Fig. 7	0.01	14	1400	Opposite-signed ring (30%)	s = 0.67 α	30 waves, 10% r_p amplitude
d	Fig. 7	0.01	14	1400	Opposite-signed ring (30%)	s = 0.67 α	30 waves, 1% r_p amplitude
e	Fig. 7	0.01	25	2500	Opposite-signed ring (30%)	s = 0.67 α	30 waves, 1% r_p amplitude
e	Fig. 7	0.01	25	2500	Opposite-signed ring (30%)	s = 0.67 α	30 waves, 1% r_p amplitude
f	Fig. 6	0.01	14	1400	None	N/A	30 waves, 0.33% r amplitude
f	Fig. 6	0.01	14	1400	None	N/A	30 waves, 1% r amplitude
f	Fig. 6	0.01	14	1400	None	N/A	30 waves, 1% r amplitude
f	Fig. 6	0.01	14	1400	None	N/A	30 waves, 1% r amplitude
N/A	Fig. 6	0.01	14	1400	None	N/A	Random, 5% of max vorticity
N/A	Fig. 6	0.01	14	1400	None	N/A	Random, 5% of max vorticity
g	Fig. 6	0.01	25	2500	None	N/A	30 waves, 1% r amplitude
g	Fig. 6	0.01	25	2500	None	N/A	30 waves, 1% r amplitude
g	Fig. 6	0.01	25	2500	None	N/A	30 waves, 1% r amplitude
h	Fig. 8	0.01	14	1400	Image vortex	h = 2 α	30 waves, 1% r_p amplitude
h	Fig. 8	0.01	14	1400	Image vortex	h = 4 α	30 waves, 1% r_p amplitude
h	Fig. 8	0.01	14	1400	Image vortex	h = 2 α	30 waves, 1% r_p amplitude
h	Fig. 8	0.01	14	1400	Image vortex	h = 1 α	30 waves, 1% r_p amplitude

Table A1, Continued. Details of the parameters used in the simulations. Sample images are given in Figure 3 in the body of the thesis.

Appendix 2. Isosurfaces for Solitary Ring Simulation, Re = 1400

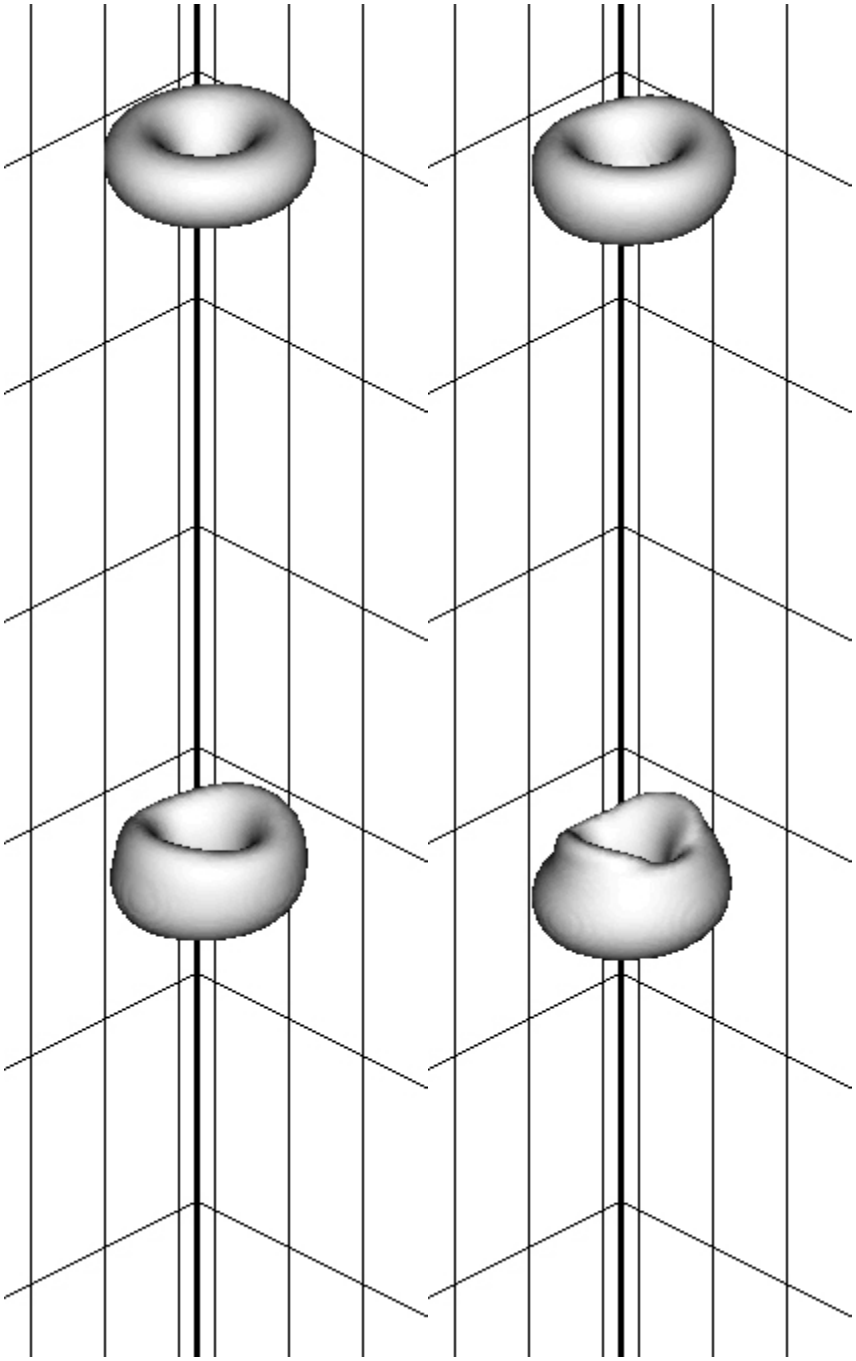

Figure A1. Isosurfaces of total vorticity magnitude for the solitary ring simulations at Re = 1400. Isosurface is taken at a vorticity level of $\omega = 250\ s^{-1}$. Images correspond to times of 0.002s, 0.004s, 0.006s, 0.008s. Images should be viewed in the order: top left, top right, bottom left, bottom right.

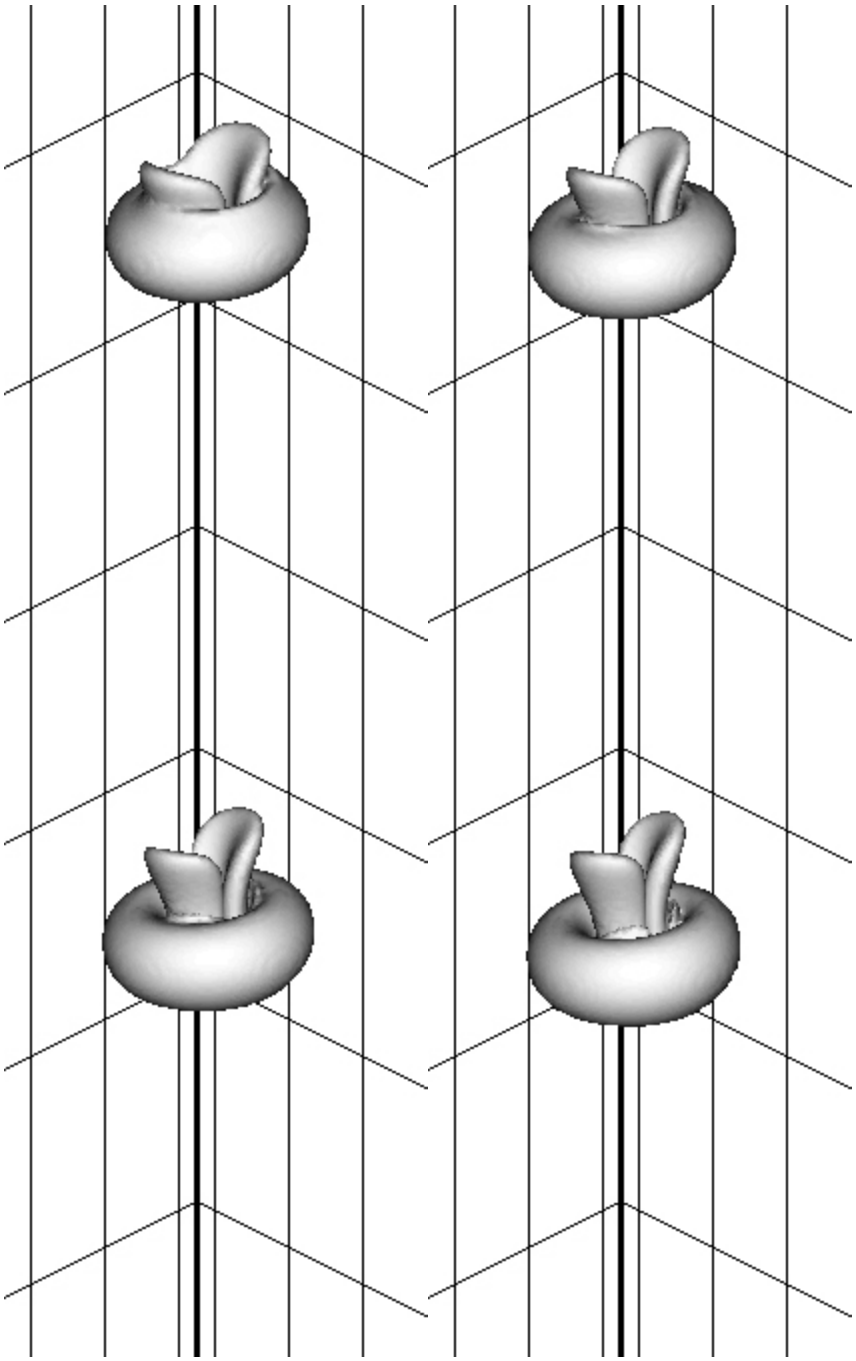

Figure A1, Continued. Isosurfaces of total vorticity magnitude for the solitary ring simulations at Re = 1400. Isosurface is taken at a vorticity level of $\omega = 250\ s^{-1}$. Images correspond to times of 0.010s, 0.012s, 0.014s, 0.016s. Images should be viewed in the order: top left, top right, bottom left, bottom right.

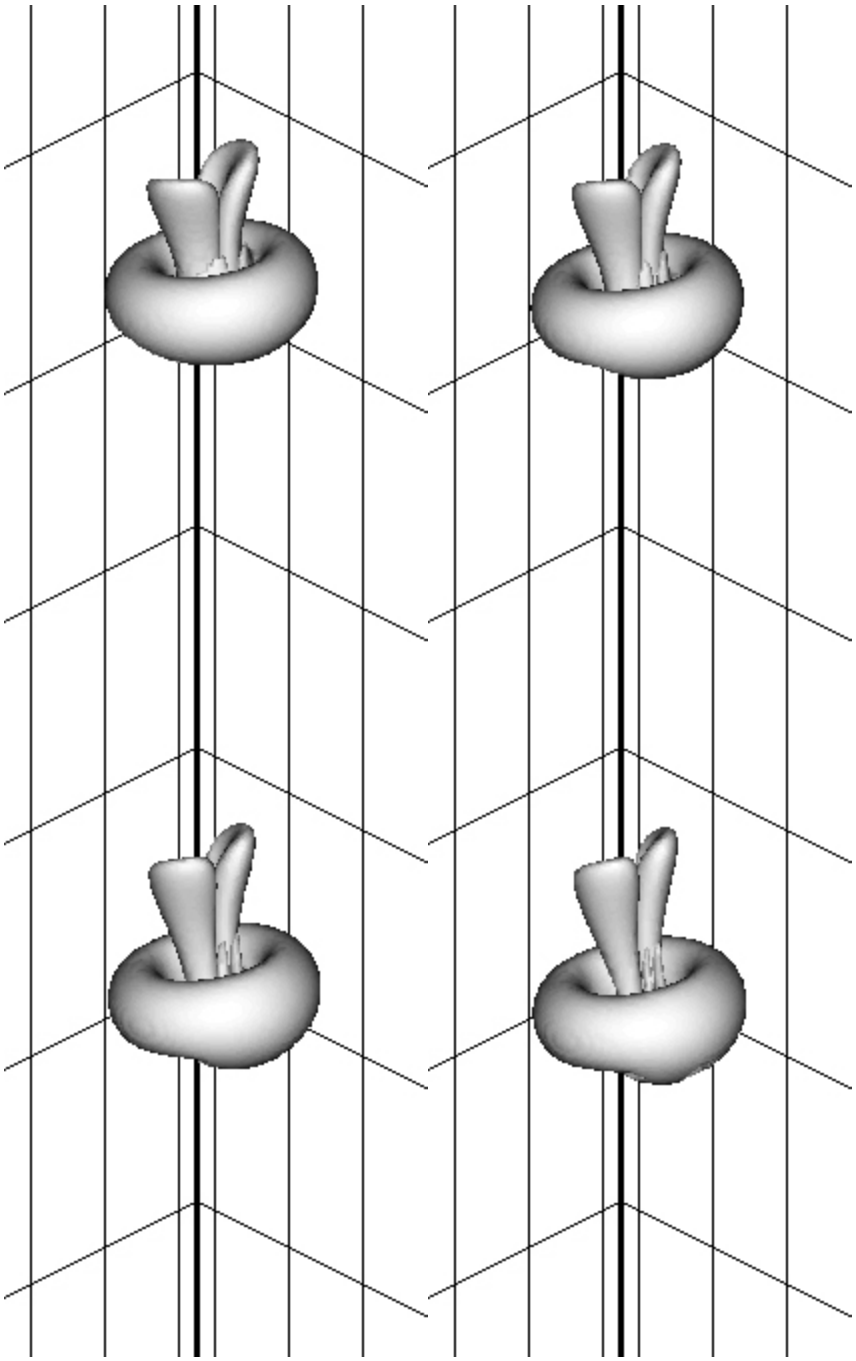

Figure A1, Continued. Isosurfaces of total vorticity magnitude for the solitary ring simulations at Re = 1400. Isosurface is taken at a vorticity level of $\omega = 250\ s^{-1}$. Images correspond to times of 0.018s, 0.020s, 0.022s, 0.024s. Images should be viewed in the order: top left, top right, bottom left, bottom right.

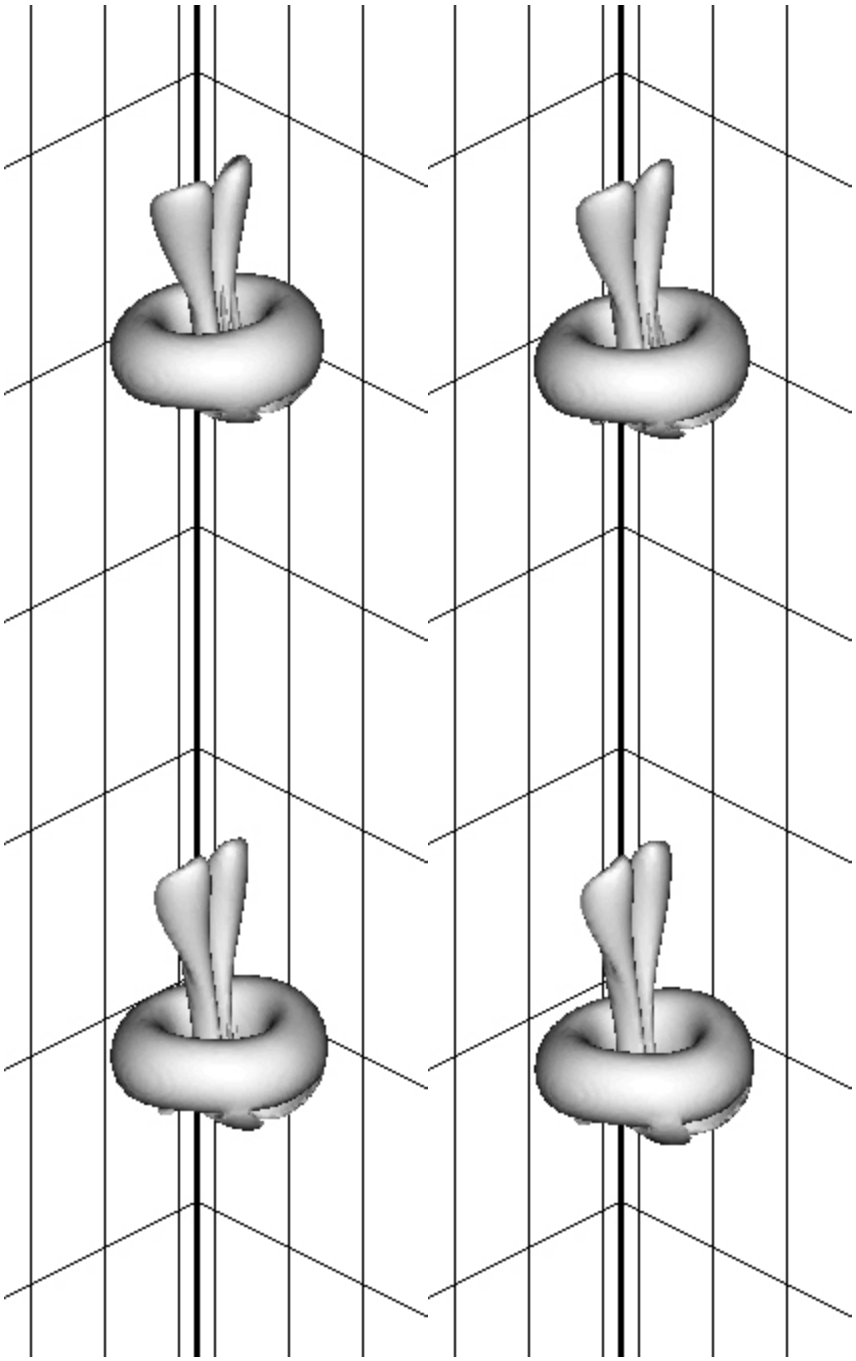

Figure A1, Continued. Isosurfaces of total vorticity magnitude for the solitary ring simulations at Re = 1400. Isosurface is taken at a vorticity level of $\omega = 250\ s^{-1}$. Images correspond to times of 0.026s, 0.028s, 0.030s, 0.032s. Images should be viewed in the order: top left, top right, bottom left, bottom right.

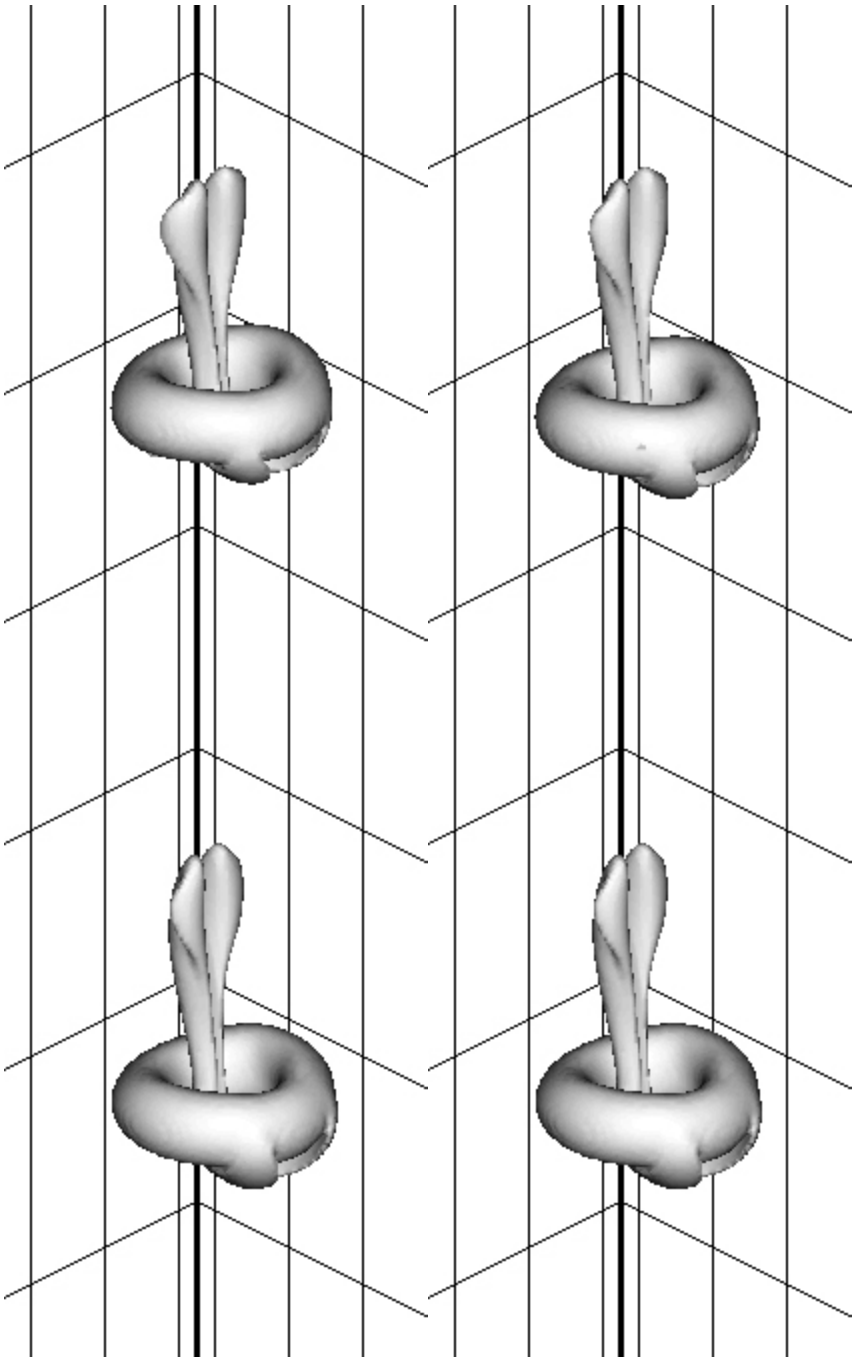

Figure A1, Continued. Isosurfaces of total vorticity magnitude for the solitary ring simulations at Re = 1400. Isosurface is taken at a vorticity level of $\omega = 250\ s^{-1}$. Images correspond to times of 0.034s, 0.036s, 0.038s, 0.040s. Images should be viewed in the order: top left, top right, bottom left, bottom right.

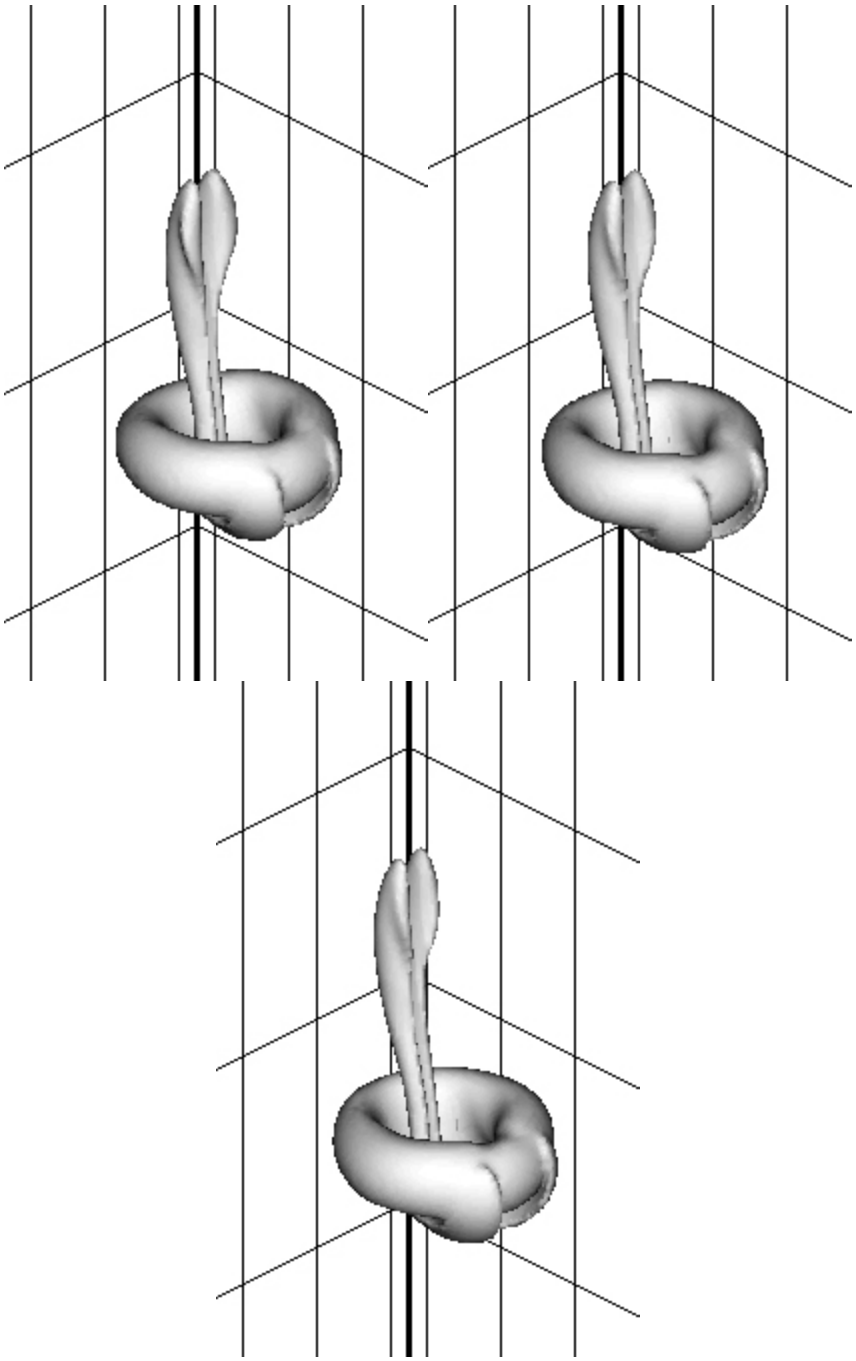

Figure A1, Continued. Isosurfaces of total vorticity magnitude for the solitary ring simulations at Re = 1400. Isosurface is taken at a vorticity level of $\omega = 250\ s^{-1}$. Images correspond to times of 0.042s, 0.044s, 0.046s. Images should be viewed in the order: top left, top right, bottom.

Appendix 3. Isosurfaces for Solitary Ring Simulation, Re = 2500

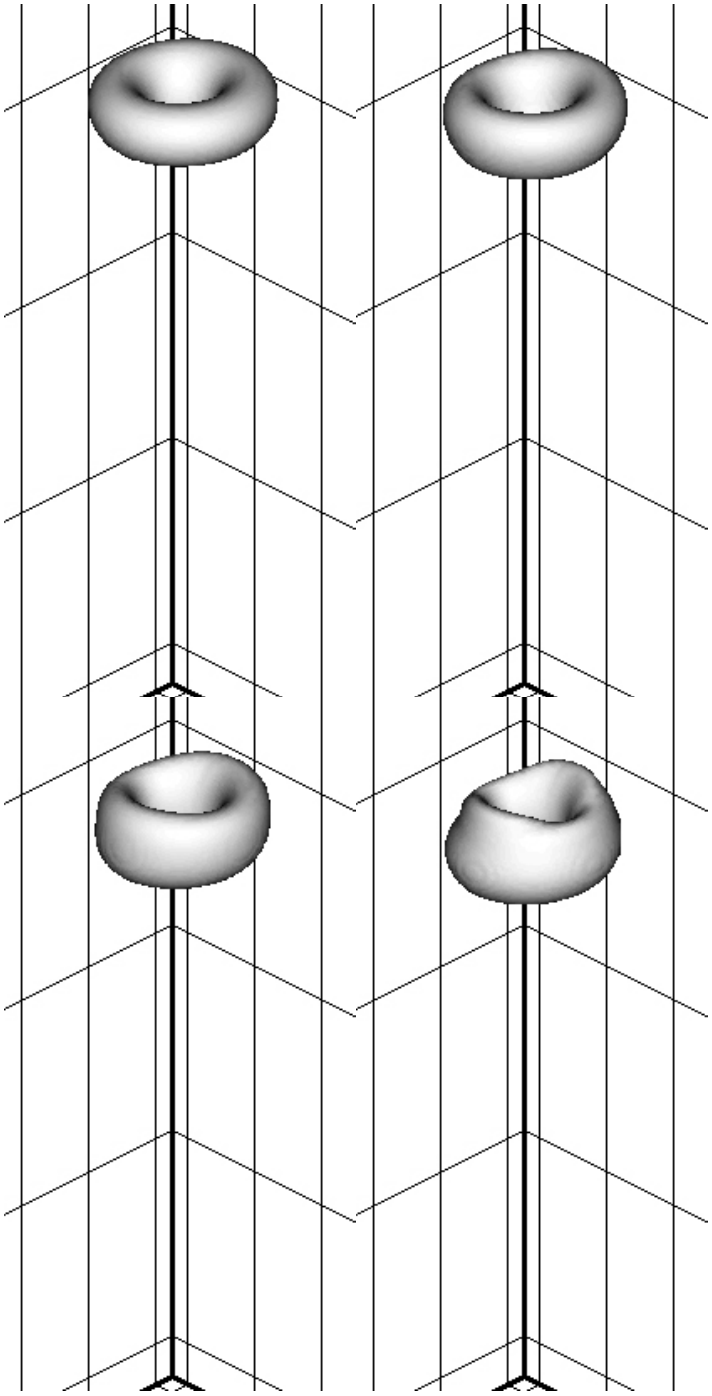

Figure A2. Isosurfaces of total vorticity magnitude for the solitary ring simulations at Re = 2500. Isosurface is taken at a vorticity level of $\omega = 250\ s^{-1}$. Images correspond to times of 0.001s, 0.002s, 0.003s, 0.004s. Images should be viewed in the order: top left, top right, bottom left, bottom right.

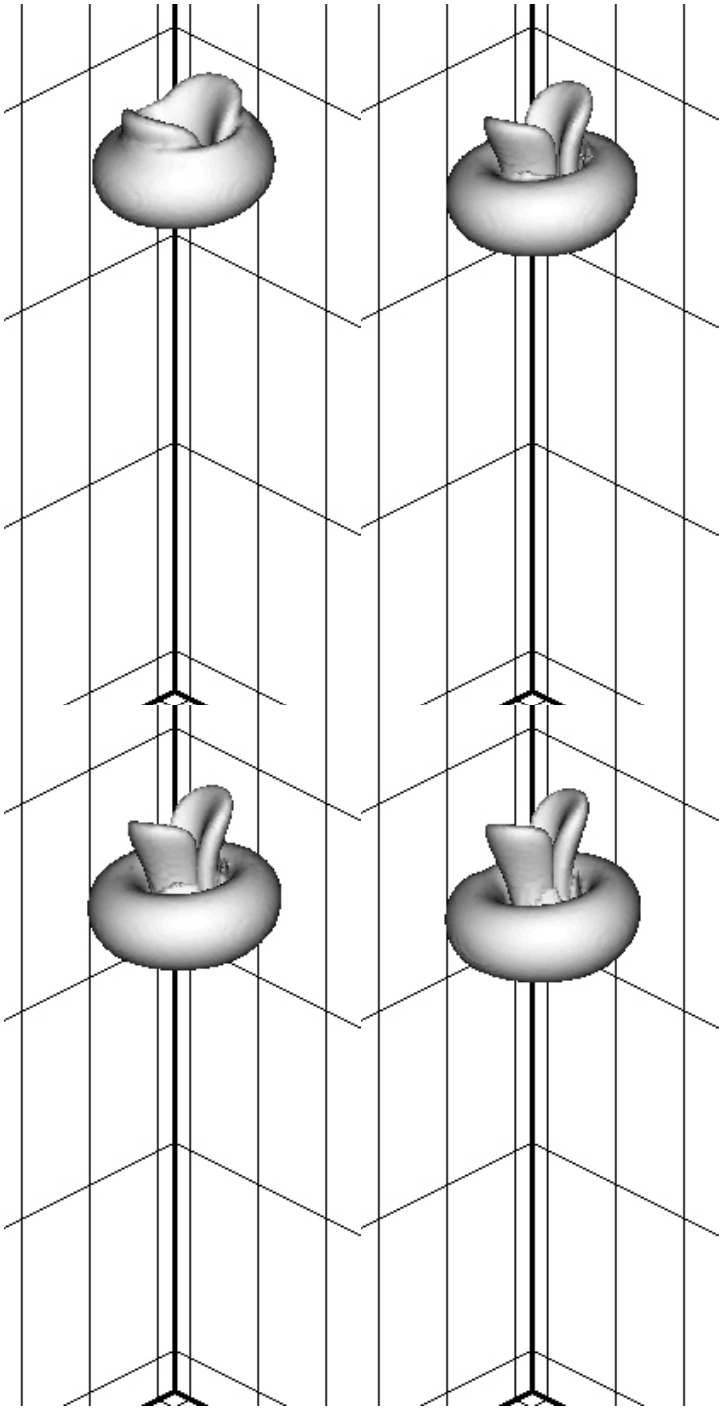

Figure A2, Continued. Isosurfaces of total vorticity magnitude for the solitary ring simulations at Re = 2500. Isosurface is taken at a vorticity level of $\omega = 250\ s^{-1}$. Images correspond to times of 0.005s, 0.006s, 0.007s, 0.008s. Images should be viewed in the order: top left, top right, bottom left, bottom right.

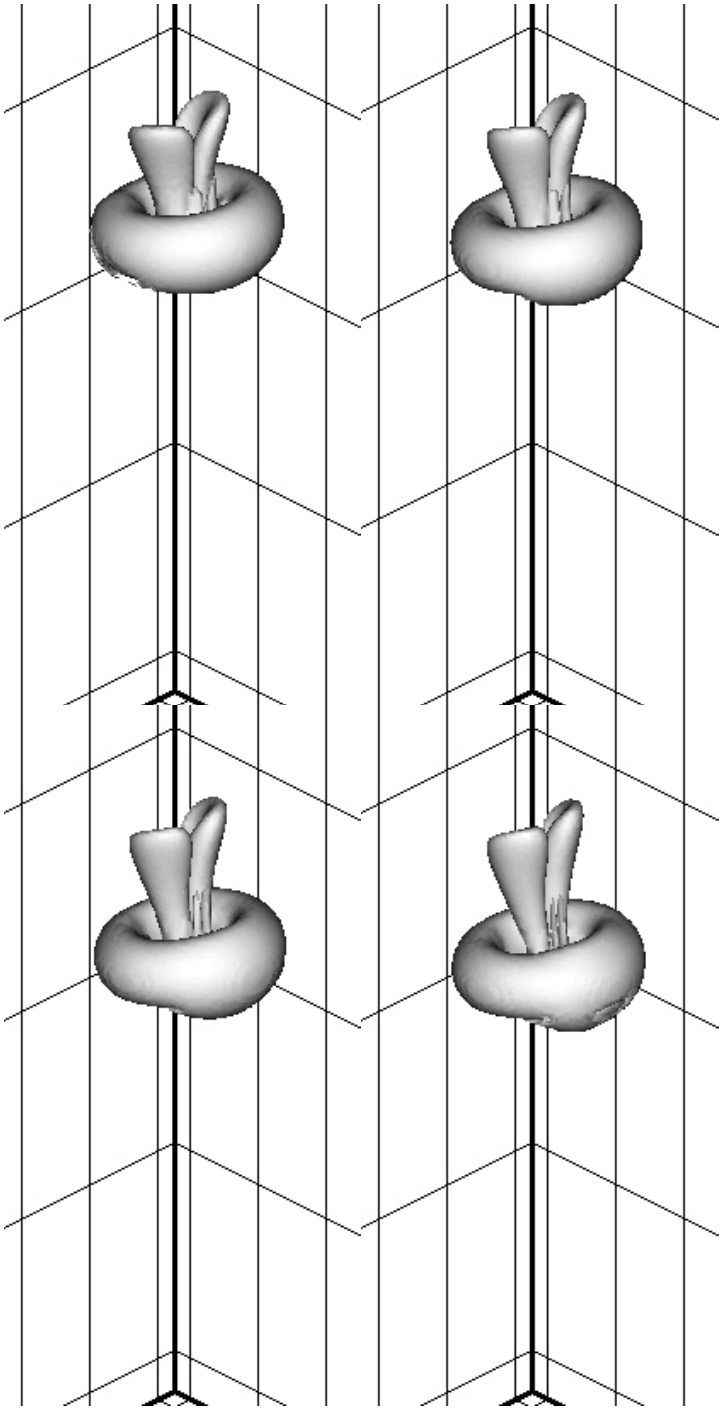

Figure A2, Continued. Isosurfaces of total vorticity magnitude for the solitary ring simulations at Re = 2500. Isosurface is taken at a vorticity level of $\omega = 250\ s^{-1}$. Images correspond to times of 0.009s, 0.010s, 0.011s, 0.012s. Images should be viewed in the order: top left, top right, bottom left, bottom right.

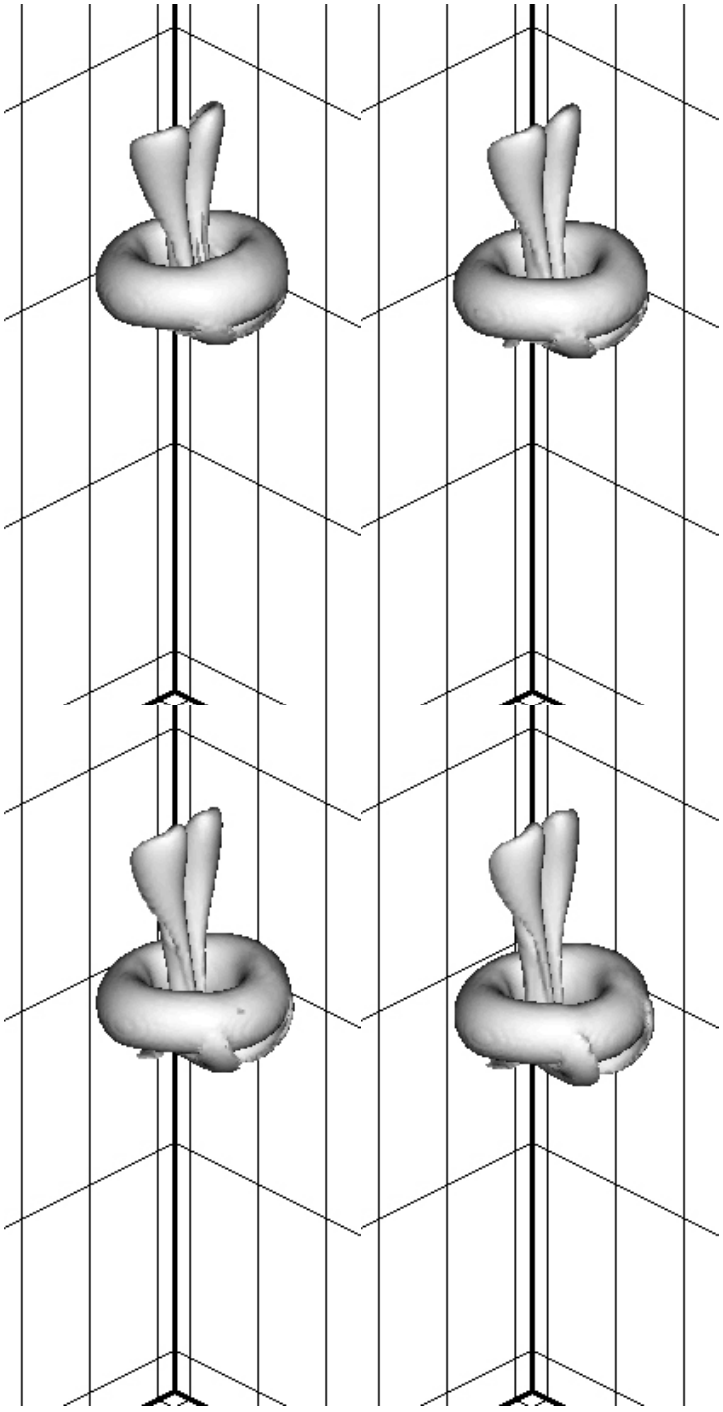

Figure A2, Continued. Isosurfaces of total vorticity magnitude for the solitary ring simulations at Re = 2500. Isosurface is taken at a vorticity level of $\omega = 250\ s^{-1}$. Images correspond to times of 0.013s, 0.014s, 0.015s, 0.016s. Images should be viewed in the order: top left, top right, bottom left, bottom right.

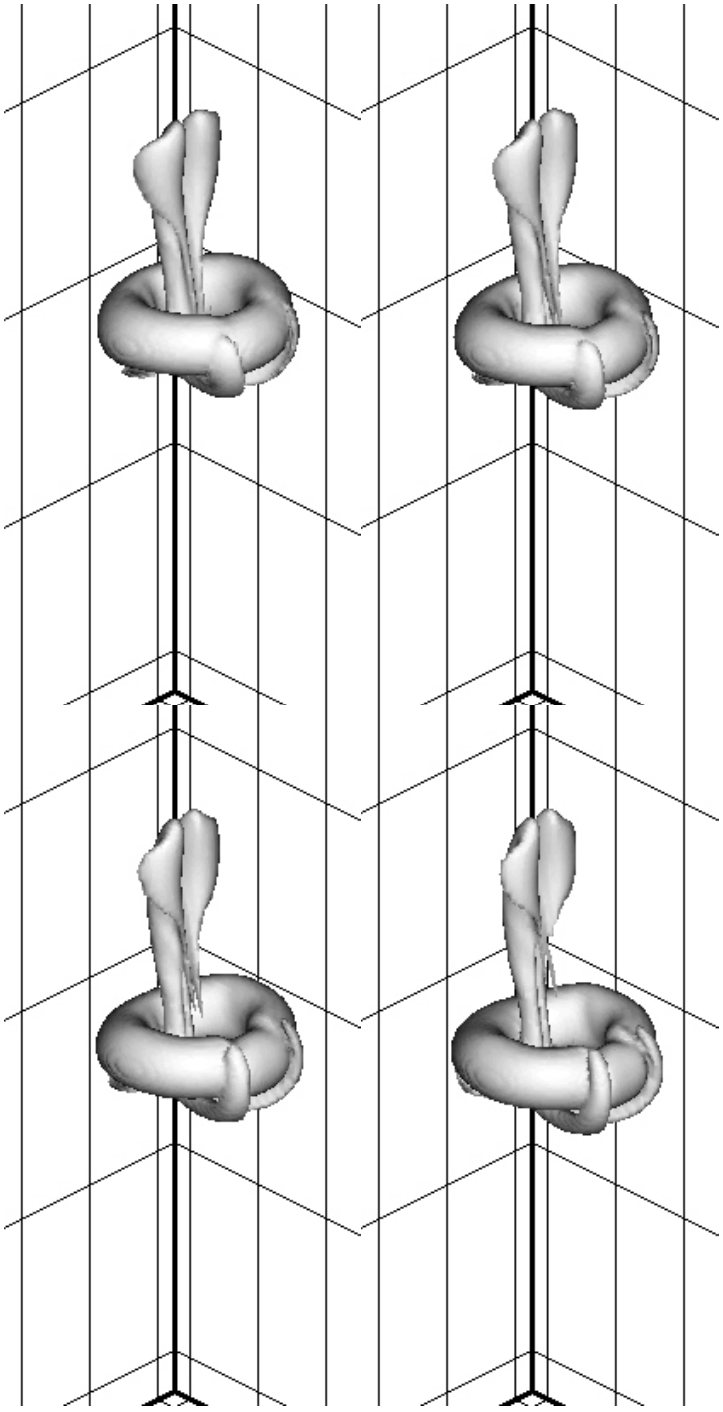

Figure A2, Continued. Isosurfaces of total vorticity magnitude for the solitary ring simulations at Re = 2500. Isosurface is taken at a vorticity level of $\omega = 250\ s^{-1}$. Images correspond to times of 0.017s, 0.018s, 0.019s, 0.020s. Images should be viewed in the order: top left, top right, bottom left, bottom right.

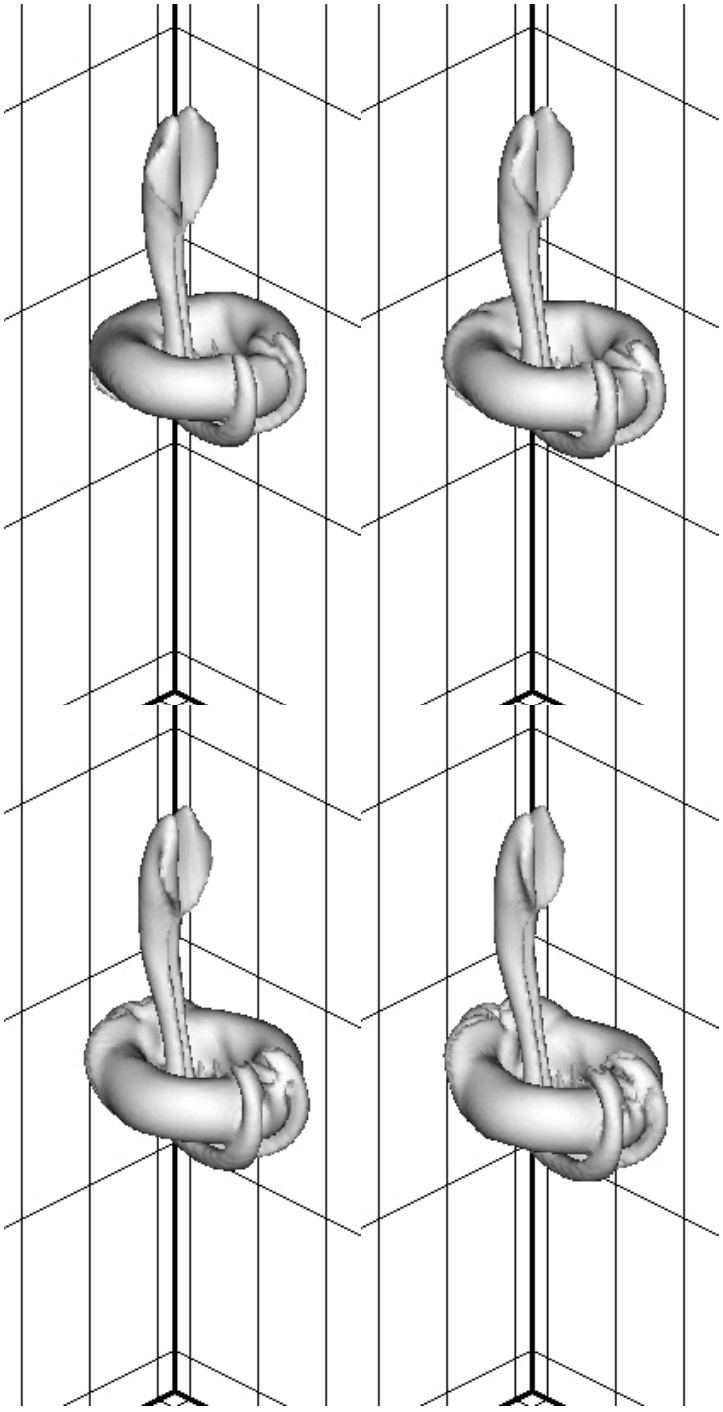

Figure A2, Continued. Isosurfaces of total vorticity magnitude for the solitary ring simulations at Re = 2500. Isosurface is taken at a vorticity level of $\omega = 250\ s^{-1}$. Images correspond to times of 0.021s, 0.022s, 0.023s, 0.024s. Images should be viewed in the order: top left, top right, bottom left, bottom right.

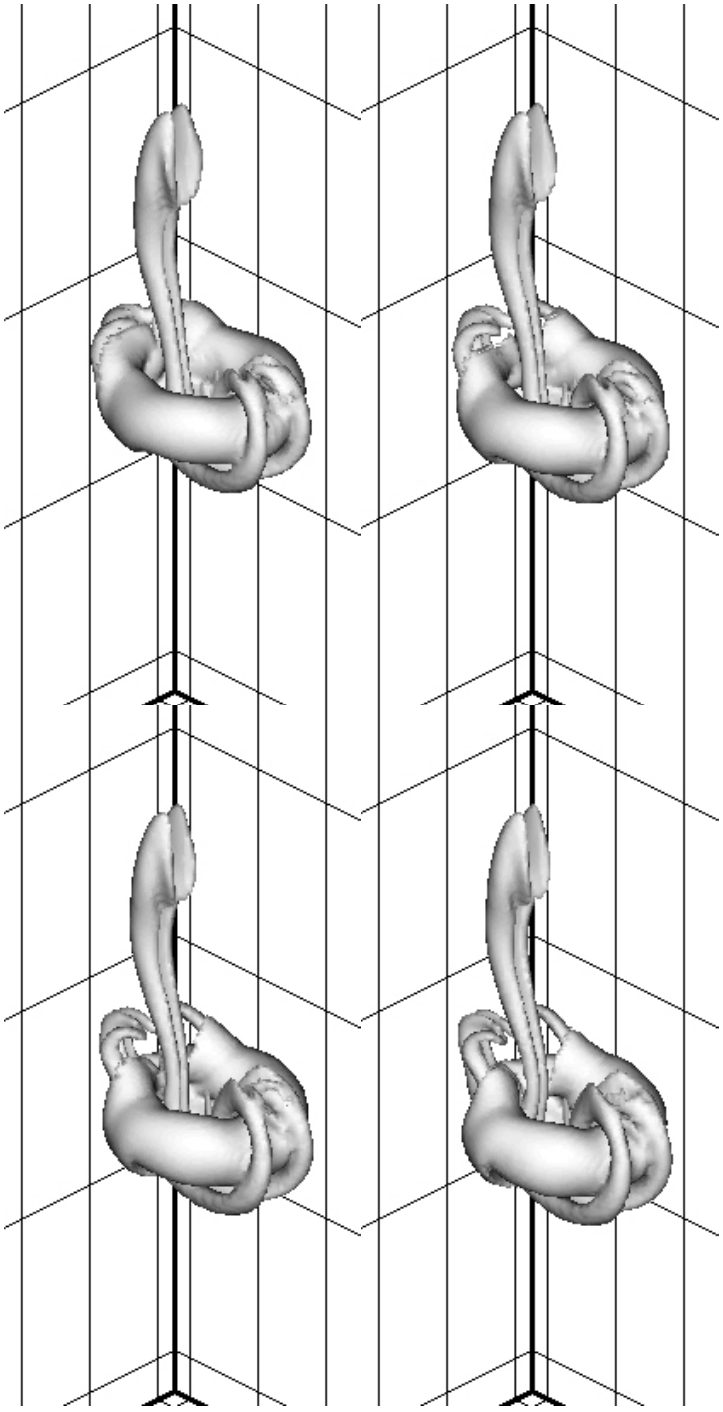

Figure A2, Continued. Isosurfaces of total vorticity magnitude for the solitary ring simulations at Re = 2500. Isosurface is taken at a vorticity level of $\omega = 250\ s^{-1}$. Images correspond to times of 0.025s, 0.026s, 0.027s, 0.028s. Images should be viewed in the order: top left, top right, bottom left, bottom right.

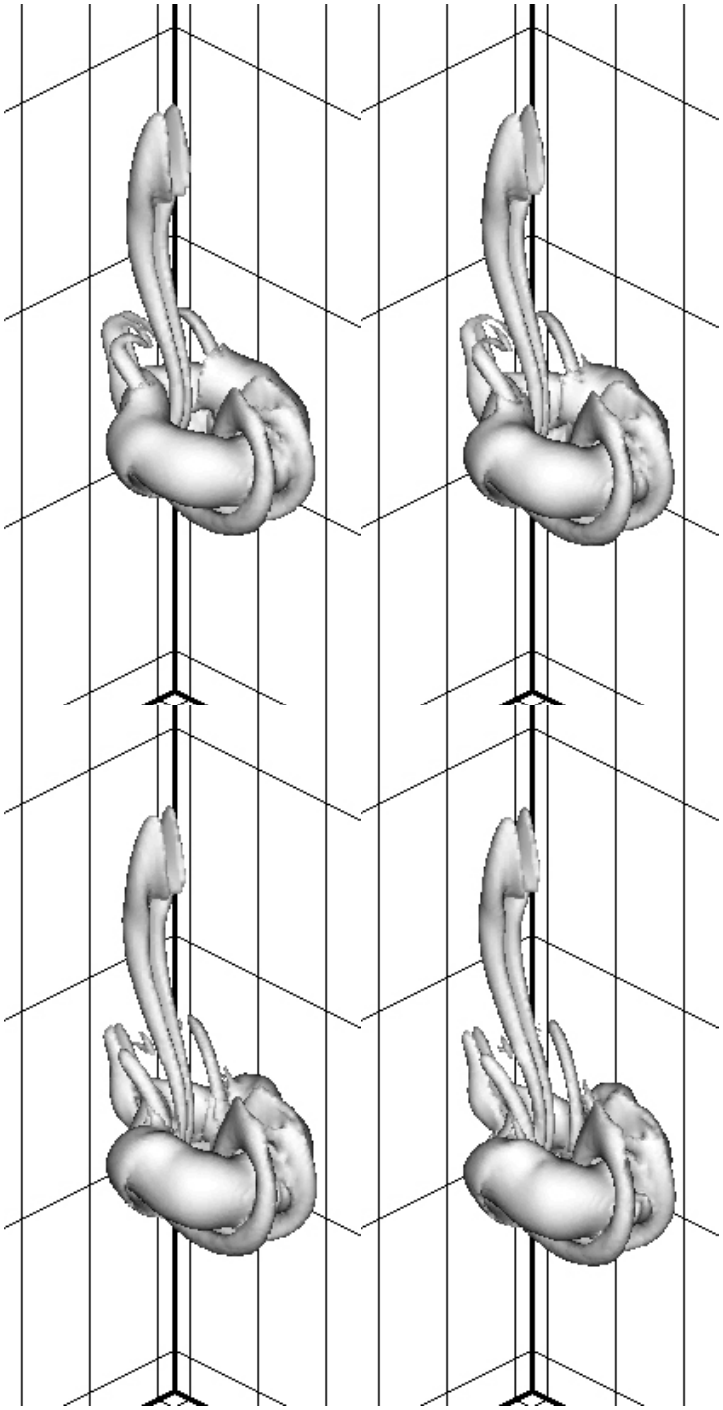

Figure A2, Continued. Isosurfaces of total vorticity magnitude for the solitary ring simulations at Re = 2500. Isosurface is taken at a vorticity level of $\omega = 250\ s^{-1}$. Images correspond to times of 0.029s, 0.030s, 0.031s, 0.032s. Images should be viewed in the order: top left, top right, bottom left, bottom right.

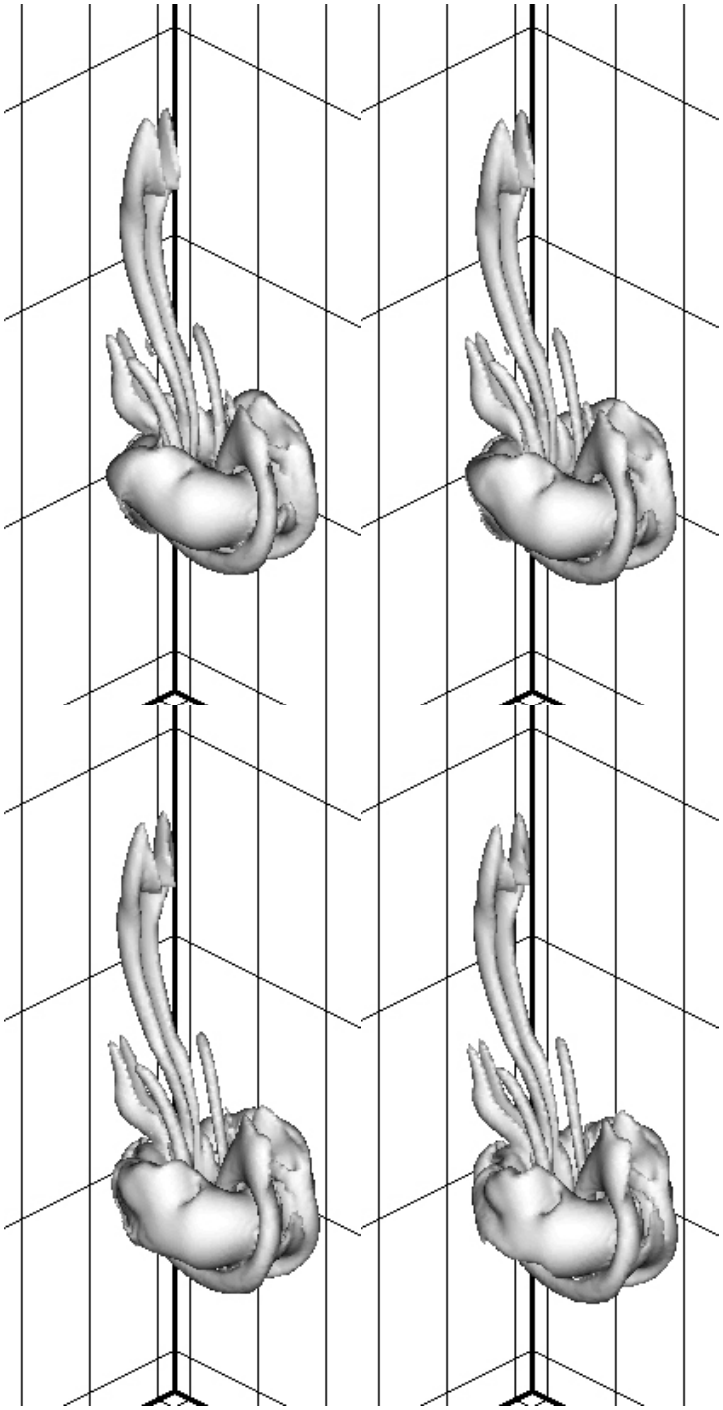

Figure A2, Continued. Isosurfaces of total vorticity magnitude for the solitary ring simulations at Re = 2500. Isosurface is taken at a vorticity level of $\omega = 250\ s^{-1}$. Images correspond to times of 0.033s, 0.034s, 0.035s, 0.036s. Images should be viewed in the order: top left, top right, bottom left, bottom right.

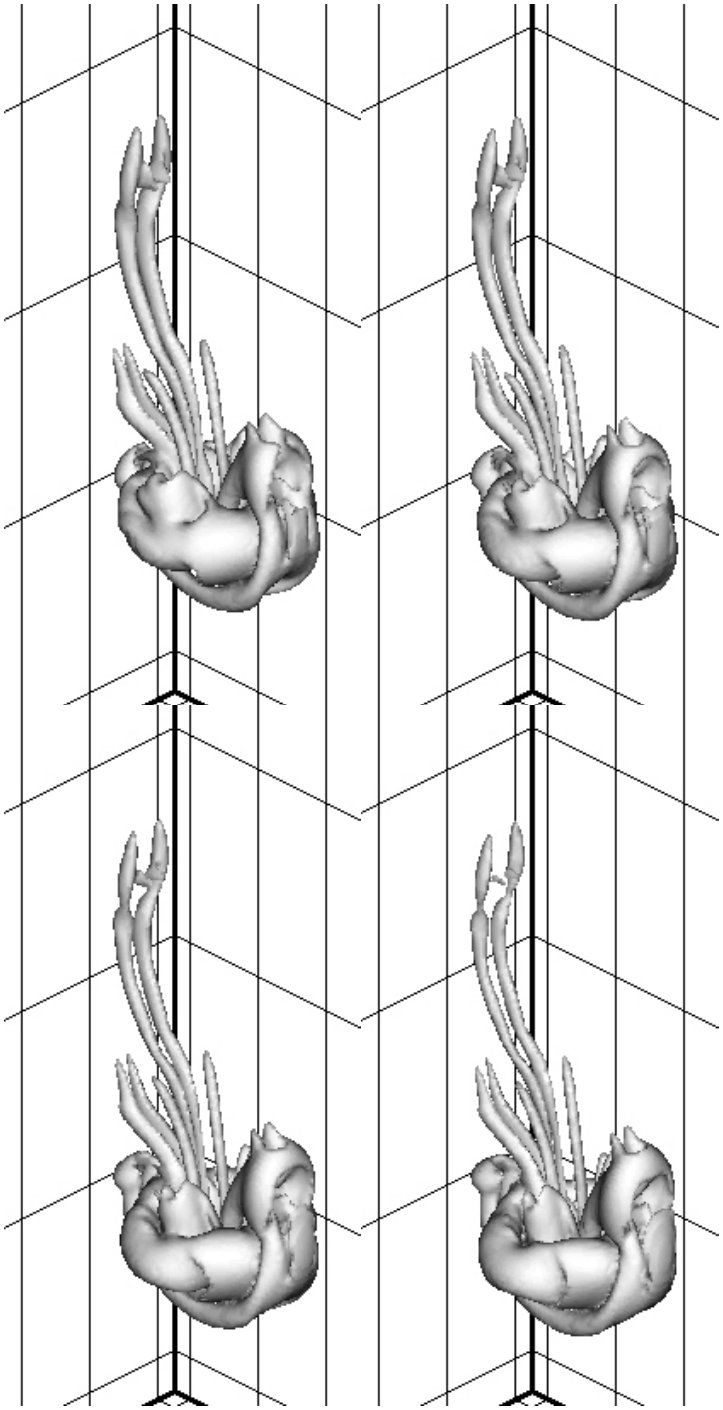

Figure A2, Continued. Isosurfaces of total vorticity magnitude for the solitary ring simulations at Re = 2500. Isosurface is taken at a vorticity level of $\omega = 250\ s^{-1}$. Images correspond to times of 0.037s, 0.038s, 0.039s, 0.040s. Images should be viewed in the order: top left, top right, bottom left, bottom right.

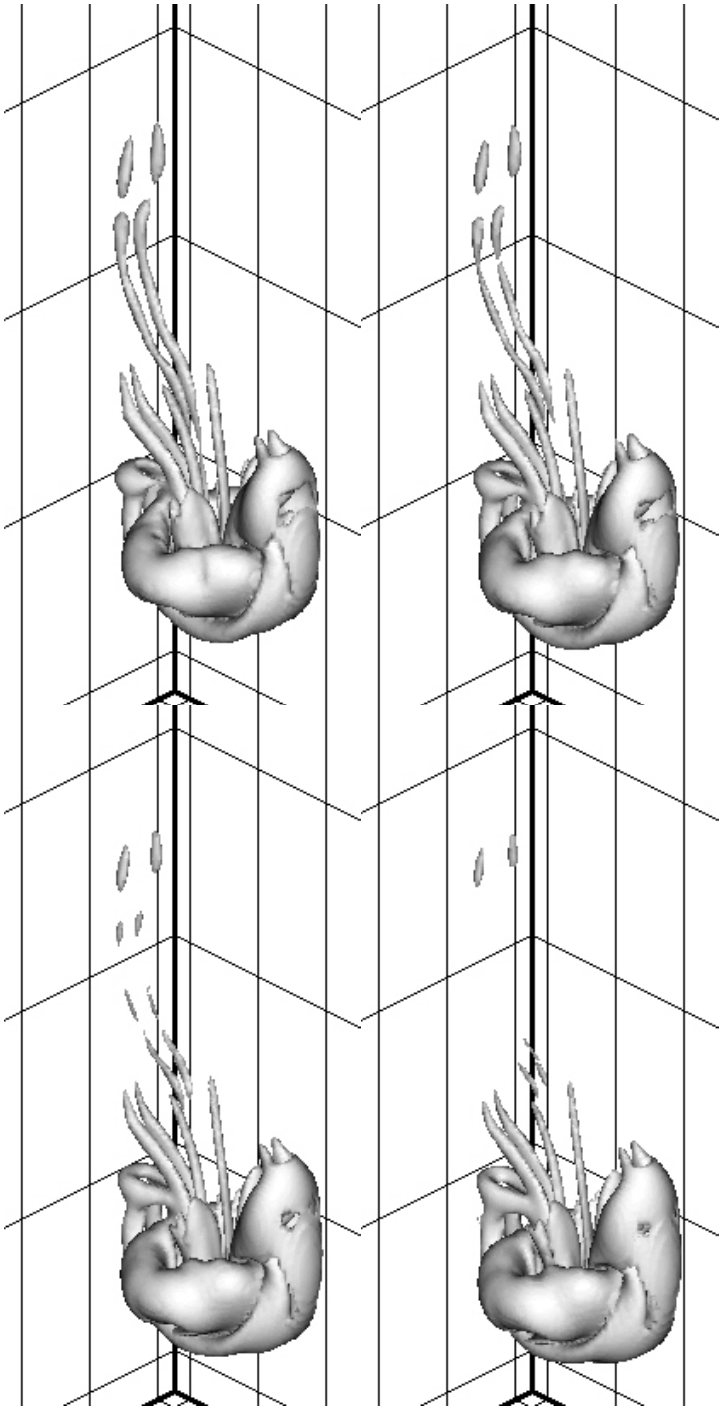

Figure A2, Continued. Isosurfaces of total vorticity magnitude for the solitary ring simulations at Re = 2500. Isosurface is taken at a vorticity level of $\omega = 250\ s^{-1}$. Images correspond to times of 0.041s, 0.042s, 0.043s, 0.044s. Images should be viewed in the order: top left, top right, bottom left, bottom right.

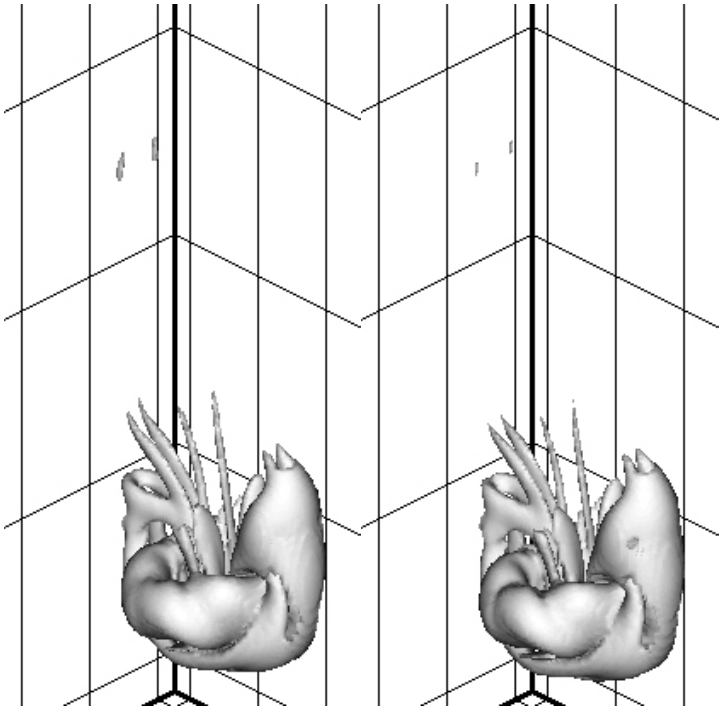

Figure A2, Continued. Isosurfaces of total vorticity magnitude for the solitary ring simulations at Re = 2500. Isosurface is taken at a vorticity level of $\omega = 250\ s^{-1}$. Images correspond to times of 0.045s, 0.046s. Images should be viewed left to right.

Appendix 4. Contour Plots for Solitary Ring Simulations. Re = 1400

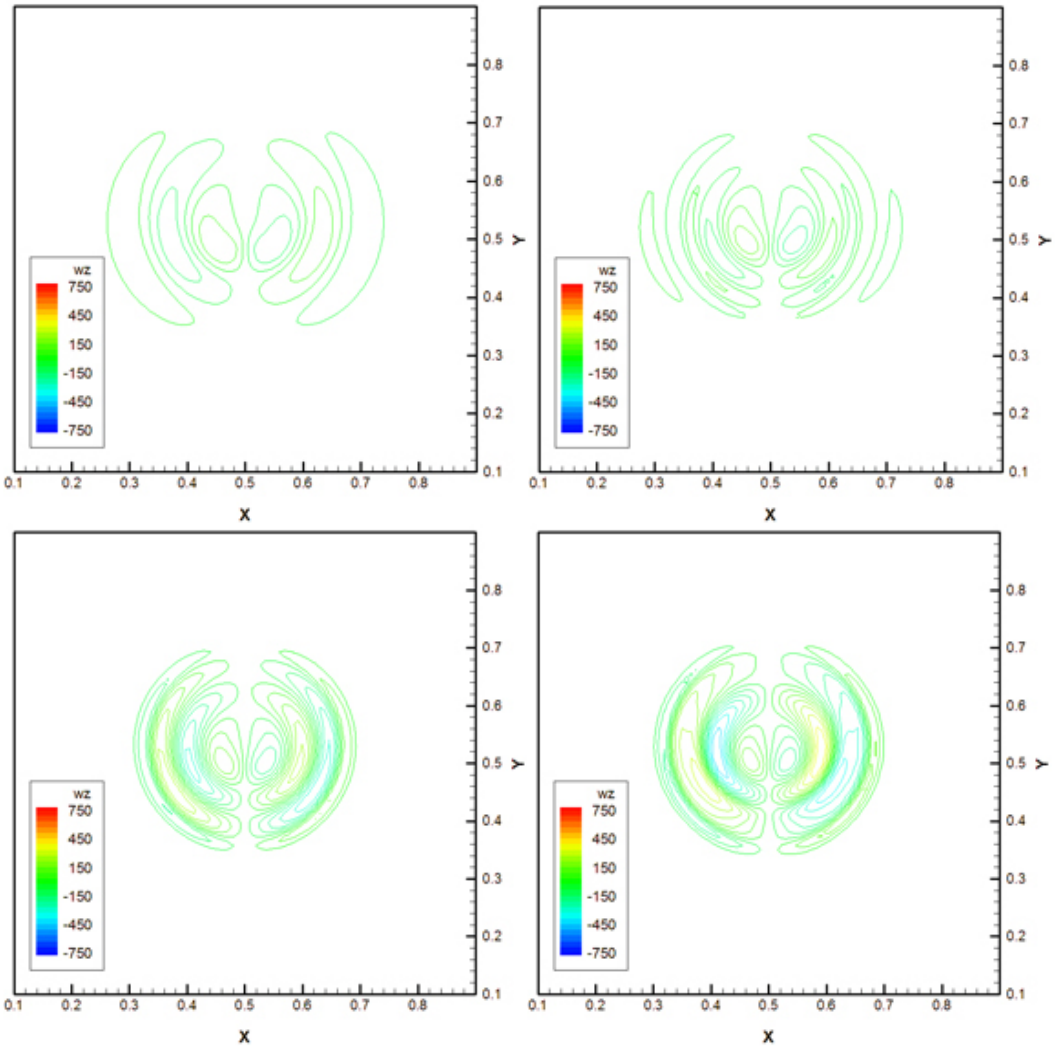

Figure A3. Contour plots in an x-y plane for the solitary ring simulations at Re = 1400. The x-y plane is taken through the centroid of the x and y vorticity, which approximates the center of the vortex ring core. Images correspond to times of 0.002s, 0.004s, 0.006s, 0.008s, and should be viewed in the order: top left, top right, bottom left, bottom right.

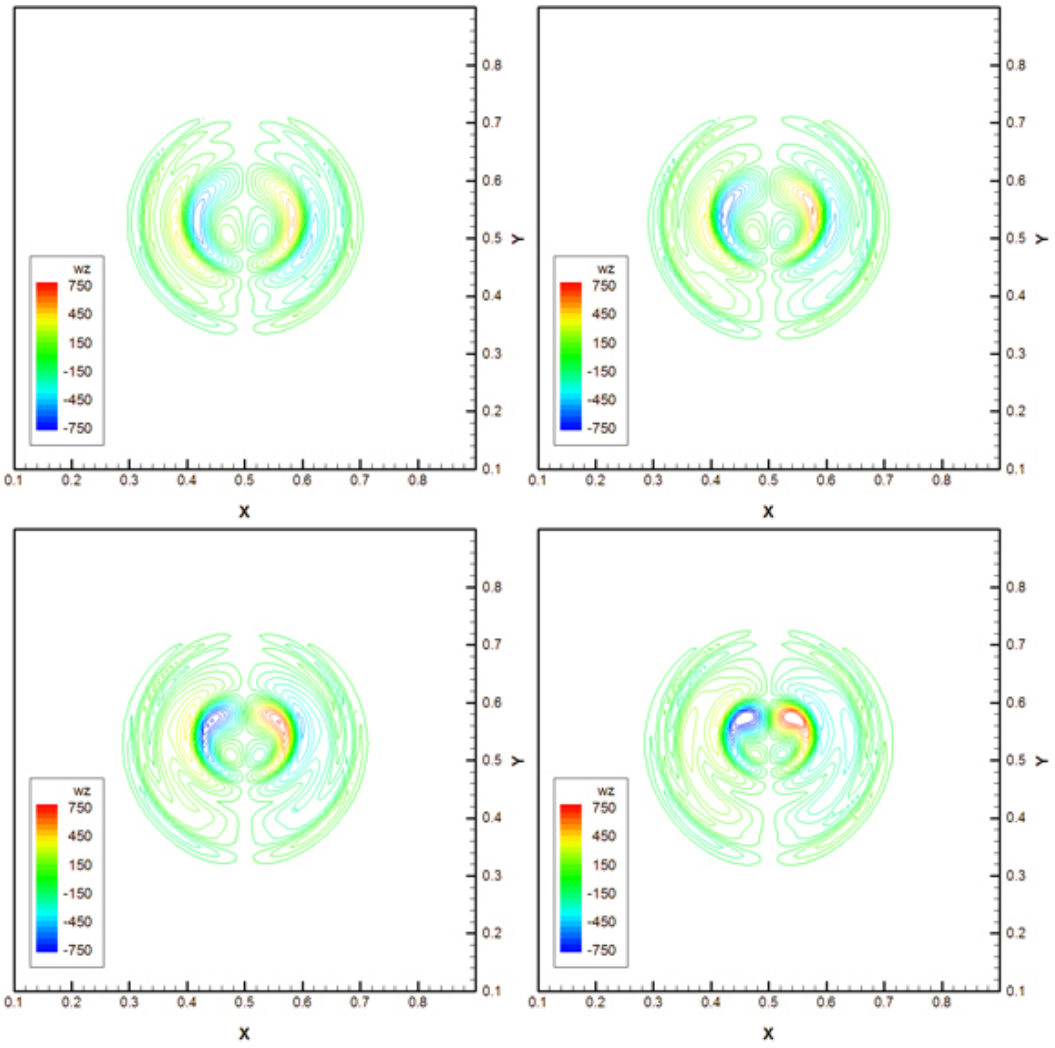

Figure A3, Continued. Contour plots in an x-y plane for the solitary ring simulations at Re = 1400. The x-y plane is taken through the centroid of the x and y vorticity, which approximates the center of the vortex ring core. Images correspond to times of 0.010s, 0.012s, 0.014s, 0.016s, and should be viewed in the order: top left, top right, bottom left, bottom right.

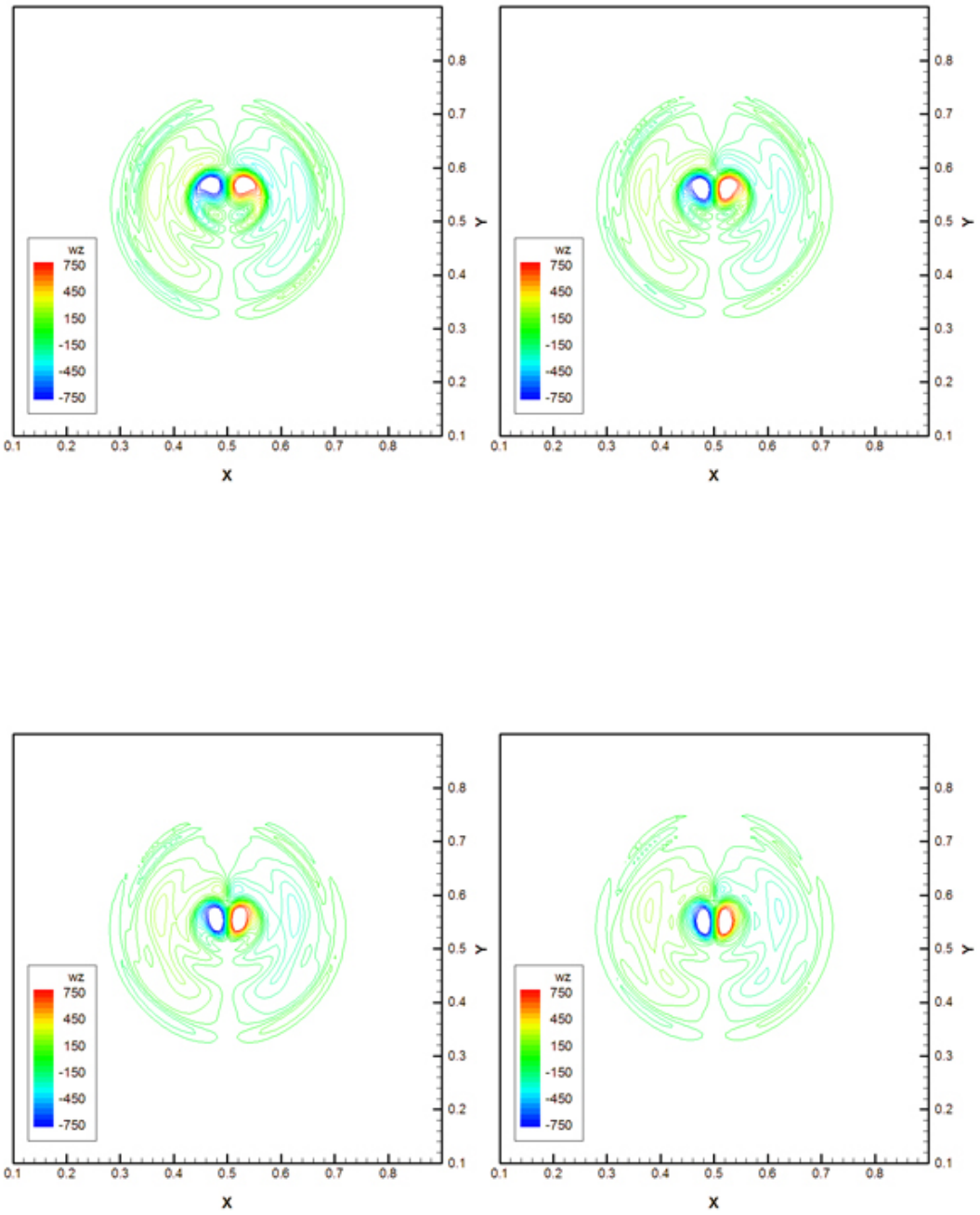

Figure A3, Continued. Contour plots in an x-y plane for the solitary ring simulations at Re = 1400. The x-y plane is taken through the centroid of the x and y vorticity, which approximates the center of the vortex ring core. Images correspond to times of 0.018s, 0.020s, 0.022s, 0.024s, and should be viewed in the order: top left, top right, bottom left, bottom right.

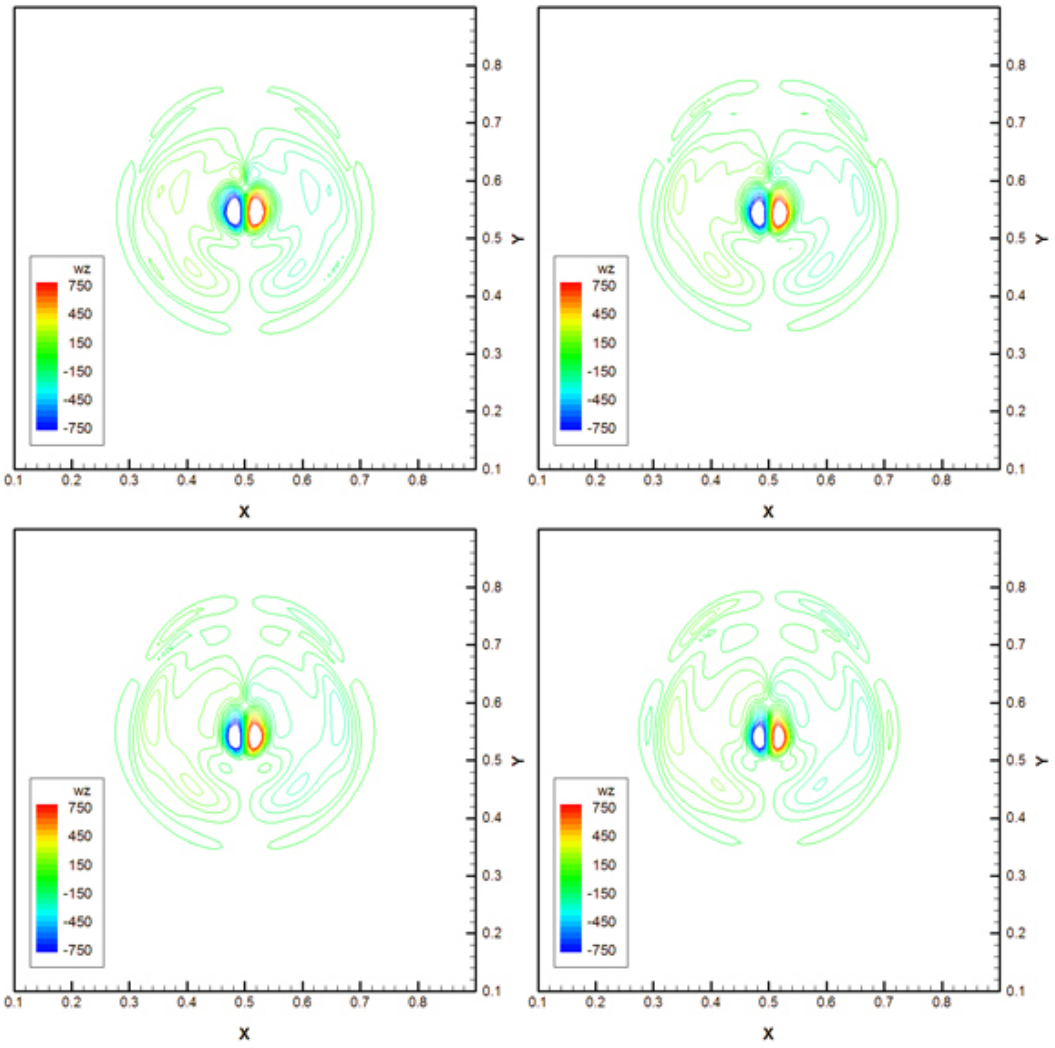

Figure A3, Continued. Contour plots in an x-y plane for the solitary ring simulations at Re = 1400. The x-y plane is taken through the centroid of the x and y vorticity, which approximates the center of the vortex ring core. Images correspond to times of 0.026s, 0.028s, 0.030s, 0.032s, and should be viewed in the order: top left, top right, bottom left, bottom right.

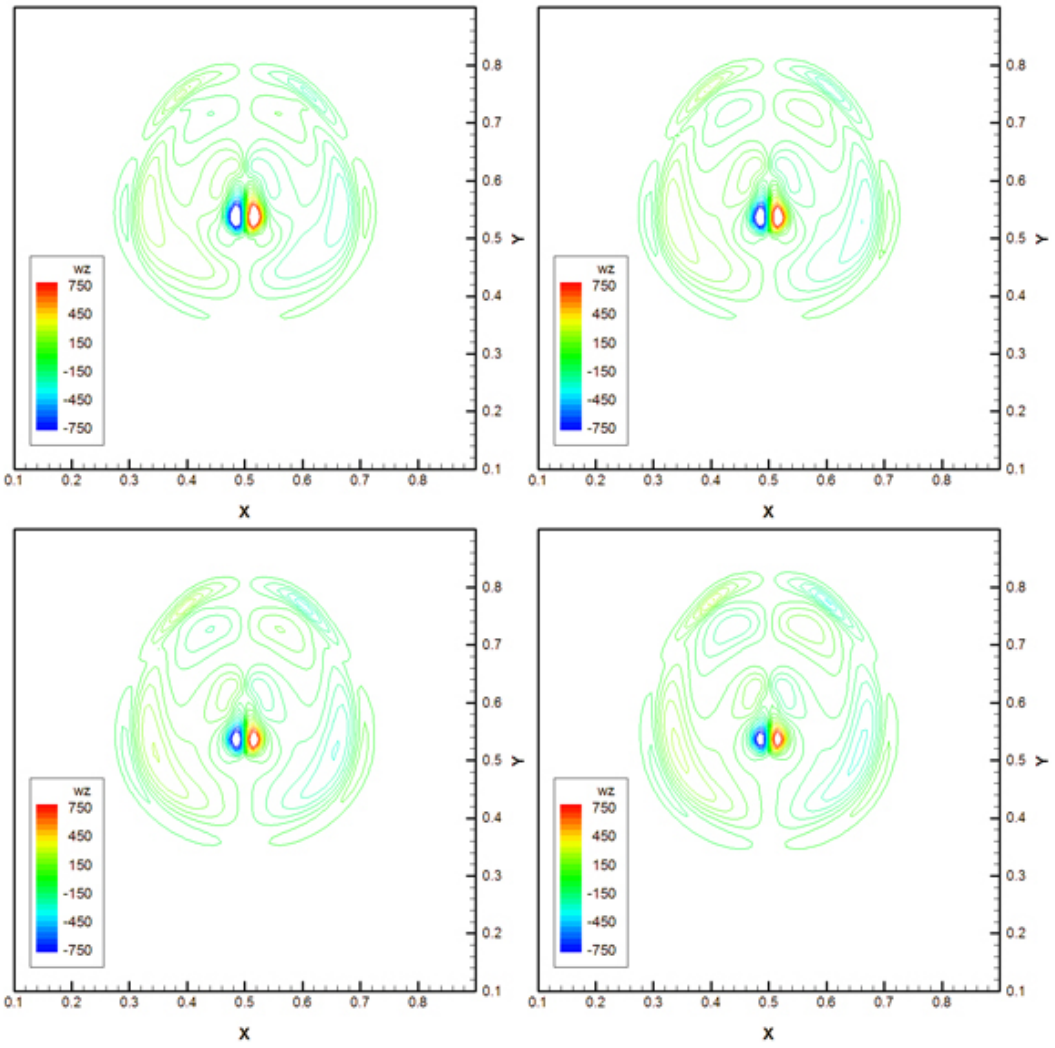

Figure A3, Continued. Contour plots in an x-y plane for the solitary ring simulations at Re = 1400. The x-y plane is taken through the centroid of the x and y vorticity, which approximates the center of the vortex ring core. Images correspond to times of 0.034s, 0.036s, 0.038s, 0.040s, and should be viewed in the order: top left, top right, bottom left, bottom right.

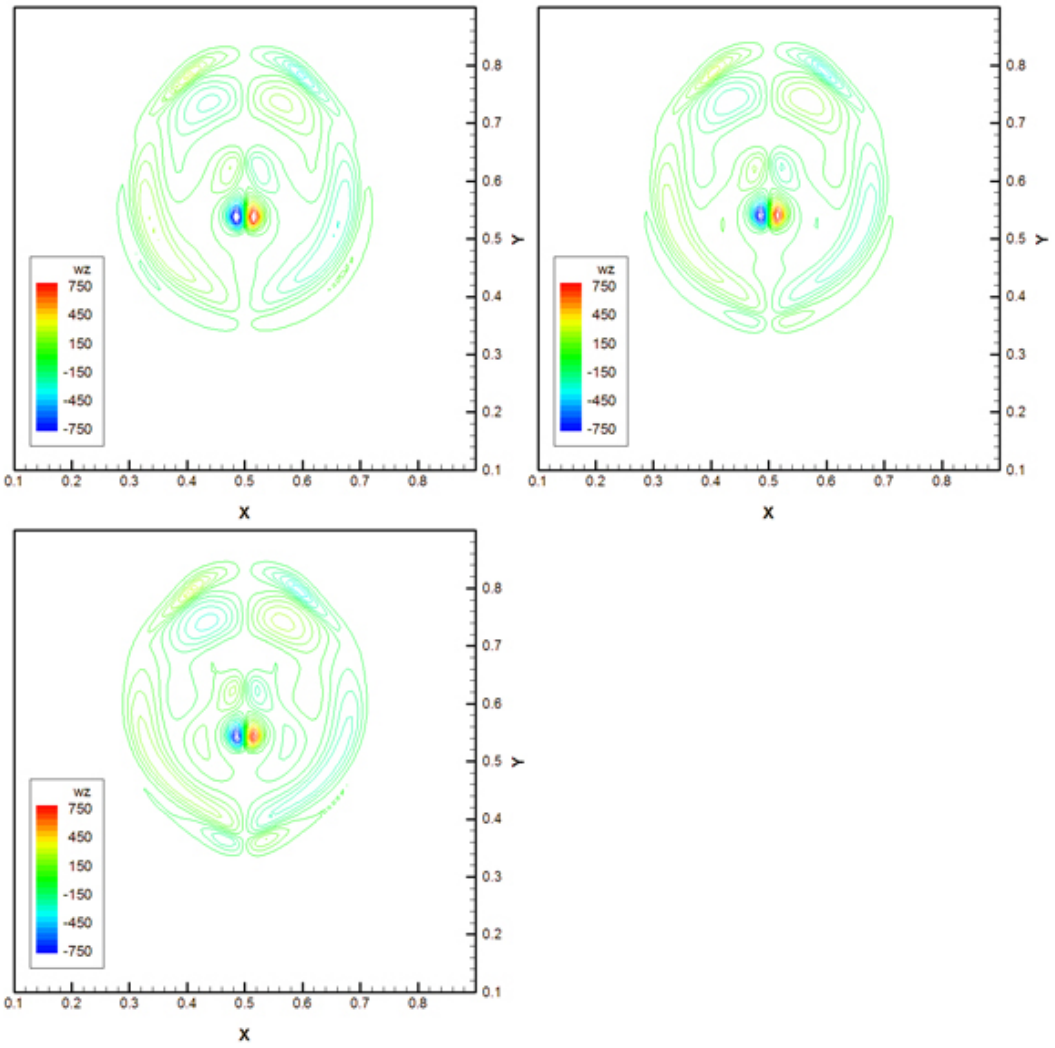

Figure A3, Continued. Contour plots in an x-y plane for the solitary ring simulations at Re = 1400. The x-y plane is taken through the centroid of the x and y vorticity, which approximates the center of the vortex ring core. Images correspond to times of 0.042s, 0.044s, 0.046s, and should be viewed in the order: top left, top right, bottom left.

Appendix 5. Contour Plots for Solitary Ring Simulations. Re = 2500.

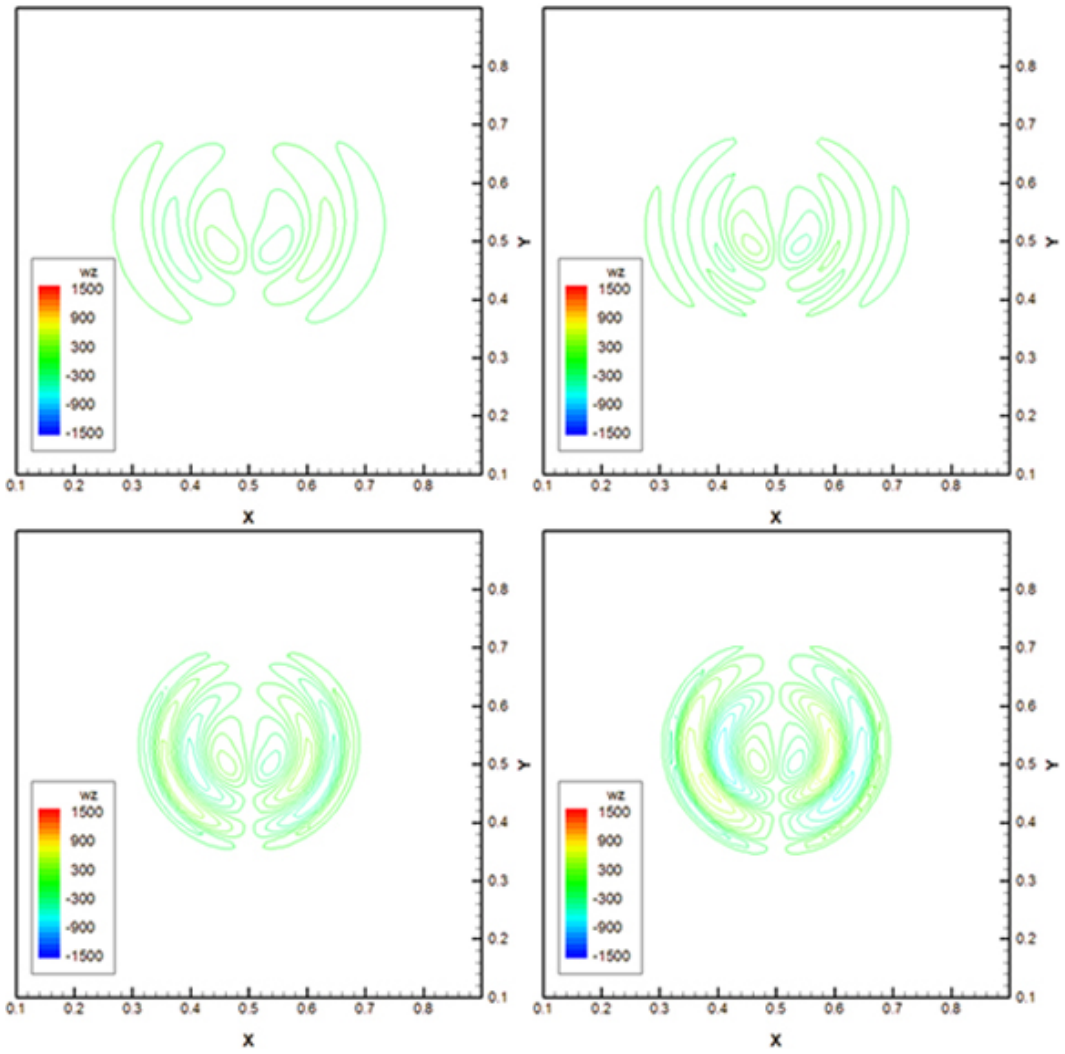

Figure A4. Contour plots in an x-y plane for the solitary ring simulations at Re = 2500. The x-y plane is taken through the centroid of the x and y vorticity, which approximates the center of the vortex ring core. Images correspond to times of 0.001s, 0.002s, 0.003s, 0.004s, and should be viewed in the order: top left, top right, bottom left, bottom right.

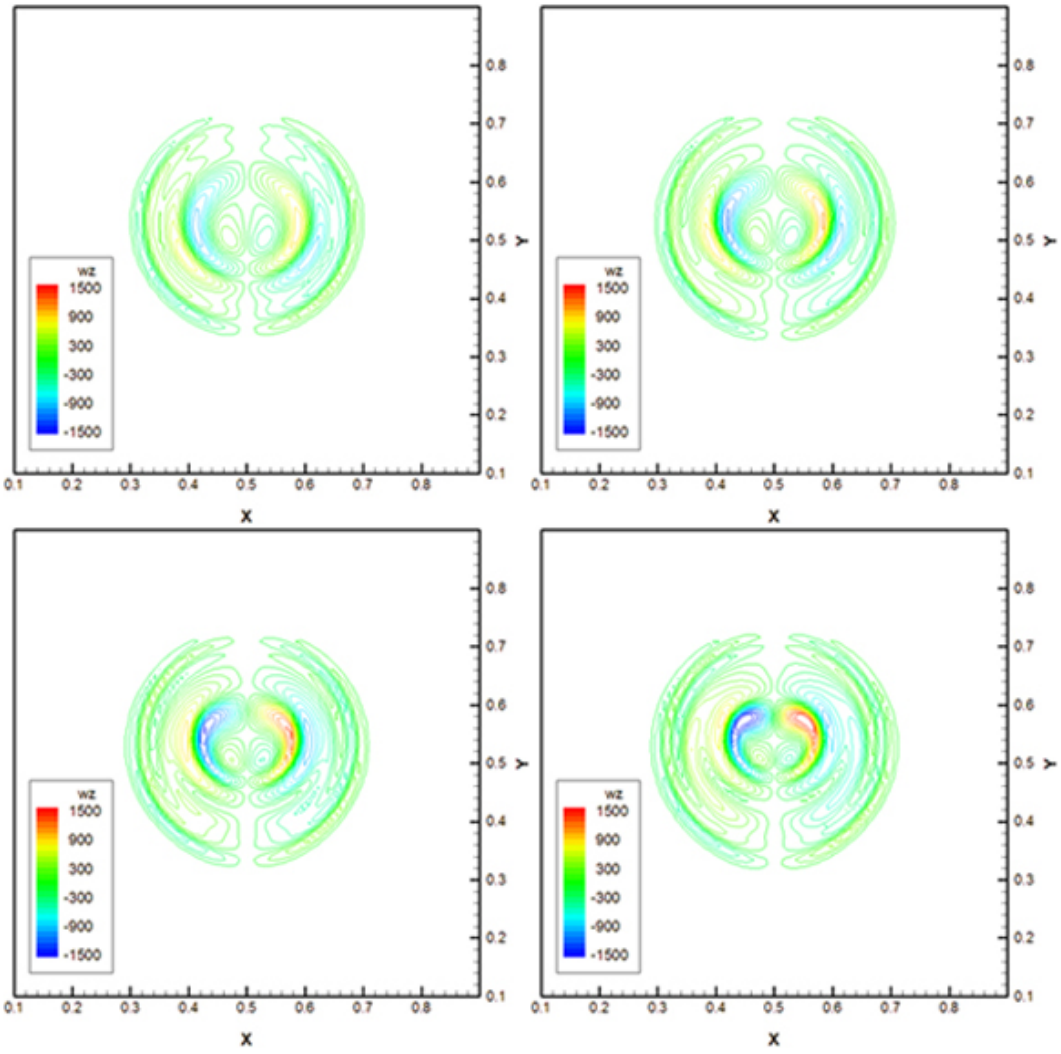

Figure A4, Continued. Contour plots in an x-y plane for the solitary ring simulations at Re = 2500. The x-y plane is taken through the centroid of the x and y vorticity, which approximates the center of the vortex ring core. Images correspond to times of 0.005s, 0.006s, 0.007s, 0.008s, and should be viewed in the order: top left, top right, bottom left, bottom right.

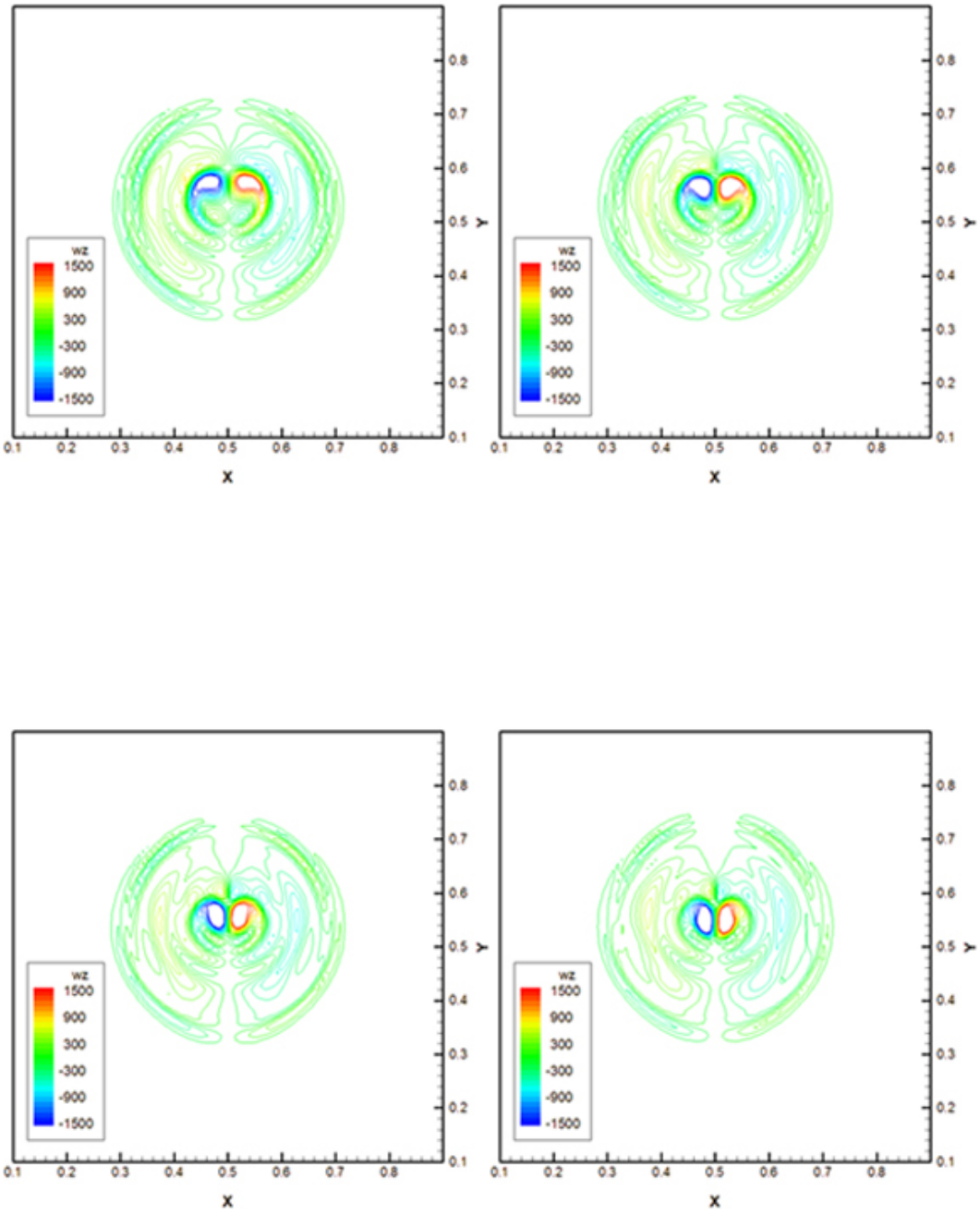

Figure A4, Continued. Contour plots in an x-y plane for the solitary ring simulations at Re = 2500. The x-y plane is taken through the centroid of the x and y vorticity, which approximates the center of the vortex ring core. Images correspond to times of 0.009s, 0.010s, 0.011s, 0.012s, and should be viewed in the order: top left, top right, bottom left, bottom right.

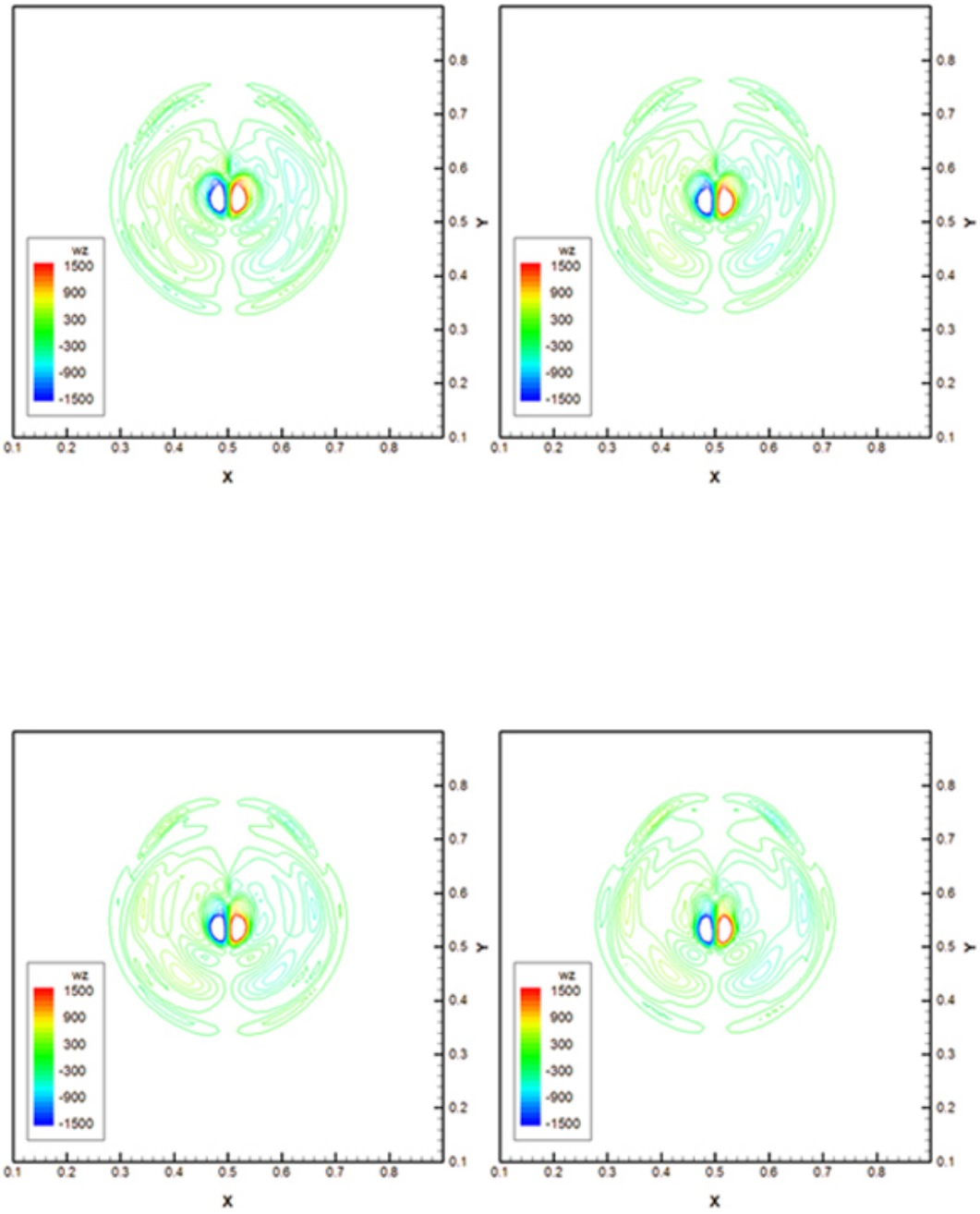

Figure A4, Continued. Contour plots in an x-y plane for the solitary ring simulations at Re = 2500. The x-y plane is taken through the centroid of the x and y vorticity, which approximates the center of the vortex ring core. Images correspond to times of 0.013s, 0.014s, 0.015s, 0.016s, and should be viewed in the order: top left, top right, bottom left, bottom right.

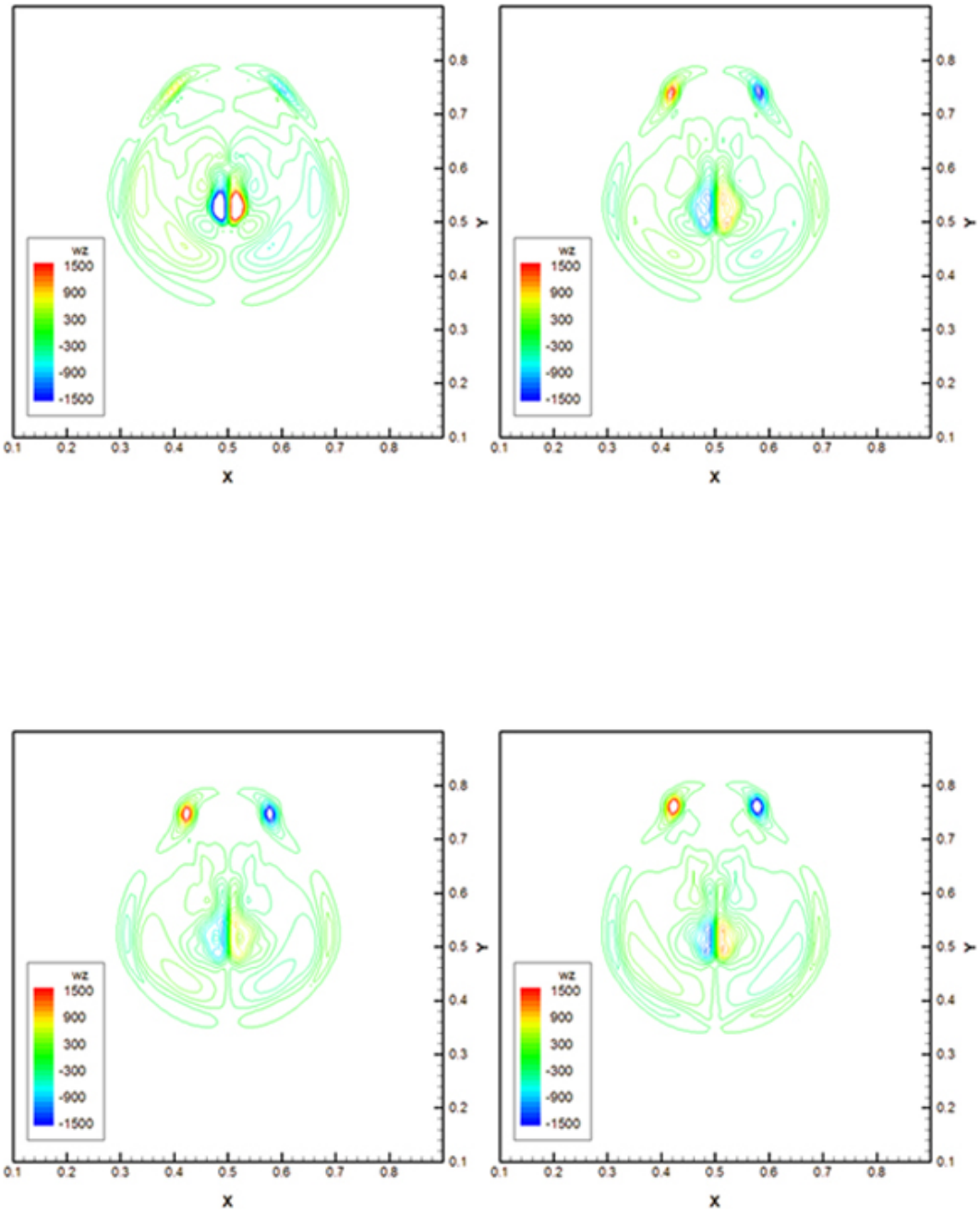

Figure A4, Continued. Contour plots in an x-y plane for the solitary ring simulations at Re = 2500. The x-y plane is taken through the centroid of the x and y vorticity, which approximates the center of the vortex ring core. Images correspond to times of 0.017s, 0.018s, 0.019s, 0.020s, and should be viewed in the order: top left, top right, bottom left, bottom right.

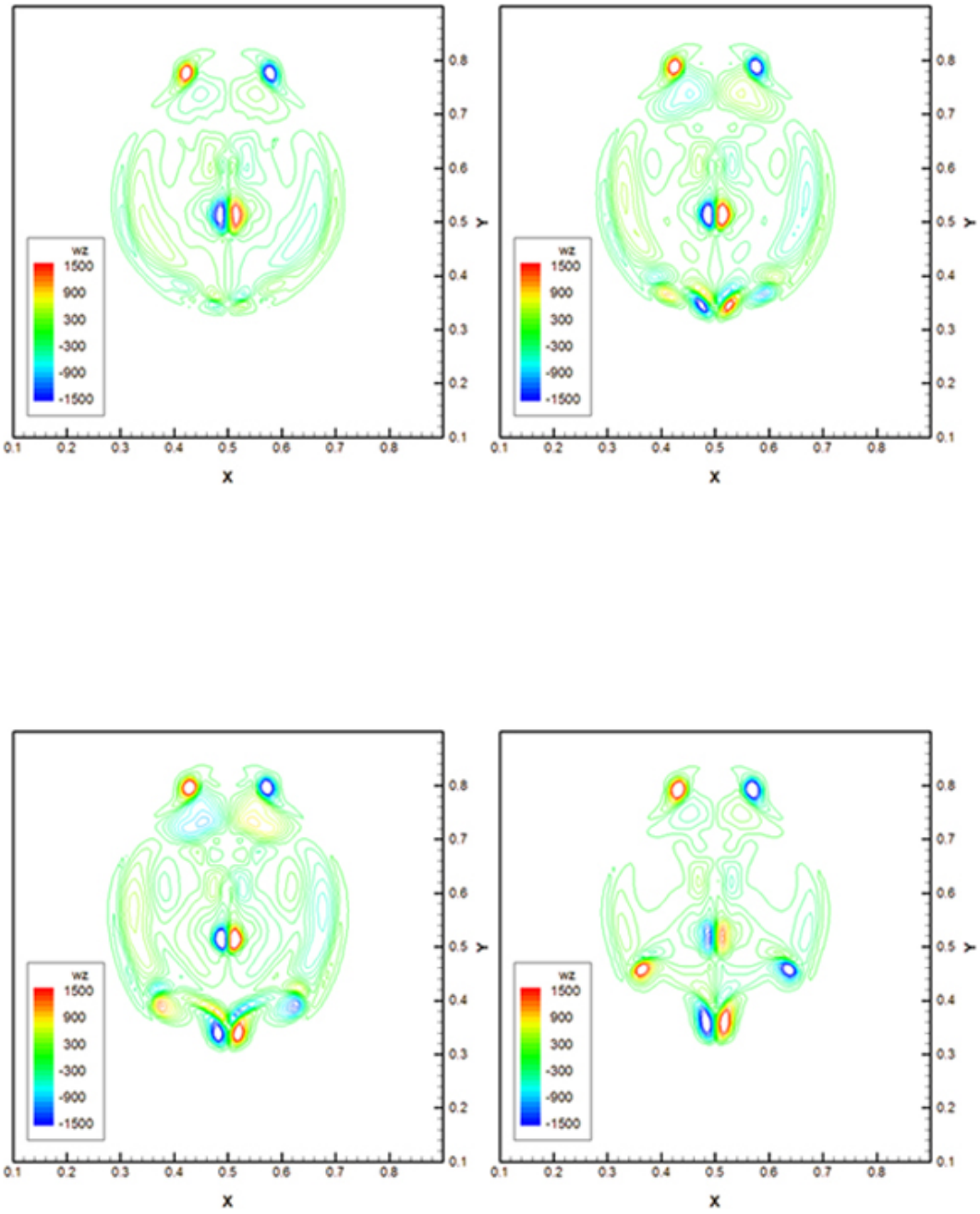

Figure A4, Continued. Contour plots in an x-y plane for the solitary ring simulations at Re = 2500. The x-y plane is taken through the centroid of the x and y vorticity, which approximates the center of the vortex ring core. Images correspond to times of 0.021s, 0.022s, 0.023s, 0.024s, and should be viewed in the order: top left, top right, bottom left, bottom right.

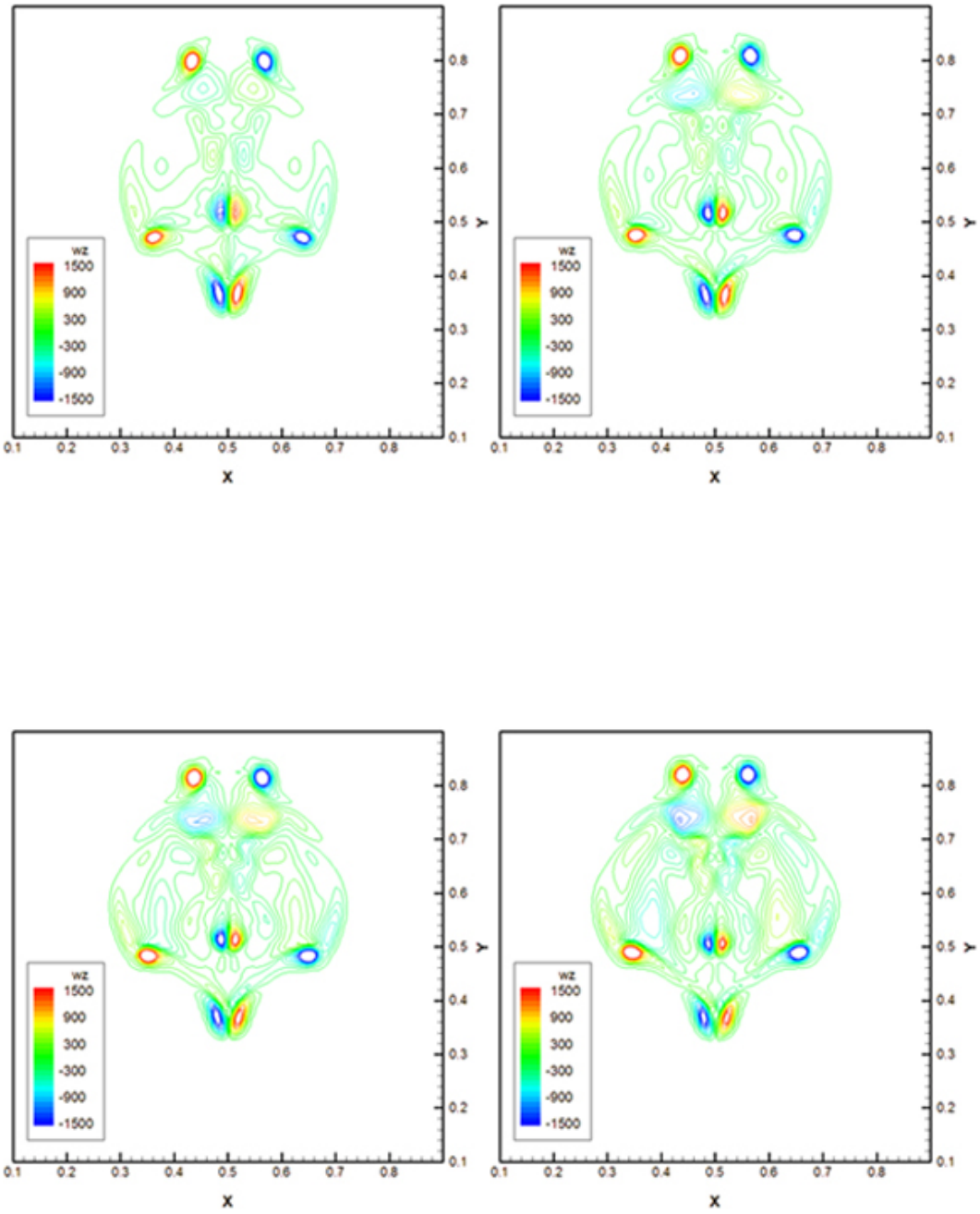

Figure A4, Continued. Contour plots in an x-y plane for the solitary ring simulations at Re = 2500. The x-y plane is taken through the centroid of the x and y vorticity, which approximates the center of the vortex ring core. Images correspond to times of 0.025s, 0.026s, 0.027s, 0.028s, and should be viewed in the order: top left, top right, bottom left, bottom right.

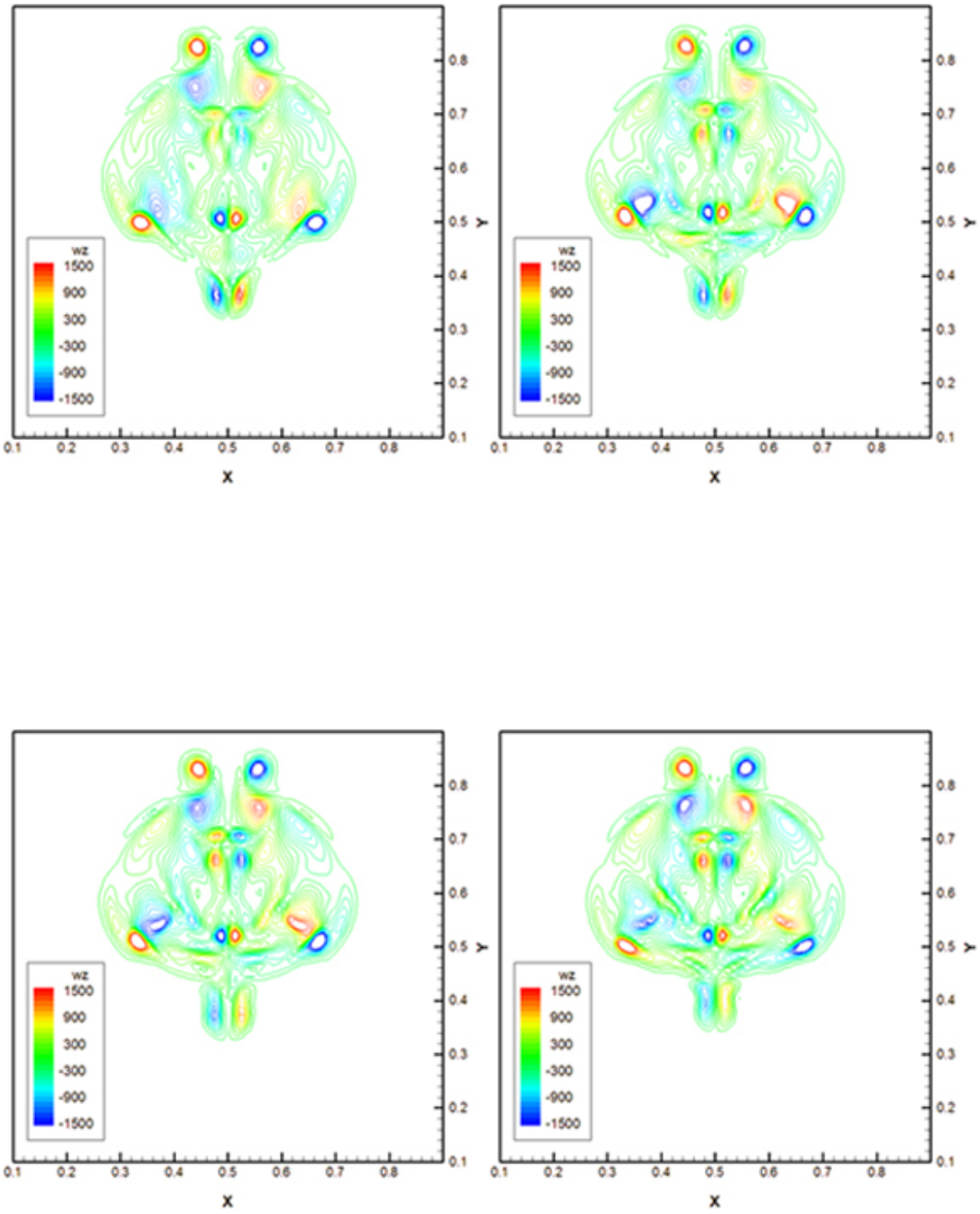

Figure A4, Continued. Contour plots in an x-y plane for the solitary ring simulations at Re = 2500. The x-y plane is taken through the centroid of the x and y vorticity, which approximates the center of the vortex ring core. Images correspond to times of 0.029s, 0.030s, 0.031s, 0.032s, and should be viewed in the order: top left, top right, bottom left, bottom right.

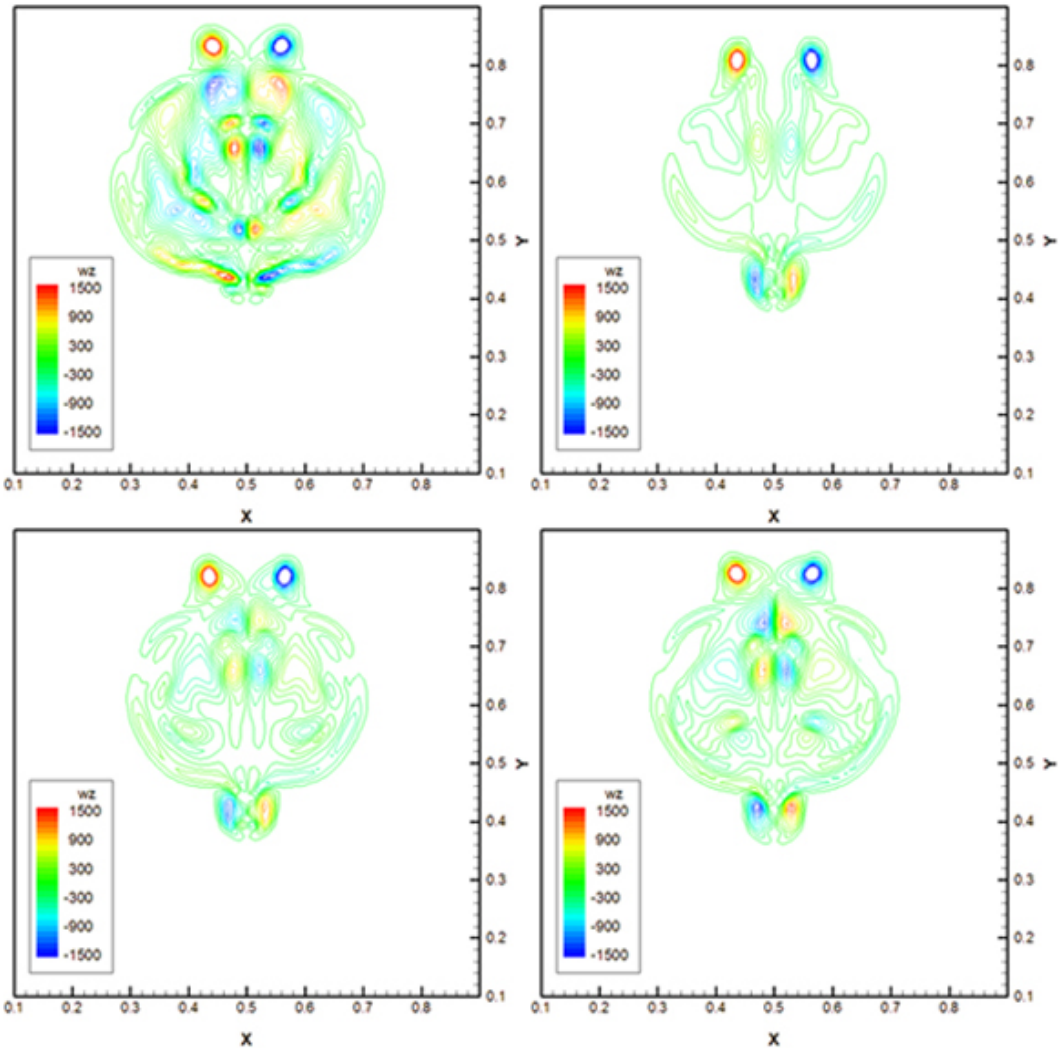

Figure A4, Continued. Contour plots in an x-y plane for the solitary ring simulations at Re = 2500. The x-y plane is taken through the centroid of the x and y vorticity, which approximates the center of the vortex ring core. Images correspond to times of 0.033s, 0.034s, 0.035s, 0.036s, and should be viewed in the order: top left, top right, bottom left, bottom right.

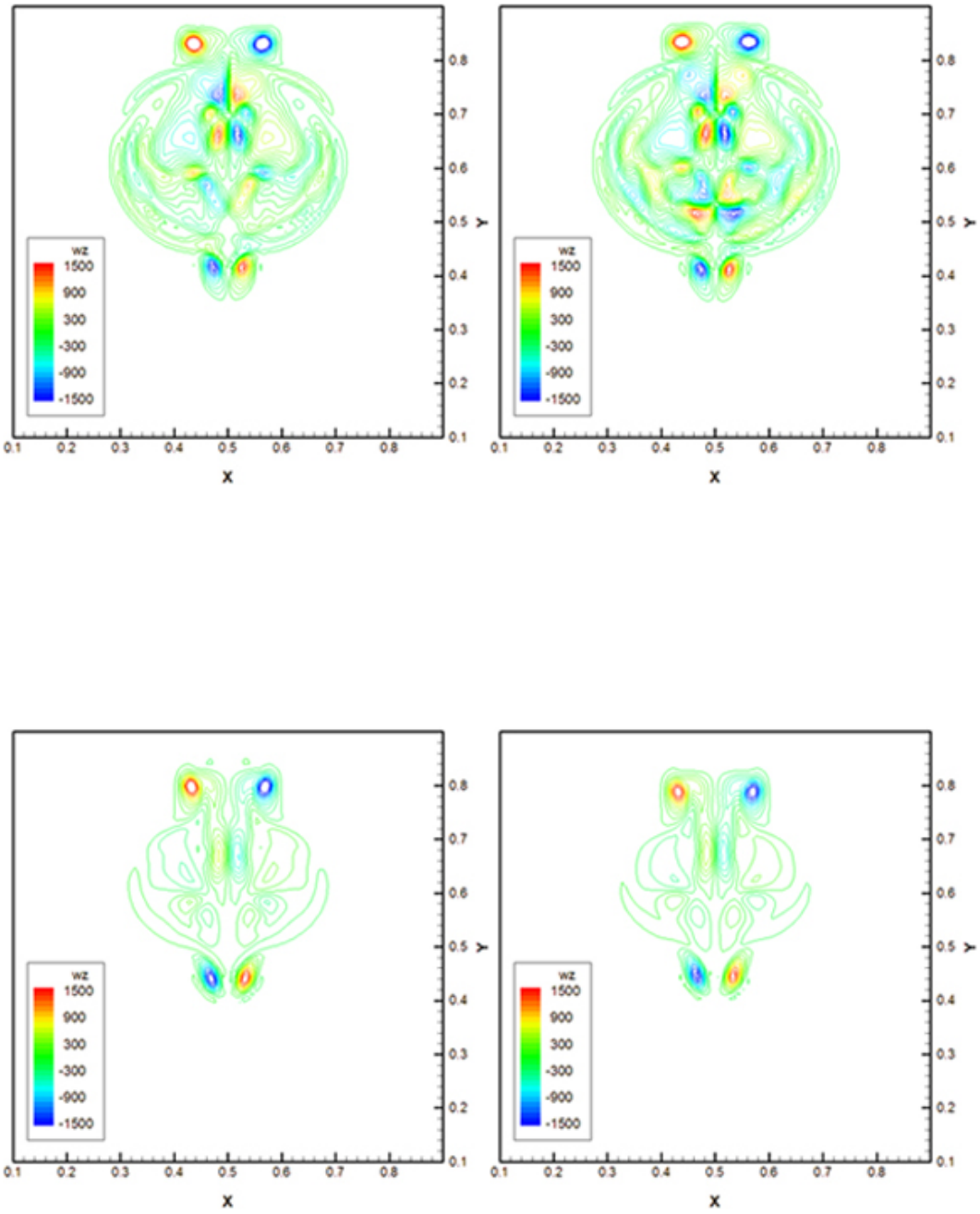

Figure A4, Continued. Contour plots in an x-y plane for the solitary ring simulations at Re = 2500. The x-y plane is taken through the centroid of the x and y vorticity, which approximates the center of the vortex ring core. Images correspond to times of 0.037s, 0.038s, 0.039s, 0.040s, and should be viewed in the order: top left, top right, bottom left, bottom right.

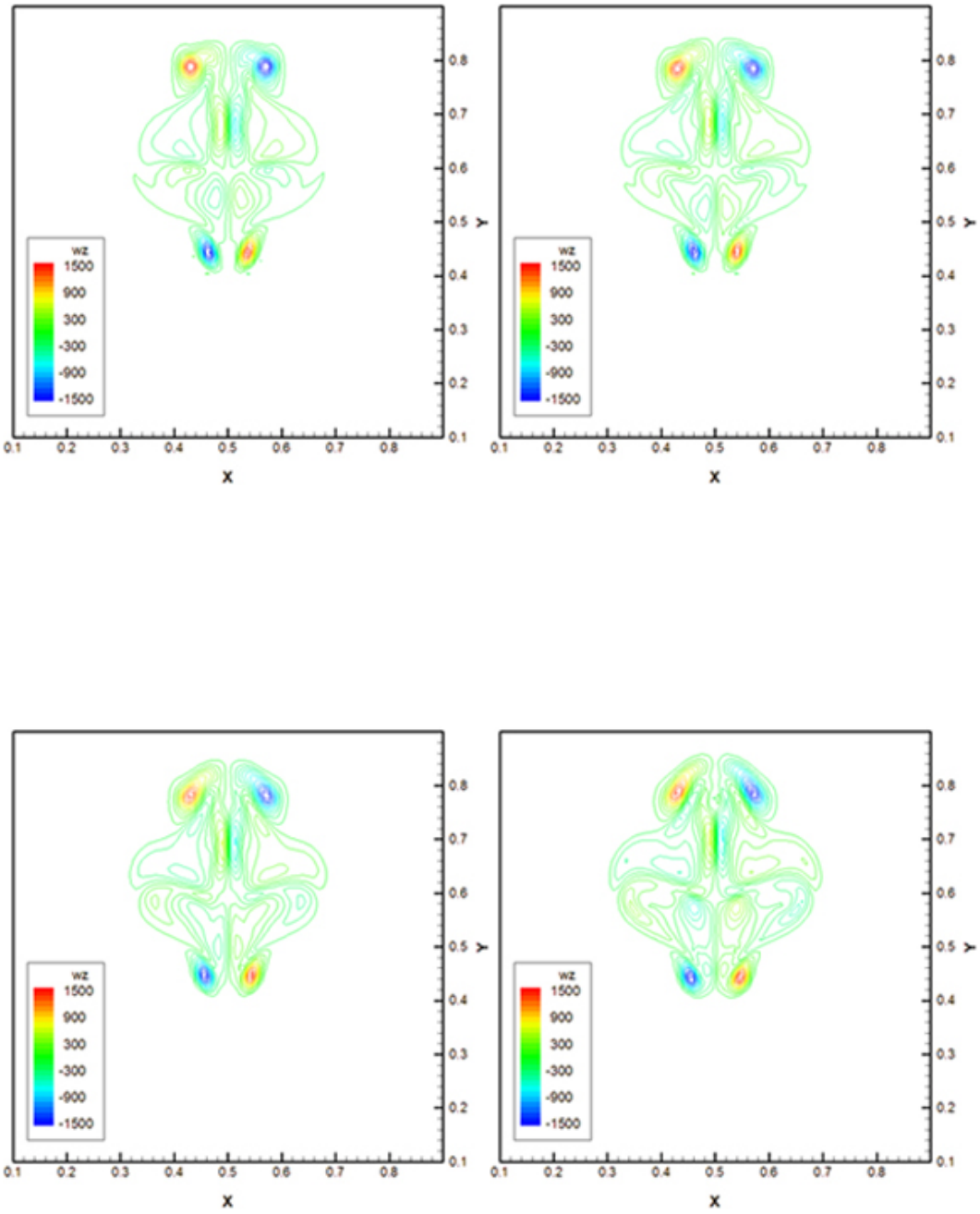

Figure A4, Continued. Contour plots in an x-y plane for the solitary ring simulations at Re = 2500. The x-y plane is taken through the centroid of the x and y vorticity, which approximates the center of the vortex ring core. Images correspond to times of 0.041s, 0.042s, 0.043s, 0.044s, and should be viewed in the order: top left, top right, bottom left, bottom right.

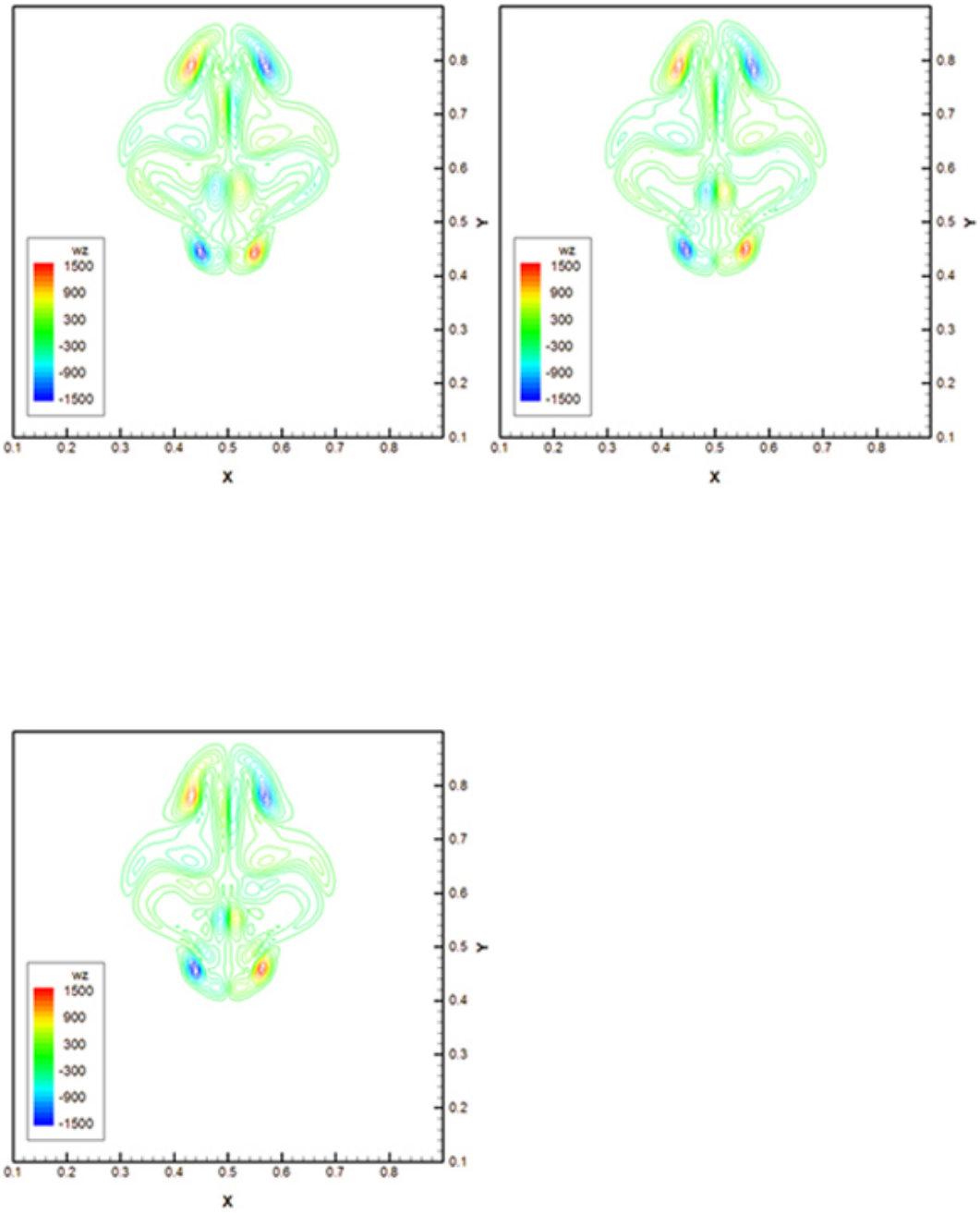

Figure A4, Continued. Contour plots in an x-y plane for the solitary ring simulations at Re = 2500. The x-y plane is taken through the centroid of the x and y vorticity, which approximates the center of the vortex ring core. Images correspond to times of 0.045s, 0.046s, 0.047s, and should be viewed in the order: top left, top right, bottom left.

Appendix 6. Wave-Number Growth for ω_r, Re = 2500

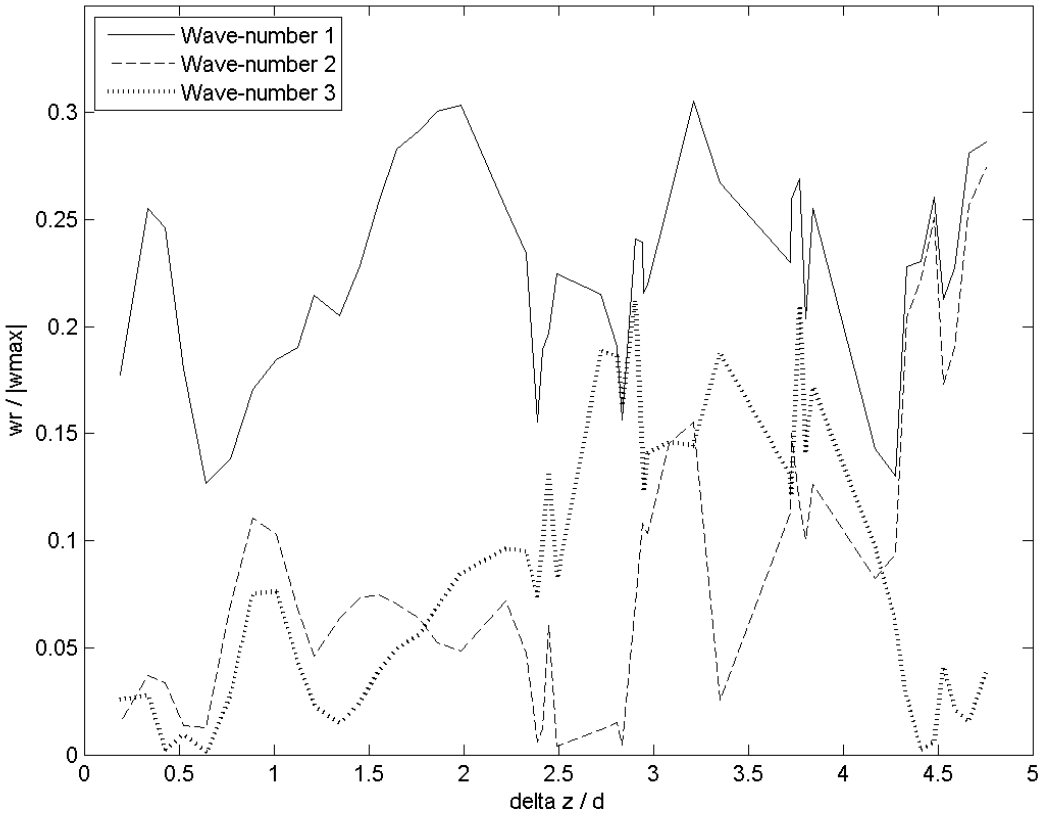

Figure A5. Instability growth of wave-numbers 1-3 for ω_r at Re = 2500. The horizontal axis is the number of ring diameters the vortex ring has travelled. The vertical axis is the amplitude of the instability compared to the maximum vorticity magnitude around the azimuth of the vortex ring.

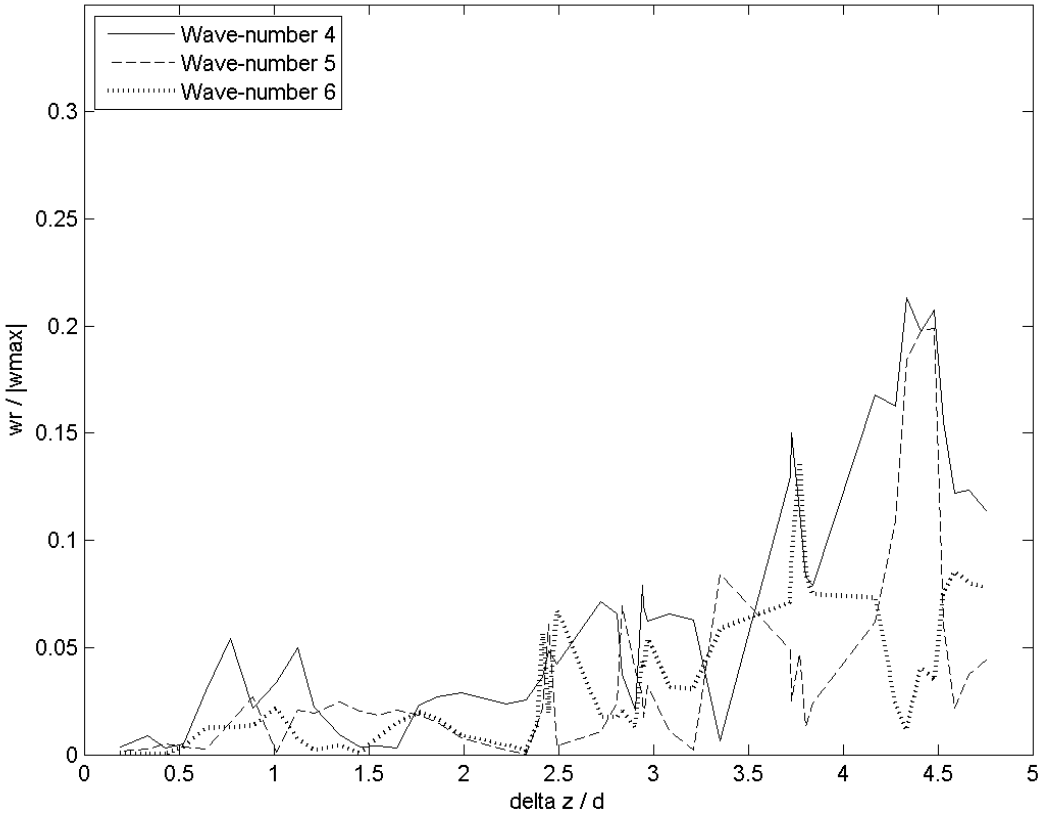

Figure A6. Instability growth of wave-numbers 4-6 for ω_r at Re = 2500. The horizontal axis is the number of ring diameters the vortex ring has travelled. The vertical axis is the amplitude of the instability compared to the maximum vorticity magnitude around the azimuth of the vortex ring.

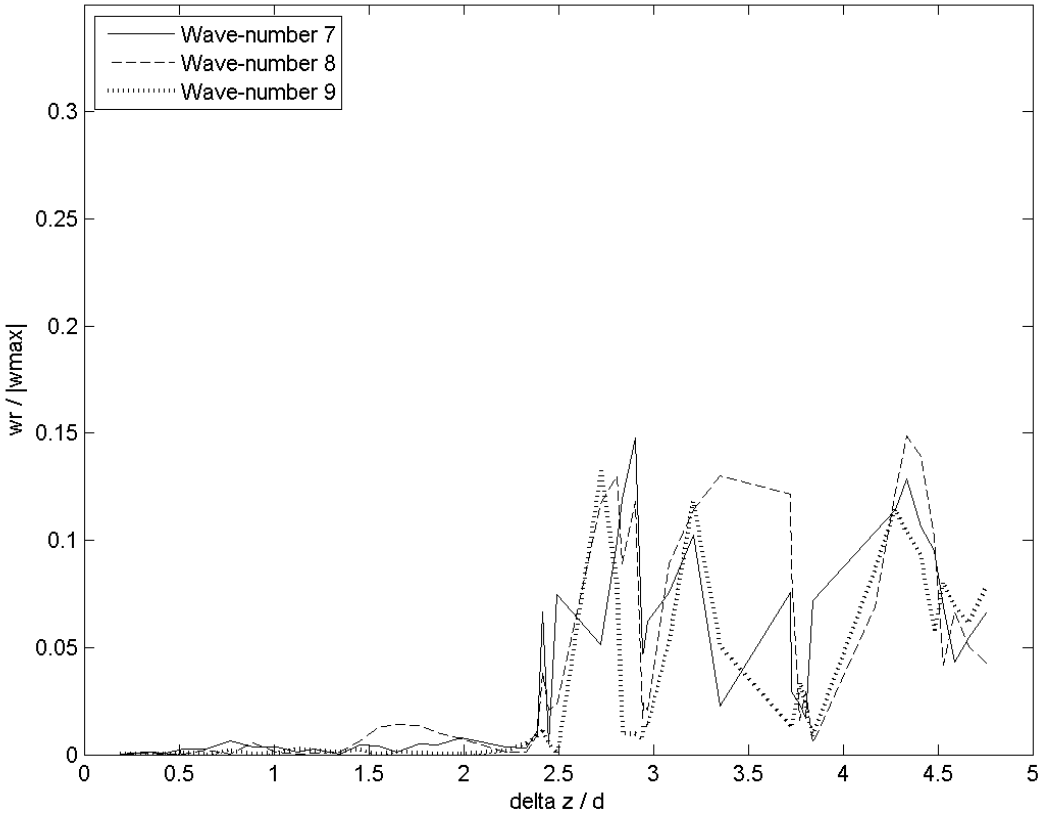

Figure A7. Instability growth of wave-numbers 7-9 for ω_r at Re = 2500. The horizontal axis is the number of ring diameters the vortex ring has travelled. The vertical axis is the amplitude of the instability compared to the maximum vorticity magnitude around the azimuth of the vortex ring.

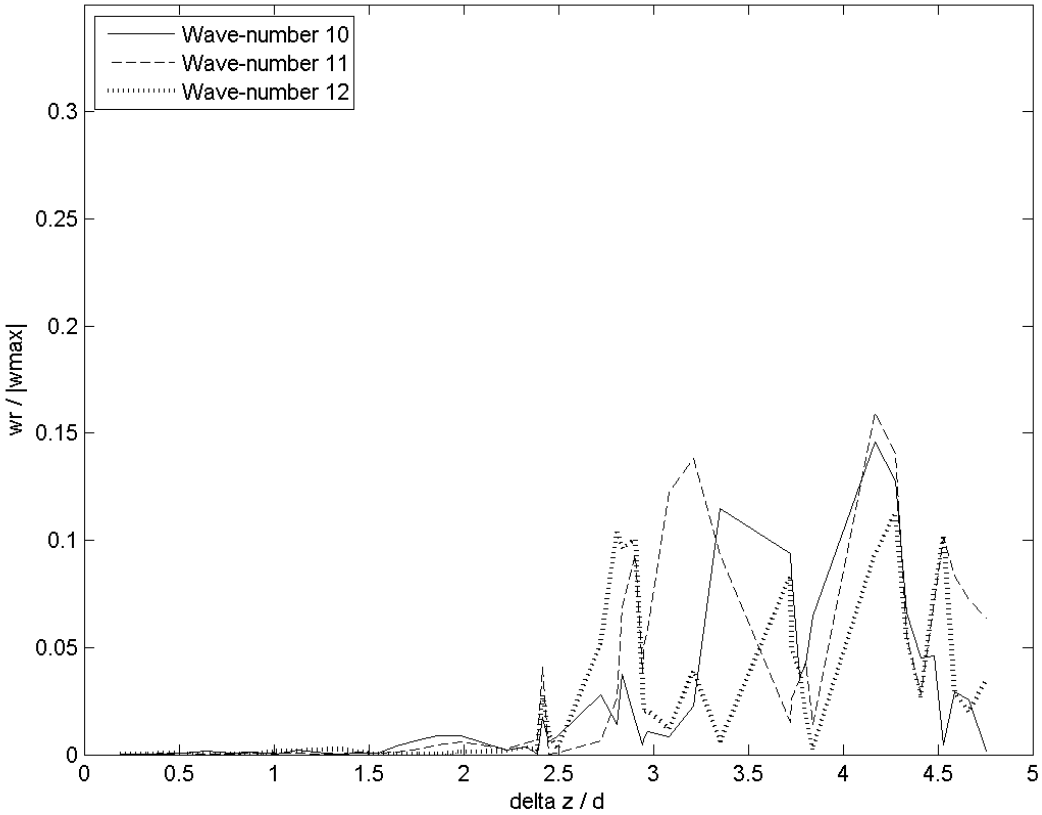

Figure A8. Instability growth of wave-numbers 10-12 for ω_r at Re = 2500. The horizontal axis is the number of ring diameters the vortex ring has travelled. The vertical axis is the amplitude of the instability compared to the maximum vorticity magnitude around the azimuth of the vortex ring.

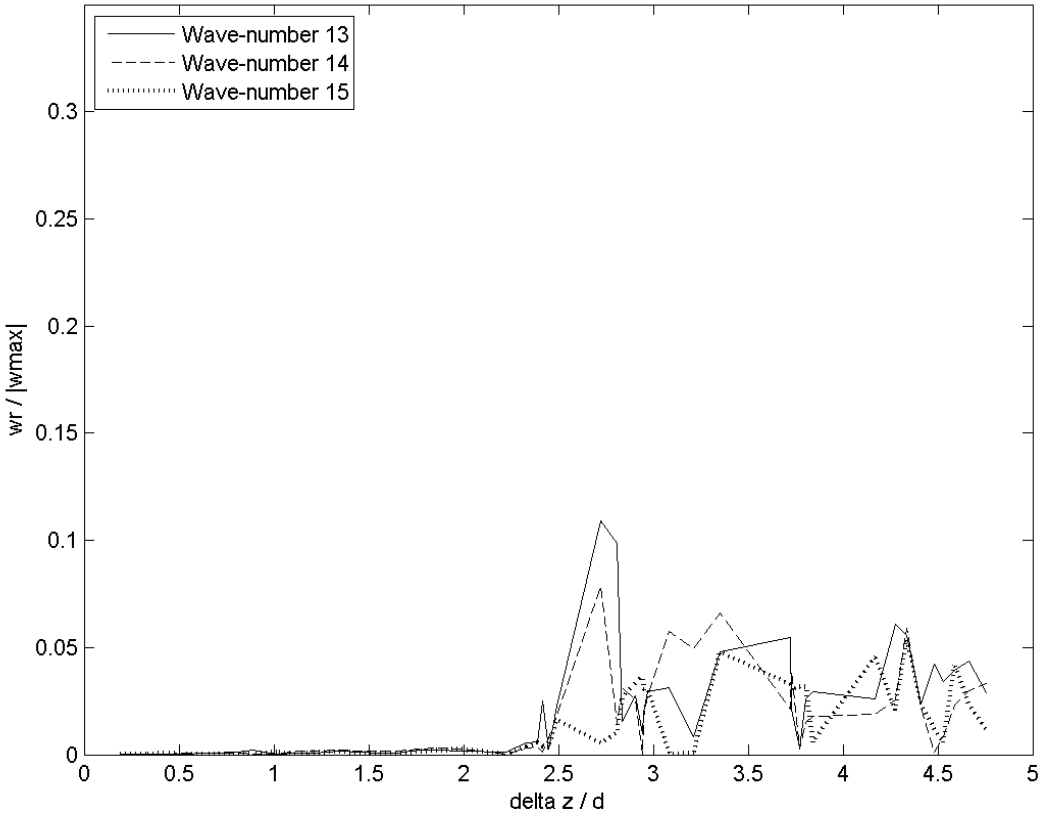

Figure A9. Instability growth of wave-numbers 13-15 for ω_r at Re = 2500. The horizontal axis is the number of ring diameters the vortex ring has travelled. The vertical axis is the amplitude of the instability compared to the maximum vorticity magnitude around the azimuth of the vortex ring.

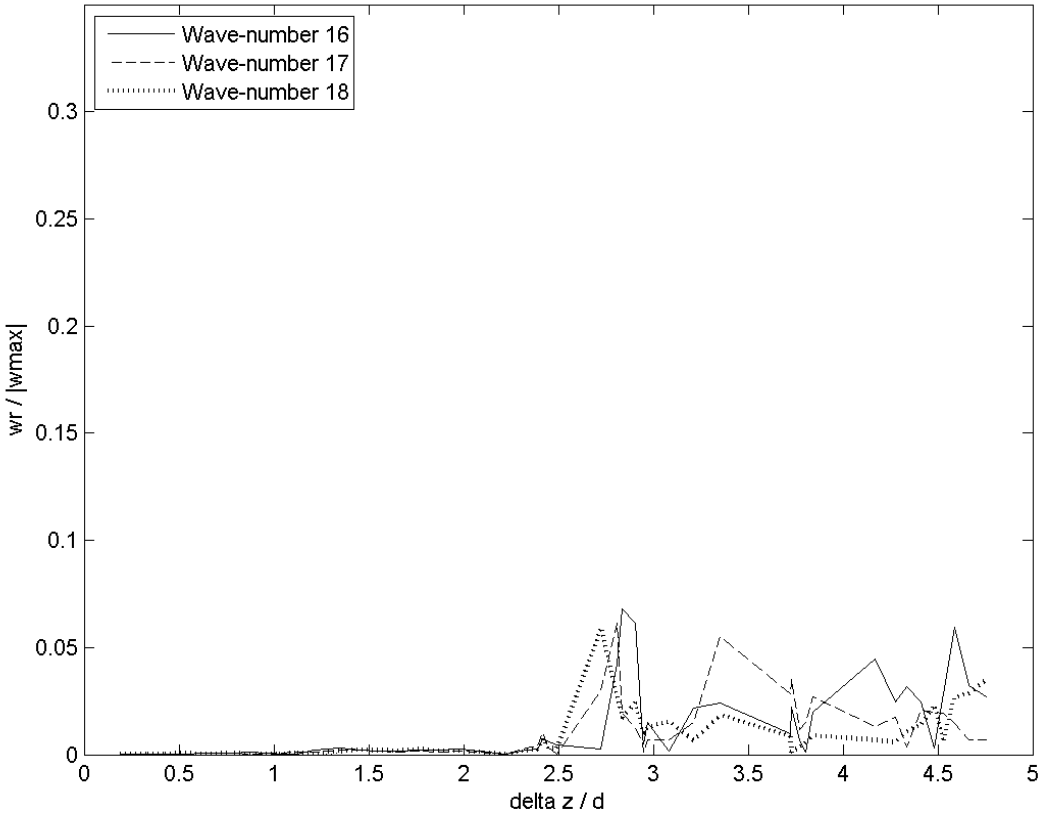

Figure A10. Instability growth of wave-numbers 16-18 for ω_r at Re = 2500. The horizontal axis is the number of ring diameters the vortex ring has travelled. The vertical axis is the amplitude of the instability compared to the maximum vorticity magnitude around the azimuth of the vortex ring.

Appendix 7. Wave-Number Growth for ω_z, Re = 2500

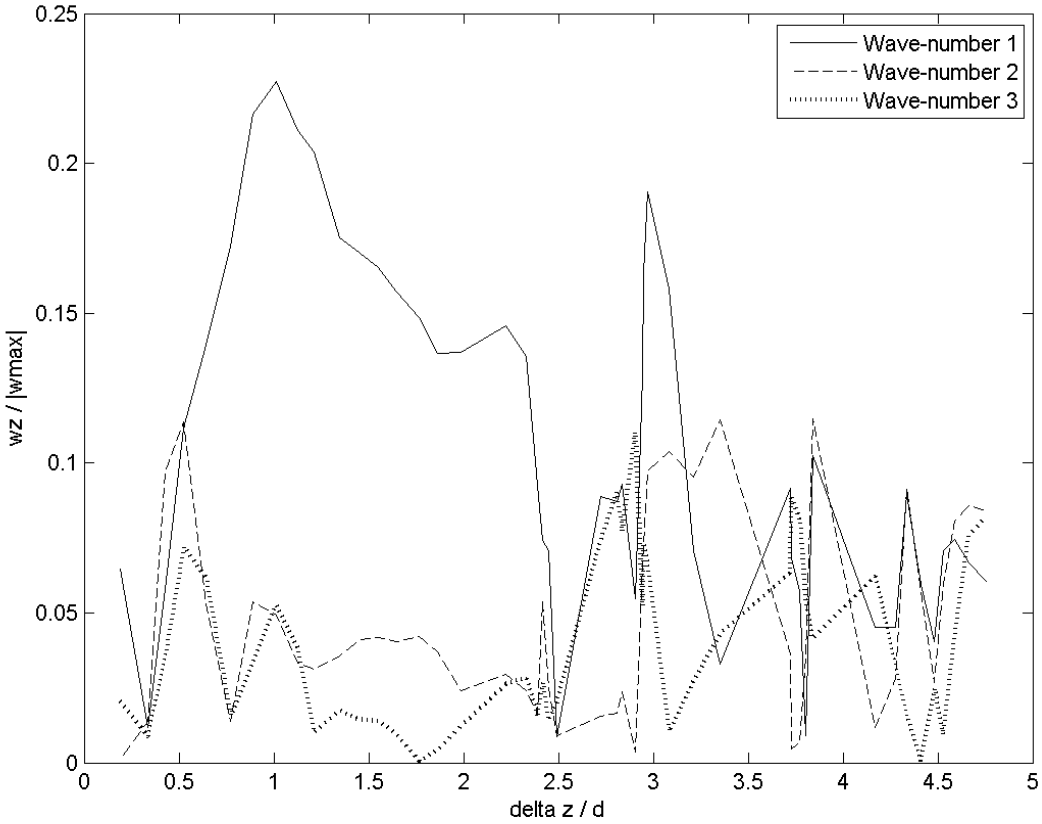

Figure A11. Instability growth of wave-numbers 1-3 for ω_z at Re = 2500. The horizontal axis is the number of ring diameters the vortex ring has travelled. The vertical axis is the amplitude of the instability compared to the maximum vorticity magnitude around the azimuth of the vortex ring.

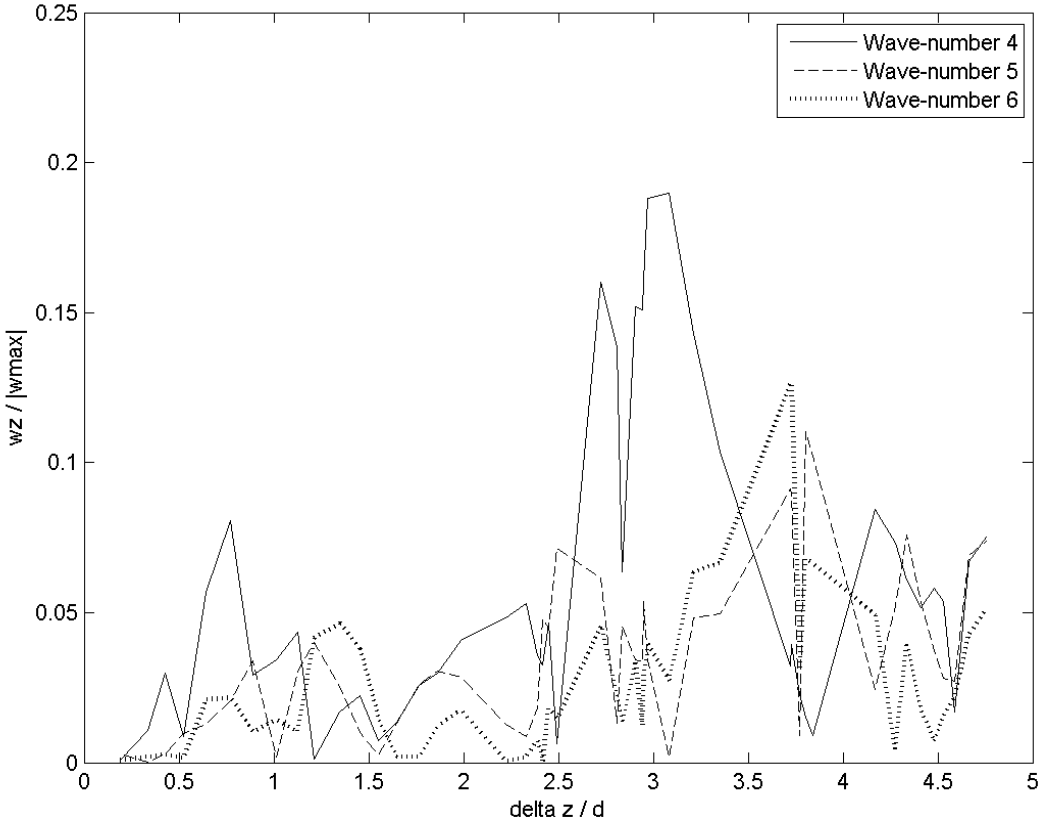

Figure A12. Instability growth of wave-numbers 4-6 for ω_z at Re = 2500. The horizontal axis is the number of ring diameters the vortex ring has travelled. The vertical axis is the amplitude of the instability compared to the maximum vorticity magnitude around the azimuth of the vortex ring.

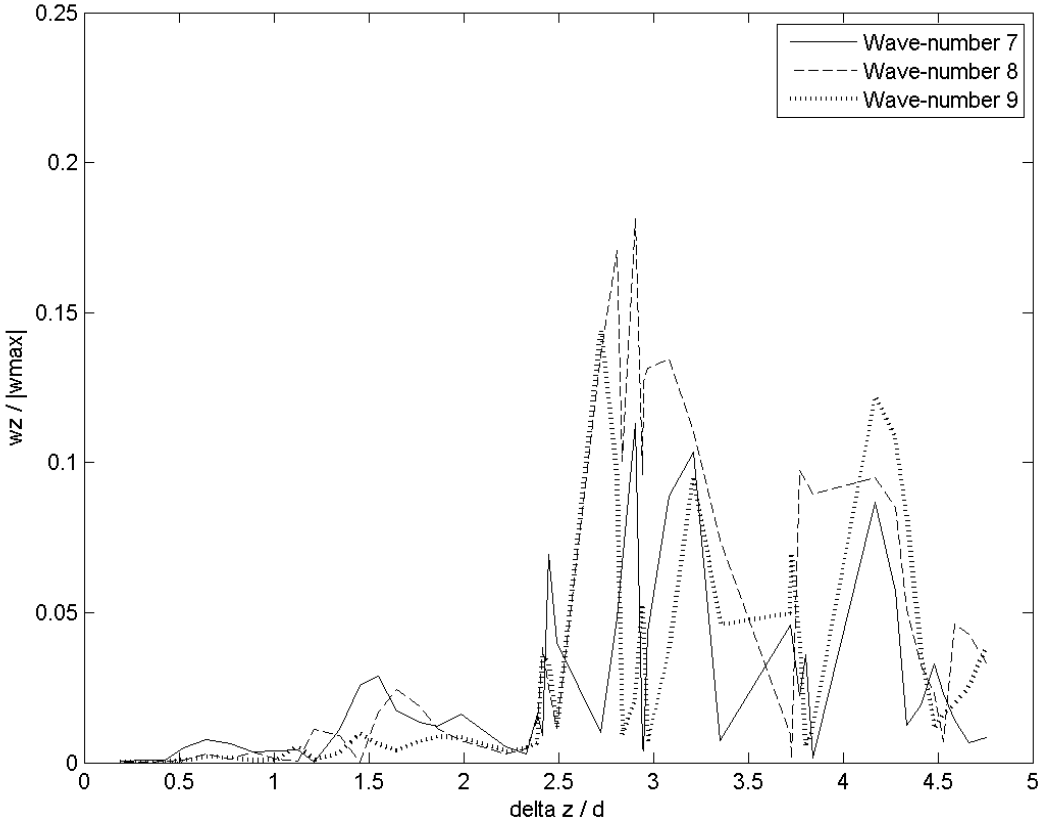

Figure A13. Instability growth of wave-numbers 7-9 for ω_z at Re = 2500. The horizontal axis is the number of ring diameters the vortex ring has travelled. The vertical axis is the amplitude of the instability compared to the maximum vorticity magnitude around the azimuth of the vortex ring.

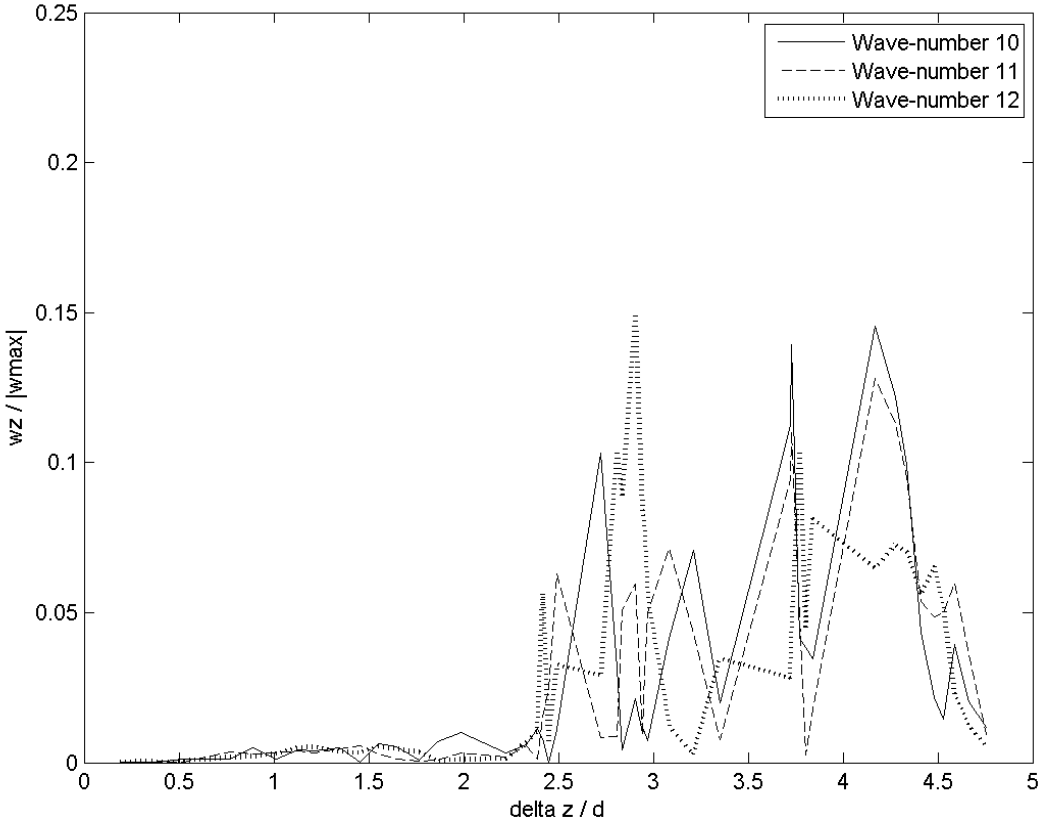

Figure A14. Instability growth of wave-numbers 10-12 for ω_z at Re = 2500. The horizontal axis is the number of ring diameters the vortex ring has travelled. The vertical axis is the amplitude of the instability compared to the maximum vorticity magnitude around the azimuth of the vortex ring.

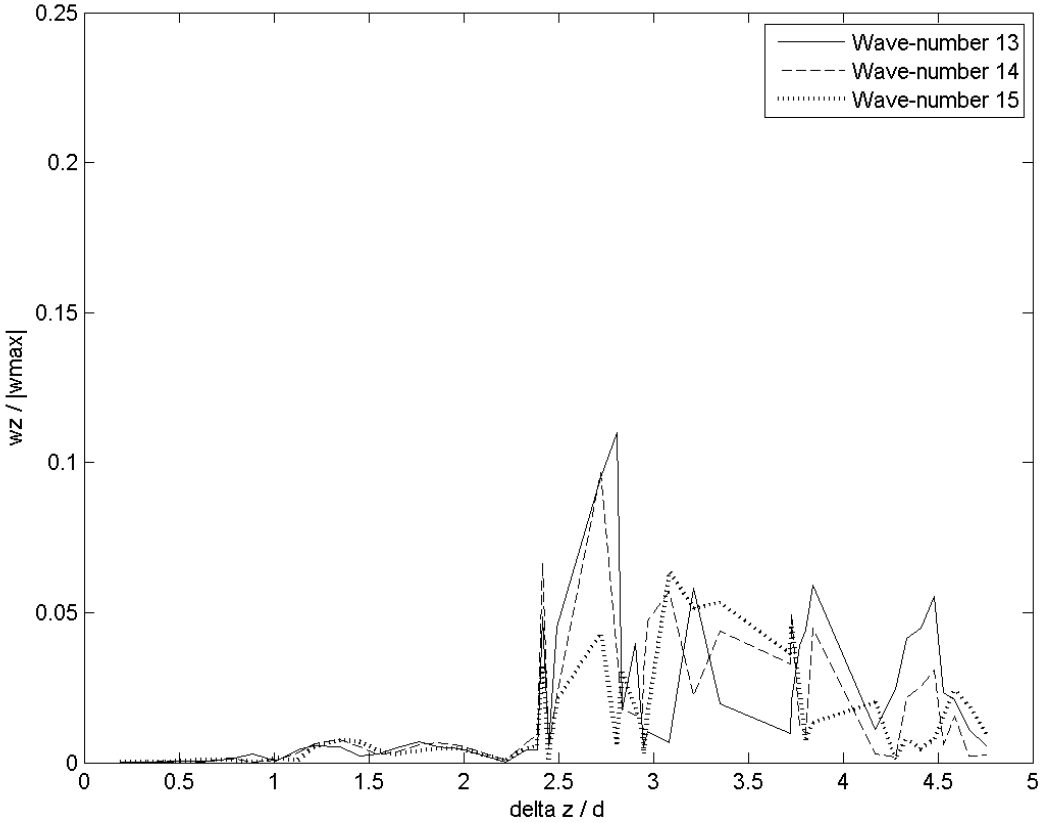

Figure A15. Instability growth of wave-numbers 13-15 for ω_z at Re = 2500. The horizontal axis is the number of ring diameters the vortex ring has travelled. The vertical axis is the amplitude of the instability compared to the maximum vorticity magnitude around the azimuth of the vortex ring.

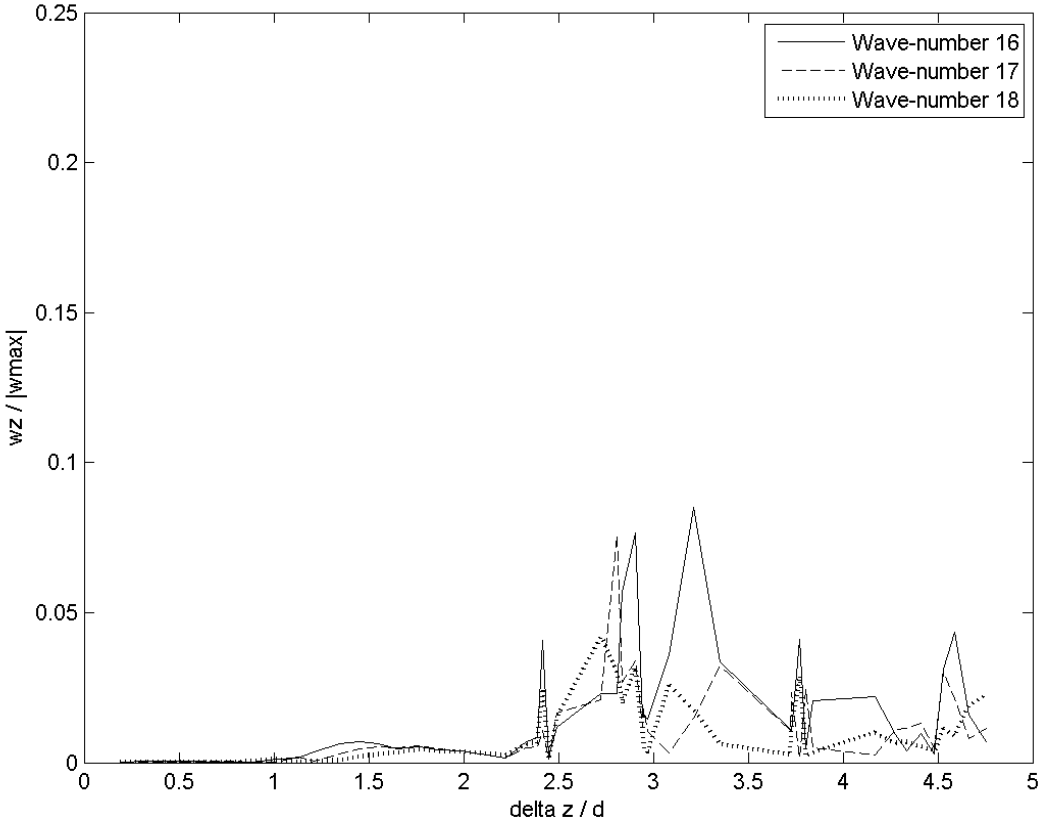

Figure A16. Instability growth of wave-numbers 16-18 for ω_z at Re = 2500. The horizontal axis is the number of ring diameters the vortex ring has travelled. The vertical axis is the amplitude of the instability compared to the maximum vorticity magnitude around the azimuth of the vortex ring.

Appendix 8. Clean Function Test

The code used a clean function to ensure the vorticity field was divergence free, which it must be for incompressibility. The random perturbation used in the simulations and discussed in Section 3.2.1 is non-physical, in the sense that it is based on a random number generator and not any physical phenomenon. Therefore, it was important to investigate the effect that the clean function had on the random perturbation to ensure that the perturbation wasn't significantly diminished or eliminated. Two simulations were run using the random perturbation, the magnitude of which was based on global maximum vorticity. An x-y slice was taken at a position away from the vortex ring, at a point that would have no vorticity were it not for the random perturbation. In this plane the visible vorticity is due exclusively to the random perturbation, and by running simulations with the clean function turned on and turned off we can see how the clean function effects the perturbation. Figure A1 shows the vorticity magnitude in the plane with the clean function turned off, and Figure A2 shows the vorticity in the plane with the clean function turned on.

The vorticity in the plane is visibly lower once the clean function is turned on. The maximum vorticity on the plane with the clean function turned off was 30.5 s^{-1}, and the maximum vorticity on the plane with the clean function turned on was 23.3 s^{-1}. This is an indication that the clean function may have reduced the random perturbation by approximately 24%. Because the amplitude of the perturbation was arbitrary, having it reduced is not a problem; the important thing is that the perturbation was not eliminated completely. The clean function did not eliminate the effect of the random perturbation.

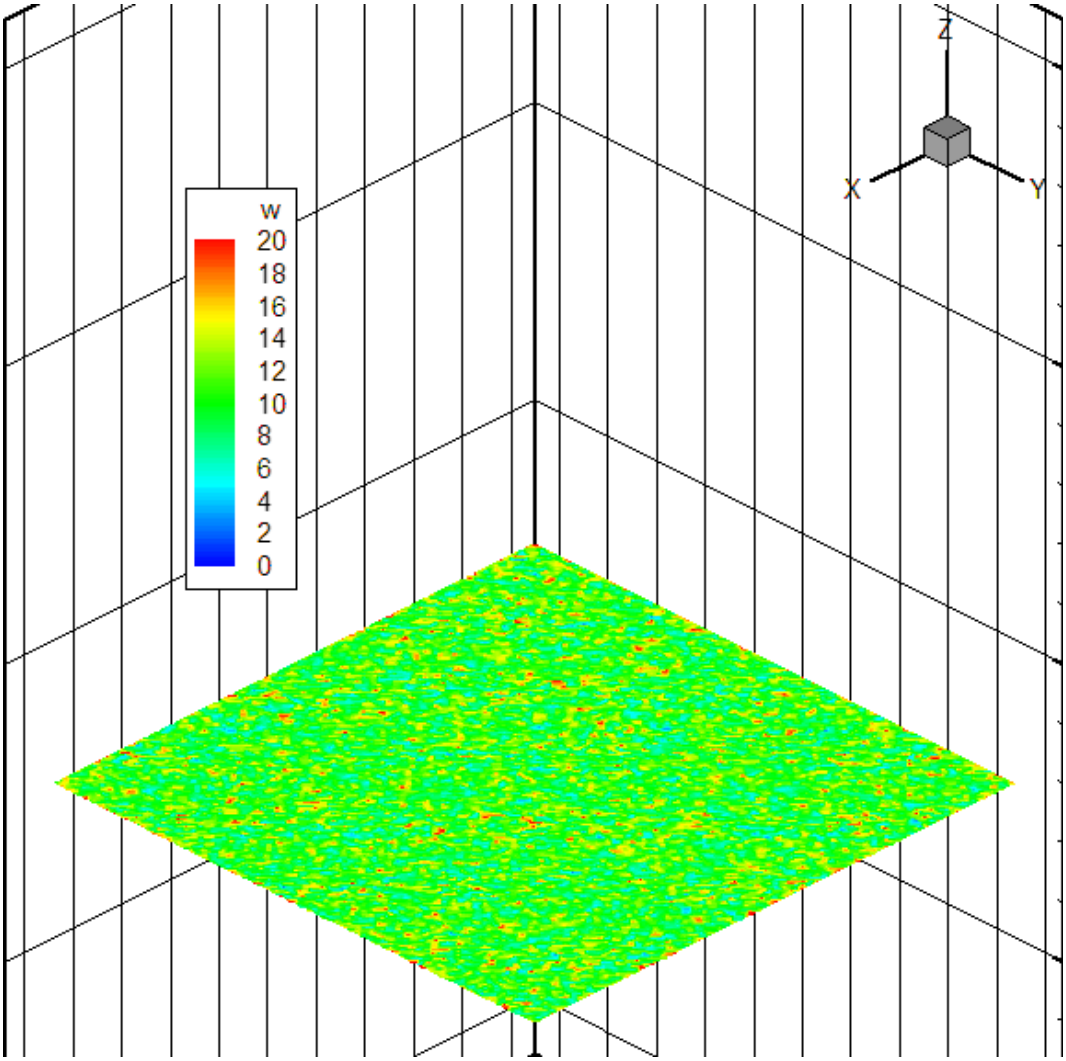

Figure A17. Vorticity magnitude in an x-y plane at a position away from the vortex ring, clean function off. Visible vorticity is due to the random perturbation added to the system. $\omega_{max} = 30.5\ s^{-1}$.

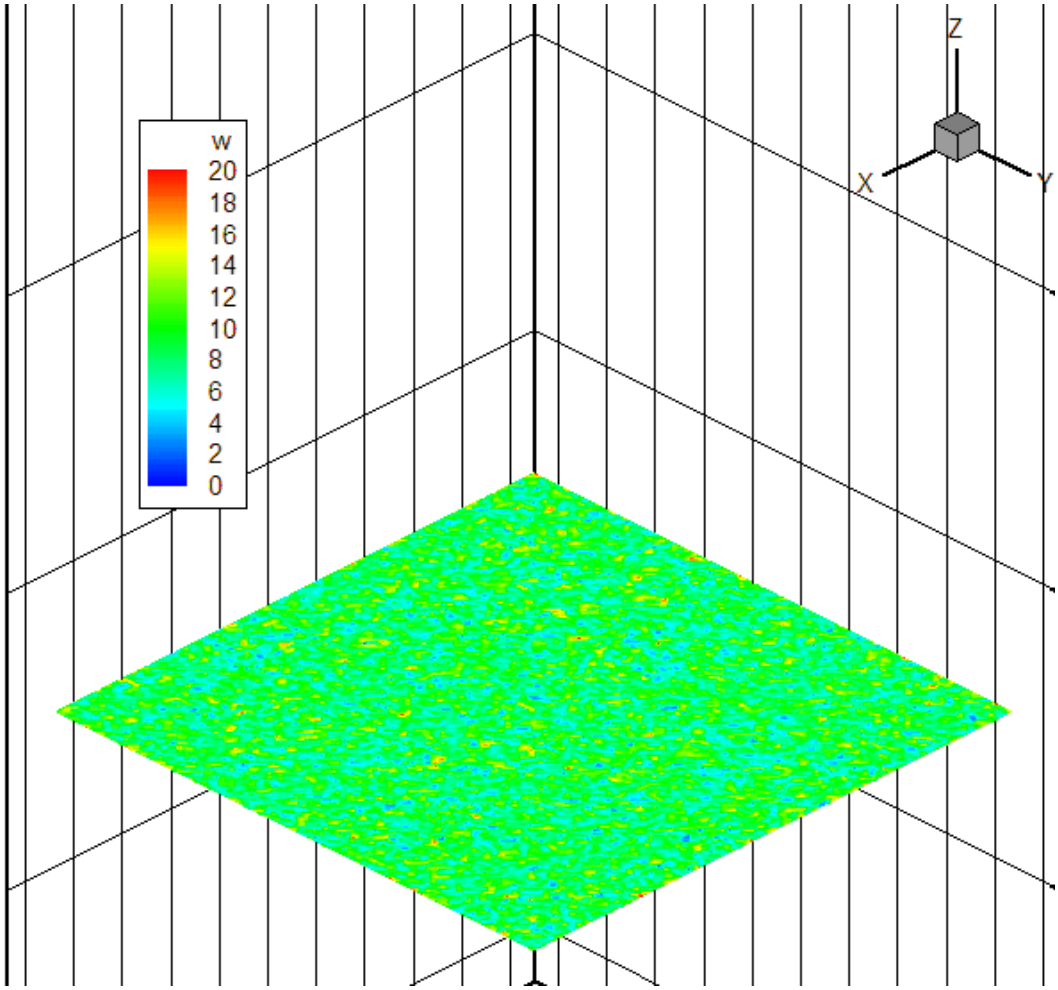

Figure A18. Vorticity magnitude in an x-y plane at a position away from the vortex ring, clean function on. Visible vorticity is due to the random perturbation added to the system. $\omega_{max} = 23.3\ s^{-1}$.

Appendix 9. Sample Code for Setting Initial Conditions

Below is a sample of the code used to set the initial vorticity in the simulation. The program takes x,y,z coordinates as inputs, and outputs the vorticity components at the given coordinates. The sample includes a Rayleigh unstable opposite-signed vortex ring and the 30 wave-number perturbation on the primary ring. The code was written in FORTRAN, originally by Jens Walther and then modified for the simulations used in this thesis. The code is shown here with permission from Jens Walther.

```
!------------------------------------------------------------------------
!  Subroutine   :                     UsrRou
!------------------------------------------------------------------------
!
!  Purpose      : User routine specifying the vorticity as function of
!                 the spatial co-ordinates (x,y,z).
!
!  Input        : (x,y,z)    : Cartesian co-ordinates
!
!  Input/output :
!
!  Output       : (v1,v2,v3) : vorticity components at (x,y,z)
!                 info       : should return zero on success.
!
!  Routines     :
!
!  Remarks      :
!
!  References   :
!
!  Revisions    :
!------------------------------------------------------------------------
!  $Log: UsrRou.stn,v $
!  Revision 1.1  1999/03/08 12:01:04  walther
!  Initial revision
!
!------------------------------------------------------------------------
!  Jens Honore Walther
!  Institute of Fluid Dynamics
!  ETH Zentrum
!  Sonneggstrasse 3
!  CH-8092 Zurich, Switzerland
!------------------------------------------------------------------------

SUBROUTINE UsrRou(x,y,z,v1,v2,v3,info)
!------------------------------------------------------------------------
!  Modules
!------------------------------------------------------------------------
USE m_cic
IMPLICIT NONE
!------------------------------------------------------------------------
!  Arguments
!------------------------------------------------------------------------
INTEGER               :: info
REAL(MK), INTENT(IN)  :: x,y,z
REAL(MK), INTENT(OUT) :: v1,v2,v3
!------------------------------------------------------------------------
!  Local variables
!------------------------------------------------------------------------
INTEGER               :: i,j,k,iteration,arraysize
REAL(MK)              :: gamma,r0,x0,y0,z0,alpha,alpha_inv2
REAL(MK)              :: factor,theta,xt,yt,zt,s2,arg,om_theta
REAL(MK)              :: pi
```

```
      REAL(MK)             :: magnitude,phase(30)
      INTEGER, DIMENSION(:), ALLOCATABLE :: seed
      LOGICAL               :: UsrRou_first=.TRUE.
      !-----------------------------------------------------------------------
      !  Save
      !-----------------------------------------------------------------------
      SAVE UsrRou_first

      !-----------------------------------------------------------------------
      !  Initialise
      !-----------------------------------------------------------------------
      info = 0

      !-----------------------------------------------------------------------
      !  Here: code the vorticity as function of the (x,y,z) co-ordinates
      !-----------------------------------------------------------------------
!     IF (UsrRou_first) THEN
!        UsrRou_first = .FALSE.
!        WRITE(*,'(A)')'User routine for ring (Orlandi parameters)'
!     ENDIF
      pi         = ACOS(-1.0)
      gamma      = 14
      r0         = 0.13
      z0         = 0.8
      x0         = 0.5
      y0         = 0.5
      alpha      = 0.42 * r0
      alpha_inv2 = 1./(alpha**2)
      factor     = Gamma*(alpha_inv2/pi)

      IF (x.EQ.x0.AND.y.EQ.y0) THEN
         theta = 0.0_MK
      ELSE
         theta = ATAN2(y - Y0,x - X0)
      ENDIF

      xt         = x0 + r0*COS(theta)
      zt         = z0
      yt         = y0 + r0*SIN(theta)

      !-----------------------------------------------------------------------
      !  adds waves in the x,y plane to the core
      !-----------------------------------------------------------------------

      magnitude  = 0.01*r0
      call random_seed(size=arraysize)
      allocate(seed(arraysize))
      seed = 3
      call random_seed(put=seed)
      call random_number(phase)
      do iteration = 1,30
          xt         = xt + magnitude*SIN(theta +
2*pi*phase(iteration))*COS(theta)
          yt         = yt + magnitude*SIN(theta +
2*pi*phase(iteration))*SIN(theta)
      end do

      s2         = (x - xt)**2 + (y - yt)**2 + (z - zt)**2

      arg = s2 * alpha_inv2
!     IF (arg.LT.10.0_MK) THEN
         om_theta = factor * EXP(-arg)
         v1       =  om_theta * SIN(theta)
         v2       = -om_theta * COS(theta)
         v3       =  0.0
!     ELSE
!        v1       = 0.
!        v2       = 0.
!        v3       = 0.
!     ENDIF
      !-----------------------------------------------------------------------
```

```
      !  add a second ring (coaxially), smaller, weaker and with the opposite sign
      !-------------------------------------------------------------------------
      gamma      = -4.2
      r0         = 0.1043
      z0         = 0.8257
      x0         = 0.5
      y0         = 0.5
      alpha      = 0.00546
      alpha_inv2 = 1./(alpha**2)
      factor     = Gamma*(alpha_inv2/pi)

      IF (x.EQ.x0.AND.y.EQ.y0) THEN
         theta = 0.0_MK
      ELSE
         theta = ATAN2(y - Y0,x - X0)
      ENDIF

      xt         = x0 + r0*COS(theta)
      zt         = z0
      yt         = y0 + r0*SIN(theta)
      s2         = (x - xt)**2 + (y - yt)**2 + (z - zt)**2

      arg = s2 * alpha_inv2
!     IF (arg.LT.10.0_MK) THEN
         om_theta = factor * EXP(-arg)
         v1       =  v1 + om_theta * SIN(theta)
         v2       =  v2 - om_theta * COS(theta)
         v3       =  0.0
!     ELSE
!        v1       = 0.
!        v2       = 0.
!        v3       = 0.
!     ENDIF
      !-------------------------------------------------------------------------
      !  Return
      !-------------------------------------------------------------------------
 9999 CONTINUE
      RETURN
      END SUBROUTINE UsrRou
```